National Library of Canada
Acquisitions and Bibliographic Services Branch
395 Wellington Street
Ottawa, Ontario
K1A 0N4

Bibliothèque nationale du Canada
Direction des acquisitions et des services bibliographiques
395, rue Wellington
Ottawa (Ontario)
K1A 0N4

Your file Votre référence

Our file Notre référence

NOTICE

The quality of this microform is heavily dependent upon the quality of the original thesis submitted for microfilming. Every effort has been made to ensure the highest quality of reproduction possible.

If pages are missing, contact the university which granted the degree.

Some pages may have indistinct print especially if the original pages were typed with a poor typewriter ribbon or if the university sent us an inferior photocopy.

Reproduction in full or in part of this microform is governed by the Canadian Copyright Act, R.S.C. 1970, c. C-30, and subsequent amendments.

AVIS

La qualité de cette microforme dépend grandement de la qualité de la thèse soumise au microfilmage. Nous avons tout fait pour assurer une qualité supérieure de reproduction.

S'il manque des pages, veuillez communiquer avec l'université qui a conféré le grade.

La qualité d'impression de certaines pages peut laisser à désirer, surtout si les pages originales ont été dactylographiées à l'aide d'un ruban usé ou si l'université nous a fait parvenir une photocopie de qualité inférieure.

La reproduction, même partielle, de cette microforme est soumise à la Loi canadienne sur le droit d'auteur, SRC 1970, c. C-30, et ses amendements subséquents.

Canada

UNIVERSITY OF ALBERTA

INTERFACIAL STRUCTURES AND ELECTRICAL PROPERTIES IN Pd-BASED METALLIZATIONS TO N-TYPE InP

By

PING JIAN

A thesis submitted to the Faculty of Graduate Studies and Research in partial fulfillment of the requirements for the degree of **MASTER OF SCIENCE**

IN

METALLURGICAL ENGINEERING

DEPARTMENT OF **MINING, METALLURGICAL AND PETROLEUM ENGINEERING**

EDMONTON, ALBERTA

FALL 1993

National Library
of Canada

Acquisitions and
Bibliographic Services Branch

395 Wellington Street
Ottawa, Ontario
K1A 0N4

Bibliothèque nationale
du Canada

Direction des acquisitions et
des services bibliographiques

395, rue Wellington
Ottawa (Ontario)
K1A 0N4

Your file Votre référence

Our file Notre référence

The author has granted an irrevocable non-exclusive licence allowing the National Library of Canada to reproduce, loan, distribute or sell copies of his/her thesis by any means and in any form or format, making this thesis available to interested persons.

L'auteur a accordé une licence irrévocable et non exclusive permettant à la Bibliothèque nationale du Canada de reproduire, prêter, distribuer ou vendre des copies de sa thèse de quelque manière et sous quelque forme que ce soit pour mettre des exemplaires de cette thèse à la disposition des personnes intéressées.

The author retains ownership of the copyright in his/her thesis. Neither the thesis nor substantial extracts from it may be printed or otherwise reproduced without his/her permission.

L'auteur conserve la propriété du droit d'auteur qui protège sa thèse. Ni la thèse ni des extraits substantiels de celle-ci ne doivent être imprimés ou autrement reproduits sans son autorisation.

ISBN 0-315-88132-1

Canada

UNIVERSITY OF ALBERTA

RELEASE FORM

NAME OF AUTHOR: **Ping Jian**

TITLE OF THESIS: **Interfacial Structures and Electrical Properties in Pd-Based Metallizations to n-Type InP**

DEGREE: **Master of Science**

YEAR THIS DEGREE GRANTED: **Fall 1993**

Permission is hereby granted to the University of Alberta Library to reproduce single copies of this thesis, and to lend or sell such copies for private, scholarly or scientific research purposes only.

The author reserves all other publication and other rights in association with the copyright in the thesis, and except as hereinbefore provided neither the thesis nor any substantial portion thereof may be printed or otherwise reproduced in any material form whatever without the author's prior written permission.

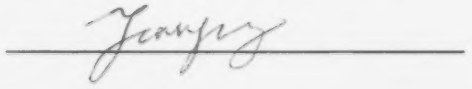

c/o. Mr. Jian Xin
Building 5-2-403, Tuanjiehu Beitoutiao
Beijing, P.R.China

Date: June 27/93

UNIVERSITY OF ALBERTA

FACULTY OF GRADUATE STUDIES AND RESEARCH

The undersigned certify that they have read, and recommend to the Faculty of Graduate Studies and Research for acceptance, a thesis entitled **INTERFACIAL STRUCTURES AND ELECTRICAL PROPERTIES IN Pd-BASED METALLIZATIONS TO N-TYPE InP** submitted by **PING JIAN** in partial fulfillment of the requirements for the degree of **MASTER OF SCIENCE** in **METALLURGICAL ENGINEERING.**

Dr. D. G. Ivey
Supervisor

Dr. M. L. Wayman

Dr. R. F. Egerton

Dr. A. C. Pierre

Mr. Robert Bruce

DATE: June 29/93

Abstract

InP and InP-based compound semiconductors are becoming increasingly important materials in the electronics industry, because of their unique combination of electrical and optical properties. The fabrication of reliable ohmic contacts to InP has been a major obstacle in the development of InP-based semiconductor devices. Pd-based metallizations make up one type of ohmic contact scheme to InP.

Three Pd-based metallizations have been systematically studied, i.e., Pd/InP, Au/Ge/Pd/InP and Pd/Ge/Pd/InP. The Pd/InP metallization is studied in an effort to better understand the role of Pd in Pd-based metallizations, while the other two metallizations are actual ohmic contact designs. Pd reacts with InP to form an amorphous and an epitaxial layer at low temperatures, which provides good metallization adhesion to InP substrates and improves the contact morphology. Au reacts strongly with In to form Au-In compounds, which creates more In site vacancies in the InP substrate and enhances doping in the InP surface. Ge is not only a dopant but also a reactant in the contacts. Changing the amount of Ge in the contact scheme can control the reaction products. Ohmic contacts to n-type InP have been fabricated in both the Au/Ge/Pd/InP and Pd/Ge/Pd/InP systems. The minimum specific resistances are $2.5\times10^{-6}\Omega cm^2$ in the Au/Ge/Pd/InP contacts and $1\times10^{-5}\Omega cm^2$ in the Pd/Ge/Pd/InP system. The annealing regime for ohmic contact formation is 300-375°C for the Au/Ge/Pd/InP system and 400-425°C for the Pd/Ge/Pd/InP system. The relationship between microstructural changes and electrical properties has been investigated. The onset of ohmic behavior in the contacts follows the decomposition of an epitaxial layer at the metallization/InP interface. The degradation of the contact resistance is due to the overreaction between metals and InP, which consumes more InP and destroys the heavily doped InP layer.

Acknowledgements

I am deeply grateful to Dr. D. G. Ivey for his supervision, guidance, and encouragement extended throughout the course of this study and during my entire tenure at the University of Alberta.

I am greatly appreciative to the Bell-Northern Research, Ltd.(BNR) for their financial support and for providing all materials and their excellent facilities for thin film deposition and electrical measurements for this study.

I especially thank Mr. R. Bruce for his continued and invaluable help throughout the research. Many thanks are also due to Dr. G. Knight who kindly provided MOCVD growths on InP substrates for this study.

I wish to thank Dr. R. F. Egerton, Dr. M. H. Chen, Mr. R. Bhatnagar and Mr. J. Malinski who provided access to TEMs. I also acknowledges Ms. Tina Barker, Mr. John Czuroski for their help in obtaining supplies.

Finally, I would like to thank my husband, Mr. Lin Zhang, for his selfless support and encouragement.

Table of Contents

Chapter 1
Introduction 1

Chapter 2
Properties and Applications of InP 4
2.1 Energy band structure 4
2.2 Applications of InP 5

Chapter 3
Metal-Semiconductor Contacts 10
3.1 Formation of Schottky barriers 10
3.2 Formation of ohmic contacts 13
3.3 Principles for forming ohmic contacts 13
3.4 Measurement of the specific contact resistance r_c 15
3.4.1 Cox-Strack method 16
3.4.2 Four point method 17
3.4.3 Shockley technique 17
3.4.4 Transmission-line method 18

Chapter 4
Formation, Structure and Properties of Metal/Semiconductor Contacts 27
4.1 Gold-based metallizations 27
4.1.1 Au/InP contacts 28
4.1.2 Gold-based/InP contacts 29
4.2 Near noble transition metal-based metallizations 33
4.2.1 Near noble transition metal element contacts 33
4.2.2 Near noble transition metal-based/GaAs contacts 41
4.2.3 Near noble transition metal-based/InP contacts 47

Chapter 5
Experimental Methods 72
5.1 Experimental materials 72
5.2 Metal thin film deposition 72

5.3 Annealing procedure 73
5.4 Microstructural characterization 73
5.4.1 X-ray diffraction experiments 73
5.4.2 Transmission electron microscopy (TEM) 73
5.4.2.1 TEM specimen preparation 74
5.4.2.2 Phase identification 75
5.4.3 Specific contact resistance measurements 76

Chapter 6
Reactions between Pd thin films and InP 83
6.1 Reactions between Pd thin films and InP 83
6.2 Discussion 85
6.2.1 Amorphous formation 85
6.2.2 Ternary phase formation 87
6.2.3 Pd-In-P phase diagram 89

Chapter 7
Reactions between multilayer metallizations and InP 101
7.1 Au/Ge/Pd/InP contacts 101
7.1.1 Resistance measurements 101
7.1.2 Microstructural evolution 101
7.2 Pd/Ge/Pd/InP contacts 104
7.3 Discussion 109
7.3.1 Reactions in the Au/Ge/Pd/InP contact system 109
7.3.2 Reactions in the Pd/Ge/Pd/InP contact system 112
7.3.3 Comparison of Au/Ge/Pd/InP and Pd/Ge/Pd/InP contacts 115
7.3.4 Mechanism of ohmic contact formation 118

Chapter 8
Conclusions and Recommendation 148
8.1 Conclusions 148
8.2 Recommendation 149

References 150

List of Tables

Table 2-1	Properties of InP, GaAs and Si	9
Table 4-1	Au-In intermetallic compounds	63
Table 4-2	Au-based contact to InP	64
Table 4-3	Date summary: Ni, Pd, Co, Rh, Pt and Ir on GaAs	65
Table 4-4	Summary of electrical measurements on five types of diodes	66
Table 4-5	Ni-In-P intermetallic compounds	67
Table 4-6	Pd-In-P intermetallic compounds	68
Table 4-7	Resistance of AuGeM (M=Ni, Pd or Pt)/GaAs contacts	69
Table 4-8	Specific contact resistance of Pd-based/GaAs contacts	70
Table 4-9	Resistance of near noble transition metal-based/InP contacts	71
Table 5-1	Annealing regime	81
Table 5-2	Geometry factors in planar contacts	82
Table 6-1	Summary of crystallographic date for ternary and binary phases in Pd/InP system	100
Table 7-1	Specific contact resistances in the Pd/Ge/Pd/InP contacts	147

List of Figures

Fig. 2-1a	E-K diagram for a direct gap semiconductor	7
Fig. 2-1b	E-K diagram for an indirect gap semiconductor	7
Fig. 2-2	Calculated energy band structure of InP	8
Fig. 3-1	Energy-band diagrams of a metal and a n-type semiconductor	19
Fig. 3-2	Electrical properties and band diagram of an ideal metal-n-type semiconductor interface	19
Fig. 3-3	I-V characteristics of a Schottky barrier	20
Fig. 3-4a	Energy-band diagrams of a metal and a p-type semiconductor	21
Fig. 3-4b	Band diagram of an ideal p-type metal-semiconductor interface	21
Fig. 3-5	Pinning of the Fermi level by surface states	22
Fig. 3-6	Band diagrams describing the Schottky theory of the metal-semiconductor interface	22
Fig. 3-7	Field and thermionic-field emission under forward bias	23
Fig. 3-8	I-V characteristics of an ohmic contact	23
Fig. 3-9	Contact resistance measurement by the Cox-Strack method	24
Fig. 3-10	Contact resistance measurement by the four point method	24
Fig. 3-11	Contact resistance measurement by the Shockley technique	25
Fig. 3-12a	Contact resistance measurement by the transmission-line model (TLM) technique	26
Fig. 3-12b	A method of determining R_e	26
Fig. 4-1a	Schematic representation of the reactions of Au films on InP substrates	51
Fig. 4-1b	Au-In-P phase diagram	51
Fig. 4-2	Schematic representation of the reactions of Ni films on GaAs substrates	52
Fig. 4-3	Ni-Ga-As phase diagram at 600°C	52
Fig. 4-4	Schematic representation of the reactions of Pd films on GaAs substrates	53
Fig. 4-5	Pd-Ga-As phase diagram at 600°C	53
Fig. 4-6	Schematic representation of the reactions of Co films on GaAs substrates	54
Fig. 4-7	Co-Ga-As phase diagram at 600°C	54
Fig. 4-8	Schematic representation of the reactions of Rh films on GaAs substrates	55
Fig. 4-9	Rh-Ga-As phase diagram at 800°C	55
Fig. 4-10	Schematic representation of the reactions of Pt films on GaAs substrates	56
Fig. 4-11	Pt-Ga-As phase diagram at 600°C	56
Fig.4-12	Schematic representation of the reactions of films on GaAs substrates	57
Fig. 4-13	Ir-Ga-As phase diagram at 600°C	57

Fig. 4-14	Ni-In-P phase diagram	59
Fig. 4-15	Schematic representation of the reactions of Ni films on InP substrates	59
Fig. 4-16	Pd-In-P phase diagram at 600°C	60
Fig. 4-17	Schematic representation of the reactions of Pd films on InP substrates	60
Fig. 4-18	Schematic representation of the reactions of Ge/Pd/InP contacts	61
Fig. 4-19	Schematic representation of the reactions of Si/Pd/InP contacts	61
Fig. 4-20a	Plot of contact resistance vs annealing temperature of Pd-based contacts	62
Fig. 4-20b	Thermal stability of Pd-based contacts at 400°C	62
Fig. 5-1a	Schematic showing TEM sample preparation procedure	80
Fig. 6-1	X-ray spectrum of the amorphous Pd-In-P	90
Fig. 6-2	Images of Pd/InP specimens annealed at 225°C for <8min.	91
Fig. 6-3	Images of Pd/InP sample annealed for 15 min. at 225°C.	92
Fig. 6-4	Computed SAD patterns of Pd_2InP and Pd_5InP	93
Fig. 6-5	Image, SAD patterns of Pd_2InP(II) and x-ray spectrum of Pd/InP sample annealed at 350°C for 5 min	94
ig. 6-6	Images of Pd/InP specimens annealed at 500°C	95
Fig. 6-7	Images of Pd/InP specimen annealed at 500°C for 5 min	96
Fig. 6-8	Schematic SAD pattern of Pd5InP superimposed on [001] InP.	97
Fig. 6-9	Schematic representation of the reactions of Pd films on InP substrates	98
Fig. 6-10	Isothermal section of the Pd-In-P phase diagram	99
Fig. 7-1	Plot of contact resistance vs annealing time in Au/Ge/Pd/InP contacts	123
Fig. 7-2	Image and EDX spectra of as deposited AuGePd/InP sample	124
Fig. 7-3	Images of AuGePd/InP sample annealed at 250°C	125
Fig. 7-4	Images of AuGePd/InP specimens annealed at 325 to 350°C	126
Fig. 7-5	Image and CBED pattern of a plan view specimen annealed at 350°C	127
Fig. 7-6	Image and EDX spectrum of a plan view specimen annealed at 325°C	128
Fig. 7-7	Images of AuGePd/InP specimens annealed at 400 to 450°C	129
Fig. 7-8	Image and CBED pattern of a plan view specimen annealed at 400°C	130
Fig. 7-10	Images of as deposited PdGePd/InP contact	132
Fig. 7-11	Image of a cross section PdGePd/InP specimen annealed at 250°C	134
Fig. 7-12	Images and SAD patterns of plan view PdGePd/InP samples annealed at 250°C	135
Fig. 7-13	Images and EDX spectrum of PdGePd/InP specimens annealed at 350°C	136
Fig. 7-14	Images and SAD patterns of a PdGePd/InP specimen annealed at 400°C	138
Fig. 7-15	Images of cross section PdGePd/InP specimens annealed at 425°C for <180min.	140

Fig. 7-16 Images, EDX spectrum, SAD and CBED patterns of PdGePd/InP specimen annealed at 425°C for 5 hours 141
Fig. 7-17 Schematic representation of the Pd/Ge/Pd/InP contact system 143
Fig. 7-18. Images of Pd/(20nm)Ge/Pd/InP specimens annealed at 250-350°C 144
Fig. 7-19 Images of cross section Pd/(20nm)Ge/Pd/InP specimens annealed at 425°C 145
Fig. 7-20 Image and SAD pattern of Gd_2Ge in sample annealed at 425°C for 180s 146

Chapter 1 Introduction

InP, a direct band gap compound semiconductor, is becoming an important semiconductor material because of its unique combination of electrical and optical properties, e.g., high electron mobility, high saturation velocity and superior radiation tolerance. The primary application of InP and related alloys in the semiconductor industry is in the fabrication of optoelectronic devices or lightwave devices.

During device operation, electrical communication links between the active regions of these semiconductor devices and the external circuit are provided by metal/semiconductor contacts. Generally, when a metal and a semiconductor are brought together, there exists a energy barrier for electron transportation from the semiconductor side to the metal side at the metal/semiconductor interface, due to the difference in work function between the metal and semiconductor. According to their current-voltage characteristic, the contact can be divided into two categories. One type is called a Schottky barrier or rectifying contact, which has a high contact resistance with respect to electronic devices. The other is an ohmic contact, which has a linear current-voltage characteristic due to a small contact resistance compared with the device resistance. Ohmic contacts on InP-based materials are essential for electronic devices such as field effect transistors (FET), junction field effect transistors (JFET), high electron mobility transistors (HEMT) and heterojunction bipolar transistors (HBT), as well as for photonic devices, such as long-wavelength laser diodes, light-emitting diodes (LED) and photoelectronic and solar cells. With the remarkable progress in the current microelectronic industry, semiconductor devices are to be further scaled down in size, and to be operated at higher current density and elevated temperature. Therefore, the requirements for the ohmic contacts to these devices are low contact resistance and high thermal stability, which are affected directly by the microstructures of the contacts. It is essential to understand the relationship between the microstructure and the electrical properties of the metal/semiconductor contacts in order to fabricate high quality and reliable ohmic contacts. Transmission electron microscopy (TEM) combined with energy dispersive X-ray spectroscopy is one of the best techniques to monitor and analyze the microstructural changes that occur during annealing. It allows direct observation of interfaces and provides information on both crystal structures and chemical composition with high spacial resolution in three dimensions. However, very little work has been done by TEM, in this area, although hundreds of papers reporting experimental results from metal/compound semiconductor contacts have been published, due to the difficulty in TEM sample preparation.

In practice, most ohmic contacts are basically Schottky barriers, but the barrier width is narrowed, by high dopant concentration, so that a majority of the electrons can tunnel through the barrier. Therefore, the most conventional way of forming an ohmic contact to InP-bsaed devices is by introducing an external dopant diffusion source, from which the dopant will be driven into the semiconductor by annealing. Although there is a wide variety in contact structures, the metallizations usually consist of a dopant element, such as Si and Ge for n-type III-V compound semiconductors or Zn and Be for p-type III-V compound semiconductors, and an electronegative metal, such as Au or Pd, acting as a dopant medium to improve the metallization wettability and contact electrical properties. Based on the type of electronegative metal in the metallizations, contacts are classified into three systems: Au-based contacts, near noble transition metal-based contacts and refractory metal-based contacts. The refractory metal-based contacts are used in the devices operated in high temperature environments (>600°C).

Au-based metallizations are the most widely used ohmic contacts to III-V compound semiconductors today because they present several advantages. But all Au-based contacts suffer from the same general disadvantages:

1. Uneven depth of interaction (spikes of Au alloy penetrate into the substrates) and spatial composition distribution, leading to nonuniform current density through the contact.
2. Lack of long-term metallurgical stability.
3. Relatively high specific contact resistance.

These deficiencies make Au-based contacts incompatible with the fabrication of submicron planar devices or higher current density application devices. As a result, the near noble transition metal-based contacts have been suggested as alternative contacts. Due to more stable thermodynamic properties and a less reactive nature, the near noble transition metal-based contacts provide a microstructure which is less reactive and degrades less during heat treatment at higher temperature. Near noble transition metal-based contacts to GaAs have been studied extensively. Some of these contacts have become industry standards for GaAs devices, while very little work has been done on InP, because of the unstable nature of InP. InP tends to decompose through heat treatment at temperatures as low as 350°C and loses the group V volatile element, P. This is reflected in a degraded contact interface morphology, poor edge geometry definition and uneven penetration of both the metal and the semiconductor elements. Therefore, it is considered that manufacturing an ohmic

contact to InP, with high quality to support both short- and long-term device operation, is much more challenging and more difficult than to GaAs.

Since palladium has a number advantages for making contacts, such as ease of deposition on III-V compound semiconductors, reactivity with both GaAs and InP at low temperatures, penetrability of thin native oxides on the semiconductor surface and resistance to oxidation, Pd-based metallizations are considered to be one of the most attractive ohmic contacts to both n-type and p-type III-V compound semiconductors. Consequently, Pd-based metallizations on n-type InP are investigated systematically in this research. Electron microscopy techniques are used as the main tool to monitor microstructural changes in the Pd/InP, Au/Ge/Pd/InP and Pd/Ge/Pd/InP contacts during annealing processes. Contact resistances are measured to identify the effect of microstructure on the contact electrical properties. The main aims of this research are:

1. To study the interactions between Pd thin films and InP over a fairly wide temperature range in order to understand role of Pd in the formation of Pd-based ohmic contacts on InP.
2. To investigate the relationship between the microstructure and electrical properties of two practical Pd-based contact systems, i.e., Au/Ge/Pd/InP and Pd/Ge/Pd/InP contacts.

This thesis is organized in eight chapters. A comprehensive literature review is provided in Chapters 2 to 4, which consist of a brief summary of the properties of both InP and the metal/semiconductor contacts, and the ohmic contact formation principles. A comprehensive survey of published experimental results on metal/semiconductor contact structures and electrical properties, with emphasis on the metal/InP contact systems, is presented in Chapter 4. Chapter 5 describes the experimental procedures used for fabricating the Pd/InP, Au/Ge/Pd/InP and Pd/Ge/Pd/InP contact systems, and the techniques used for analyzing the structures and measuring the electrical properties. The characterization and discussion about the relationship between the microstructures and electrical properties are presented in Chapters 6 and 7.

Chapter 2 Properties and Applications of InP

Semiconductors are generally classified by their electrical resistivity at room temperature, with values in the range of 10^{-2} to 10^{9} ohm-cm [1]. Resistivities are strongly dependent on temperature. There are two types of semiconductors, i.e., elemental and compound semiconductors. Elemental semiconductor consist of Si and Ge, which belong to group IVA of the elemental Periodic Table. They are sometimes called diamond-type semiconductors, because they have the crystal structure of diamond. Compound semiconductors are formed from various combinations of elements. They have the chemical formula AB. If A is divalent and B is hexavalent, the compound is called a II-VI compound semiconductor. If A is a trivalent element and B is a pentavalent element, the compound is called a III-V compound semiconductor. Common elements used in III-V compound semiconductors include Al, Ga, In (group IIIA) and P, As, Sb (group VA). The atoms in III-V compound semiconductors are tetrahedrally bonded in a zinc-blende structure.

2.1. Energy band structure

The energy band structure of solid materials consists of a valence band and a conduction band. For most semiconductors, the valence band structures are the same, consisting of a heavy-hole band (hh), a light-hole band (lh), because of their large and small effective masses respectively, and a split-off hole band (soh) as shown in Fig. 2-1 [2]. The maximum in the valence band is located at **K**=0 (**K** represents momentum space), i.e., the center of the Brillouin Zone. But the conduction band structures for various semiconductors are different. The conduction band structure is comprised of several minima, including a single minimum at **K**=0 and additional minima along the [100] and [111] axes. The band gap is the difference in energy between the lowest point of the conduction band and the highest point of the valence band. If the conduction band minimum at **K**=0 is lowest in energy as shown in Fig. 2-1a, this band structure is called a direct-band gap structure, otherwise, it is an indirect-band gap structure, as shown in Fig. 2-1b.

The mobility and effective mass of electrons in a semiconductor strongly depend on the band gap structure of the semiconductor. In a direct band gap semiconductor, an

electron in the conduction band can fall directly to an empty state in the valence band, giving off the energy difference E_g as a photon of light. On the other hand, an electron in the conduction band minimum of an indirect semiconductor can not fall directly to the valence band maximum but must go through a state within the band gap. In an indirect transition, which involves a change in **K**, the energy is given up largely as heat to the lattice rather than as an emitted photon. The mobility of electrons (μ) is higher and the effective mass of electrons (m^*) is lower in direct band gap semiconductors than those in indirect band gap semiconductors. The difference between direct and indirect band structures is very important in deciding which semiconductor can be used in devices requiring light output.

The calculated energy band structure of InP is shown in Fig. 2-2 [3]. InP has a direct band gap structure. Both the valence maximum and the lowest conduction band minimum occur at the center of the Brillouin Zone (Γ point). The conduction band minimum is doubly degenerate and is separated by an energy E_g from the valence band maximum. Away from the zone center, the highest valence bands separate into two sets of bands, referred to as the heavy-hole and light hole bands. The next set of valence bands, referred to as the spin-split-off bands, also have their maximum at Γ, where they are doubly degenerate, separated by an energy Δ from the maxima of hh and lh bands. Higher conduction band minima occur in the [100] and [111] directions, as can been seen in Fig. 2-2. The minima in the [111] and [100] direction are, respectively, 0.4eV and 0.7eV above the Γ minimum.

2.2. Applications of InP

InP is becoming a semiconductor material of great importance because of its unique combination of electrical and optical properties. The properties of InP, GaAs and Si are listed in Table 2-1 [2, 4-6]. For high-speed electrons, a semiconductor with high electron mobility and high saturation velocity is desirable. High thermal conductivity and high breakdown fields are also desirable properties. All of these requirements are well met in InP [7, 8]. Its many alloy forms, such as InGaAs or InGaAsP, provide a variety of energy gaps and carrier mobilities. The primary use of InP and its alloys with Ga and As in the semiconductor industry is in the fabrication of optoelectronic devices or lightwave devices for optical fiber communication, such as lasers, photodetectors, solar cells, photodiodes and optoelectronic integrated circuits. In addition, much attention has been given to InP

due to its tolerance to radiation. Compared with Si and GaAs, InP is far superior in a radiation environment.

At present, InP is still not as popular as Si or GaAs in industrial applications due to its fragility, thermal stability and sensitivity to ion-induced damage compared with Si and GaAs [9]. The binary nature of the InP lattice makes ion implantation damage removal and dopant activation steps more complex than for Si. Amorphization of the In-based semiconductor obstructs attainment of the best electrical activation. Incongruent evaporation of P from the sample surface upon high temperature annealing is also a severe problem for InP. In addition, because InP and its alloys are more expensive than Si and GaAs, the cost of devices is several hundred times as high.

Fig. 2-1a has been removed due to copyright restrictions.

Fig. 2-1a **E-K** diagram for a direct gap semiconductor showing three hole masses: heavy holes, light holes and split-off holes [2].

Fig. 2-1b has been removed due to copyright restrictions.

Fig. 2-1b **E-K** diagram for an indirect gap semiconductor Si, showing that the minimum in the conduction band occurs at **K** values away from **K**=0 [2].

Fig. 2-2 has been removed due to copyright restrictions.

Fig. 2-2 Calculated energy band structure of InP in two principal directions in the Brillouin Zone [3].

Table 2-1 Properties of InP, GaAs and Si [2, 4-6]

Property (300K)		InP	GaAs	Si
Energy gap (E_g) eV		1.34	1.42	1.12
Effective mass (m*)	electrons	0.073	0.007	m_t=0.97 m_l=0.19
	holes (hh)	0.4	0.45	0.49
	holes (hl)	0.08	0.08	0.16
Intrinsic mobility	electrons	4600	8500	1500
(cm2/V-s)	holes	150	400	450
Resistivity ρ (Ω-cm)		2×10^{7}	4×10^{8}	2.5×10^{5}
Electron affinity χ (v)		4.38	4.07	4.05
Crystal structure		Zinc blende	Zinc blende	Diamond
Lattice constant (nm)		0.587	0.565	0.543
Density (g/cm^3)		4.79	5.32	2.33
Thermal expansion coefficient		4.56×10^{-6}	5.9×10^{-6}	2.6×10^{-6}
Thermal conductivity (W/cm-°C)		0.68	0.46	145
Melting point (°C)		1070	1238	1420

Chapter 3 Metal-Semiconductor Contacts

Based on their current-voltage characteristics, metal-semiconductor contacts can be divided into two classifications. Contacts with rectifying characteristics are called Schottky barriers or rectifying contacts, and contacts with linear characteristics are called ohmic contacts or nonrectifying contacts.

3.1. Formation of Schottky barriers

Fig. 3-1 [10] shows an energy-band diagram of a metal and an n-type semiconductor separated by a large distance. In the figure, ϕ_m indicates the work function of the metal, i.e., the energy needed to remove an electron from the Fermi level of the metal (E_F^m) to the vacuum level. The work function of the semiconductor is ϕ_s and

$$\phi_s = \chi_s + \xi \tag{3-1}$$

where the electron affinity χ_s is the difference in energy between an electron at the vacuum level and an electron at the bottom of the conduction band; ξ is the difference in energy between the Fermi level in the semiconductor (E_F^s) and the bottom of the conduction band.

In the case where the semiconductor is n-type and $\phi_s < \phi_m$ (Fig.3-1), if the metal and the semiconductor are brought together (the vacuum level is assumed to be the same in both materials), electrons flow from the semiconductor to the metal, accumulating at the surface of the metal and depleting the number of electrons in the surface region of the semiconductor. The resulting dipole electric field (due to the positive ions) opposes further electron flow, and in equilibrium,

$$E_F^m = E_F^s \tag{3-2}$$

In the Schottky model, the semiconductor is assumed to be homogeneous right up to the boundary with metal, so that the uncompensated donors give rise to a uniform space charge of depth w, called the depletion depth, or depletion region (Fig. 3-2a [10,11]). The induced

electric field strength ε therefore increases linearly with distance from the edge of the depletion region (Fig. 3-2b), and the electrostatic potential ψ increases quadratically (Fig. 3-2c). The resulting parabolic barrier is known as a Schottky barrier, as shown in Fig. 3-2d. The depletion layer width w is an inverse measure of the square root of the doping concentration [4]. The energy barrier ϕ_{Bn} is the energy difference between the Fermi level in the metal and the bottom of the conduction band in the semiconductor at the interface.

$$\phi_{Bn} = \phi_m - \chi_s \tag{3-3}$$

where ϕ_{Bn} is the Schottky barrier height of an n-type semiconductor, i.e., the energy necessary for electrons in the metal to penetrate the semiconductor, and it is the single most important parameter describing a Schottky barrier. The barrier for electrons in the semiconductor relative to the metal is V_d, the diffusion potential or the band bending in the semiconductor at equilibrium.

$$V_d = \phi_m - \phi_s = \phi_{Bn} - \xi \tag{3-4}$$

The current-voltage characteristics of a metal-semiconductor contact are governed by the transport of the charge carriers (i.e., electrons or holes) across the metal-semiconductor interface and its associated space-charge region. For a Schottky barrier, the current transport mechanism is thermionic emission. The majority carriers, with kinetic energies in excess of V_d, are emitted from the semiconductor over the top of the barrier into the metal. If a negative voltage V is applied to the semiconductor with respect to the metal, the semiconductor-to-metal barrier is reduced to V_d-V while ϕ_{Bn} remains unchanged. The reduction of the barrier on the semiconductor side makes it easier for electrons in the semiconductor to move to the metal. This is the forward-bias condition, and a large current can flow. On the other hand, if a positive voltage is applied to the semiconductor, the potential barrier is raised to prevent current conduction and reverse bias is achieved. The current-voltage relationship for an n-type semiconductor is an exponentially increasing current under forward bias and almost constant current under reverse bias. This rectifying characteristic is shown in Fig. 3-3 [2].

The energy band diagram of a metal and a p-type semiconductor pair, with $\phi_m < \phi_s$, before contact is shown in Fig. 3-4a. When the metal and semiconductor are joined, the positive carriers from the semiconductor cross over to the metal until the Fermi level of the metal-semiconductor system is aligned. This results in the band diagram depicted in Fig. 3-

4b. Similar to the metal-n-type semiconductor case described before, there are a Schottky barrier height ϕ_{Bp} for current (or positive carriers) from metal to semiconductor and a barrier V_d for current from the semiconductor to metal. When a forward bias V is applied to the contact (p-type semiconductor positive with respect to metal), which raises the electrostatic potential on the semiconductor side relative to the metal side, the barrier V_d is lowered to a smaller value (V_d-V). Current can more easily flow from semiconductor to metal. For a reverse bias (-V), the opposite occurs, the electrostatic potential of the semiconductor side is depressed relative to the metal side, and the potential barrier becomes larger (V_d+V). Therefore, it is difficult for positive carriers to pass the barrier from semiconductor to metal, i.e., there is no current flow in the contact. The contact shows a rectifying characteristic. For a given semiconductor and for any metal, the sum of the barrier height on n-type and p-type substrates is equal to the energy band gap [12] or :

$$\phi_{Bn} + \phi_{Bp} = E_g \qquad (3\text{-}5)$$

In practical metal-semiconductor contacts, the disruption of the crystal lattice at the interface produces a large number of energy states called interface or surface states, located within the forbidden gap. The interface states are usually continuously distributed in energy and are characterized by a neutral level E_o. The states below E_o are positively charged when empty; the states above E_o are negatively charged when occupied. If E_o is aligned with the Fermi level, the net charge of the surface is zero. Whenever $E_o > E_F$, the net charge of the interface states is positive, or donorlike, so that fewer ionized donors are needed in the depletion layer to reach equilibrium. As a result, the diffusion potential V_b is effectively reduced, and according to Eq. (3-4), the barrier height ϕ_{Bn} is also reduced (Fig. 3-5a [4]). Similarly, if $E_o < E_F$, there is a negative charge in the interface states and ϕ_{Bn} is increased to bring E_F closer to E_o again. Thus, the change in the interface states has a negative feedback effect which tends to keep E_F closer to E_o (Fig. 3-5b). If the interface state density is large, the Fermi level is effectively pinned down at E_o and ϕ_{Bn} becomes independent of the work function of the metal and semiconductor. In most practical Schottky barriers, interface states play a dominant role in determining the value of ϕ_{Bn}, and the barrier height is essentially independent of both the work function difference and doping level in the semiconductor.

3.2 Formation of ohmic contacts

If a metal and an n-type semiconductor pair with $\phi_m < \phi_s$, the exchange of carriers leading to a constant Fermi level results in the band diagram depicted in Fig. 3-6b [10]. The potential barrier at the junction is almost nonexistent, so that carriers can freely pass in either direction. As a result, this metal-semiconductor contact is ohmic. Also, it is shown in Fig. 3-6c that a metal-to-p-type semiconductor with $\phi_m > \phi_s$ is also an ohmic contact . In addition to the no potential barrier case, there are other possibilities for forming ohmic contacts in metal semiconductor junctions. Since the width of the depletion layer decreases with an increase in doping level, quantum-mechanical tunneling of electrons through the barrier can occur. At very high doping levels, i.e., with an impurity density (N_d) of $10^{18}cm^{-3}$ or more, the barrier can be thin enough to permit electrons, with energies close to the Fermi energy in the semiconductor, to tunnel through the barrier at low temperature. This is known as "field emission". At moderately high doping levels ($10^{17}cm^{-3} < N_d < 10^{18}cm^{-3}$ [13]), the barrier is somewhat wider. However, if the temperature is increased, electrons can still gain enough thermal energy (E_m) and tunnel near the top of the barrier producing an appreciable current. This process is known as thermionic-field emission. Fig. 3-7 [11] shows both field and thermionic-field emission. Field emission is independent of temperature, while thermionic-field emission is temperature dependent. Both types of quantum-mechanical tunneling can lead to ohmic behavior in the contacts. The current-voltage relationship of ohmic contacts is approximately linear as shown in Fig. 3-8 [4]. When the ohmic contacts are applied to a uniform semiconductor sample or a device, the measured current-voltage relationship is determined by the resistivity of the semiconductor sample or by the behavior of the device to which the contact is formed, rather than by the characteristics of the contact. It is not essential that the current-voltage characteristic of the contact itself be linear, provided its resistance is very small compared with the resistance of the specimen or device. In addition, the contact should not inject minority carriers and should be stable both electrically and mechanically.

3.3 Principles for forming ohmic contacts

Modern high-speed electronic and photonic devices are operated under a high current density, with dimensions in the range of 2 to 150μm in width. They require a very low specific contact resistance for the contact which links the active region of the semiconductor device to the external circuit, in order that only a negligible voltage drop

occurs after current passes it. Low resistance ohmic contacts can satisfy this requirement. From the preceeding discussions, the general principles for forming ohmic contacts can be summarized as:

1) A metal with a work function less than the work function of an n-type semiconductor or greater than the work function of a p-type semiconductor is one possibility.
2) A semiconductor with an extremely narrow band gap, such as InAs (0.35eV) which can be epitaxially grown and lattice matched to an InP substrate is another possibility. This semiconductor has high electron and hole mobilities (33,000 and 460 $cm^2/V.s$ respectively, at 300K) and has surface states pinned in the bandgap; therefore, it forms an ohmic contact with almost every metal that is deposited onto it [9].
3) A third possibility is to provide a very heavily doped thin layer on the semiconductor surface, which is to be immediately adjacent to the metal. The depletion region is then so thin that field emission may take place and the contact has a very low resistance at zero bias. The most conventional way of making doped surfaces is to incorporate a high concentration of dopants into the initially grown epitaxial semiconductor layer, by introducing an external dopant diffusion source. The dopants will be driven into the semiconductor by means of a heating process or by ion implanting the semiconductor surface. The latter approach is rarely applied to InP and related materials because of the surface damage and loss of stoichiometry associated with bombarding the InP surface.

Ohmic contacts to InP-based materials are essential for electronic devices, such as field effect transistors (FET) [14,15], junction field effect transistors (JFET) [15,16], high electron mobility transistors (HEMT) and heterojunction bipolar transistors (HBT) [18,19], as well as for photonic devices such as long-wavelength laser diodes, light-emitting diodes (LED) [20-22] and photoelectronic and solar cells [23]. When designing an ohmic contact to such high-speed InP-based devices, operated under a high current density and elevated-temperature conditions, a few constraints and requirements have to be met in order to provide a suitable contact technology to support both short and long term device operation. The main issues that have to be considered when selecting the metallization scheme and the process conditions are: a) optimizing the contact design to yield an ohmic contact with the lowest possible resistance; b) providing stable morphology over a wide temperature range, i.e., only limited intermetallic reactions and an abrupt metal-semiconductor interface in the contacts throughout contact processing; c) ensuring contact stability throughout the device electrical and thermal operating conditions; d) excessive stresses in the metal films, the

underlying dielectric patterning layer, and the underlying semiconductor should be avoided; e) compatibility with the metal system used for the interconnection technology, and f) fabrication with a robust process that fits as an integrated step into the overall device manufacturing scheme.

3.4. Measurement of the specific contact resistance r_c

The most often used parameter to characterize an ohmic contact is the specific contact resistance r_c defined by

$$r_c = (\frac{\partial v}{\partial J})_{v=0} \, (\Omega\text{-cm}^2) \tag{3-6}$$

where V is the voltage and J is the density of the current. The specific contact resistance, r_c, is considered as an important figure in evaluating the quality of an ohmic contact. It is in fact one of the basic parameters by which different metal systems or metal preparation procedures are typically examined, compared and selected. Moreover, r_c can give information on the surface doping level in the semiconductor, hence providing useful insights into the contact formation mechanisms, or can be monitored to test contact stability and reliability. For a homogeneous contact of area A having uniform current density, the contact resistance R_c is simply

$$R_c = \frac{r_c}{A} \tag{3-7}$$

the measured resistance R will be approximately equal to R_c for most sample geometries when $r_c \geq 10^{-2} \Omega\text{-cm}^2$. However, for smaller values of r_c, the spreading resistance of the semiconductor R_b and the series resistance R_o of the connecting wires and semiconductor substrate must be taken into account. Then in general

$$R = R_c + R_b + R_o \tag{3-8}$$

where R_b and R_o depend on the particular geometry of the metal-semiconductor contact being characterized. For III-V semiconductors accurate determination of r_c is most often carried out using one of four methods [10]: 1) the Cox and Strack technique, 2) the four point method, 3) Shockley extrapolation technique or 4) the transmission-line model.

3.4.1. Cox-Strack method

The method of Cox-Strack utilizes the structure of Fig. 3-9, where the resistance of a circular contact of radius a on an n-type film of resistivity ρ and thickness t is to be determined. The current flow pattern is axial, through the layer to the heavily doped substrate. This structure requires metallization of both the back and the front surfaces of the semiconductor wafer, and can be used for either p- or n-type materials and for epitaxial or bulk layers. The specific contact resistance of the circular contact is

$$r_c = \pi a^2 [\, R - \frac{\rho}{a} F(\frac{a}{t}) - R_o] \qquad (3\text{-}9)$$

where F is a function of the ratio a/t and was found experimentally by Cox and Strack to have the approximate form

$$F(\frac{a}{t}) \approx \frac{1}{\pi} \arctan(\frac{2t}{a}) \qquad (3\text{-}10)$$

In practice, if the resistance of an array of contacts with differing areas is measured, the spreading resistance is calculated for each contact by using:

$$R_b = \frac{\rho}{a} F \qquad (3\text{-}11)$$

and a plot of $R\text{-}R_b$ vs. $1/a^2$ is made. A straight line fitted to the data points yields the values of r_c and R_o (r_c/π is the slope of the straight line and R_o is the intercept of the $R\text{-}R_o$ axis). The minimum value of r_c that can be accurately determined by this technique depends primarily on two factors: i) the accuracy in measurement of dimension a, and ii) the error in taking the difference between the two almost equal quantities R and R_b. For an n-type GaAs epitaxial layer with $a \geq 5\mu$, it is possible to measure r_c values down to approximately $1 \times 10^{-6} \Omega\text{-cm}^2$ with an error of about $\pm 25\%$.

3.4.2. Four point method

The four point method for measurement of r_c requires metallization of only one surface of the wafer as shown in Fig. 3-10. The layer being contacted is of thickness t and can be an epitaxial layer on a nonconducting substrate or a uniformly doped bulk wafer. The voltages V_1 and V_2 are measured for a known current I, assuming that the resistance of the semiconductor film between contacts is the same everywhere. The potential distribution in the plane of the semiconductor layer is logarithmic. The expression for the specific contact resistance is

$$r_c = \pi a^2 \left[\frac{V_1}{I} - \frac{V_2}{I}\frac{\ln(3s/2a - 0.5)}{2\ln 2} - R_b\right] \qquad (3\text{-}12)$$

If $a << s$, $t << s$ and $\rho a^2 \leq r_c t$, the contribution of R_b to R can ignored. The four point method has been used to measure values of r_c as small as $1.2\times10^{-6}\Omega\text{-cm}^2$ with about ±10% accuracy.

3.4.3. Shockley technique

For evaluation of ohmic contacts to thin semiconductor layers on nonconducting substrates, the Shockley technique can be used. As shown in Fig. 3-11, the technique consists of measuring the voltage drop $V_{(x)}$ along the surface of the semiconductor film between two planar ohmic contacts and using the extrapolated voltage V_o appearing across the contact to obtain the transfer length L_T by:

$$V_x = V_o \exp(-x/L_T) \qquad (3\text{-}13)$$

r_c is then found from:

$$r_c = R_s L_T^2 \qquad (3\text{-}14)$$

where R_s is the sheet resistance. The minimum value of r_c that can be accurately measured using the Shockley extrapolation method is limited by the error in determination of L_T. Assuming L_T could be measured to within ±1μ, it should be possible to measure r_c down to about $5\times10^{-7}\Omega\text{cm}^2$ with ±25% accuracy for ohmic contacts to n-type GaAs.

3.4.4. Transmission-line method

Another method to determine the resistance of ohmic contacts applied to a thin III-V semiconductor layer on a nonconducting substrate is the transmission line method (TLM). As shown in Fig. 3-12a, in the TLM the planar contact is treated as a resistive transmission line with uniform sheet resistance R_s and specific contact resistance r_c. In order to measure r_c using the TLM, one must first find experimentally the total resistance R_e of the contact and the epitaxial layer under the contact. This can be accomplished using the arrangement of Fig. 3-12b, where three identical ohmic contacts are spaced at unequal distance l_1 and l_2 along the surface of the layer. If R_1 and R_2 are the resistances measured, one can easily show that

$$R_e = \frac{-R_2 l_1 + R_1 L_2}{2(l_2 - l_1)} \tag{3-14}$$

The specific contact resistance r_c is

$$r_c = R_e^2 \frac{w^2}{R_s} \tag{3-15}$$

The ultimate accuracy of the TLM method is determined by the errors in measurement of l_1 and l_2 of Fig. 3-12b. Values of r_c of less than $3\times10^{-7}\Omega cm^2$ have been measured to GaAs. Finally the TLM has been extended to transmission lines of circular geometries and to arbitrary shapes. The use of the TLM avoids the necessity of measuring the $V_{(x)}$ distribution of the Shockley method and hence is somewhat simpler to implement.

Fig. 3-1 has been removed due to copyright restrictions.

Fig. 3-1 Energy-band diagrams of a metal and a n-type semiconductor separated by a large distance. The work function for the metal is ϕ_m [10].

Fig. 3-2 has been removed due to copyright restrictions.

Fig. 3-2 Variation of a) charge density, b) electric-field strength, and c) electrostatic potential with distance from metal/semiconductor interface according to the depletion approximation. d) Band diagram of an ideal metal-n-type semiconductor interface [10,11].

Fig. 3-3 has been removed due to copyright restrictions.

Fig. 3-3 Schottky barrier I-V characteristics for a circular metal film deposited on an n-type semiconductor [2].

Fig. 3-4a has been removed due to copyright restrictions.

Fig. 3-4a Energy-band diagrams of a metal and a p-type semiconductor separated by a large distance.

Fig. 3-4b has been removed due to copyright restrictions.

Fig. 3-4b Band diagram of an ideal p-type metal-semiconductor interface.

Fig. 3-5 has been removed due to copyright restrictions.

Fig. 3-5 Pinning of the Fermi level by surface states. All energy states below E_F are occupied [4].

Fig. 3-6 has been removed due to copyright restrictions.

Fig. 3-6 Band diagrams describing the Schottky theory of the metal-semiconductor interface. Four types of conductors are possible depending on the difference ϕ_m-ϕ_s and the semiconductor type. The arrows indicate majority-carrier current flow [10].

Fig. 3-7 has been removed due to copyright restrictions.

Fig. 3-7 Field and thermionic-field emission under forward bias. The diagram refers to a degenerately doped semiconductor for which ξ is negative [11].

Fig. 3-8 has been removed due to copyright restrictions.

Fig. 3-8 I-V characteristics of an ohmic contact [4].

Fig. 3-9 has been removed due to copyright restrictions.

Fig. 3-9 Measurement of the specific contact resistance r_c using the Cox-Strack method. The circular ohmic contact has radius a [10].

Fig. 3-10 has been removed due to copyright restrictions.

Fig. 3-10 Measurement of the specific contact resistance r_c by the four point method [10].

Fig. 3-11 has been removed due to copyright restrictions.

Fig. 3-11 Measurement of the specific contact resistance r_c by the Shockley technique. The voltage applied to the coplanar ohmic contact is V_a. The linear voltage distribution between the contacts is extrapolated to obtain the transfer length L_T [10].

Fig. 3-12a has been removed due to copyright restrictions.

Fig. 3-12a Measurement of the specific contact resistance r_c by the transmission-line model (TLM) technique. R_c is the total resistance of the metal-semiconductor interface and the epitaxial layer under the contact [10].

Fig. 3-12b has been removed due to copyright restrictions.

Fig. 3-12b A method of determining R_e using a linear array of unequally spaced ohmic contacts. The shaded regions are the contact areas [10].

Chapter 4 Formation, Structure and Properties of Metal/Semiconductor Contacts

The microstructures of metal/III-V compound semiconductor contacts are entirely dependent on the metallurgical system of choice and the contact process conditions. The metal/semiconductor contact morphology contains various intermetallic compounds of metal and A or B semiconductor element, and those compounds exhibit various geometrical shapes and distributions because of the structural incompatibility. Each phase has different carrier-conduction properties. Therefore, the carrier-transport nature of contacts, particularly in the cases of ohmic contacts to InP [6], is solely determined by the metallization chosen and the interfacial microstructure. The specific contact resistance may be reduced by several orders of magnitude simply by optimizing the thermal processing conditions to achieve a low contact resistance microstructure [24,25]. Because of the complexities of the reactions between metals and InP, and the lack of necessary information such as phase diagrams for ternary and quaternary systems, thermodynamic data (heat of formation, free energy change of formation, etc.), kinetic data (diffusibility, reaction rates) and crystal structures, at present, the fabrication of contacts is still more of an art than a science. Most of the publications in this field report the experimental results in particular contact systems, i.e., the formation techniques, the structures of contact layer and the corresponding contact properties. Thus, the review in this section is a collection of the published results with emphasis on the metal /InP contact system. Reaction of metals with other compound semiconductors are briefly summarized.

4.1. Gold-based metallizations

Au-based metallizations are the most widely used ohmic contacts to III-V semiconductors today. Au-based ohmic contacts present several advantages: relatively low specific contact resistance and low sheet resistance of the metallic layer, high resistance against corrosion, compatibility with standard evaporation and photolithography techniques, and quite good reliability at room temperature.

4.1.1. Au/InP contacts

Gold is used extensively as a metallization for compound semiconductors such as GaAs [26-31], GaP [32-35], InSb [36], GaSb [36,37] and InGaAsP [38,39]. For the reactions in Au/semiconductor contact systems mentioned above, Au acts as an oxidizing agent and displaces the group V elements in combining with group III elements to form various kinds of compounds. Similarly, in Au/InP contacts the dominant reaction in the ternary Au-In-P system is the one between the Au and the In, leading to formation of Au-In compounds. From binary Au-P and Au-In systems, it is known that there is one thermodyr amically stable Au-P phase (Au_2P_3) [40] and several binary thermodynamically stable Au-In phases (summarized in Table 4-1 [41-43]). The reactions of Au thin films with InP single crystal substrates have been reported by many groups [33, 34, 44-56].

The metallurgical reactions occurring in Au/InP are presented in Fig. 4-1a. The thermodynamic nature and the highly reactive nature of InP make reactions between Au and InP possible at very low temperature. Several groups [37,44-46] have reported that during gold deposition at room temperature, Au can react with both In and P. In and P out-diffuse substantially into the metallization with different diffusion rates. Hiraki [44] observed a fairly large amount of In atoms just after Au film deposition, and P atoms 100 min. after deposition, by Auger electron spectroscopy on the surface of a Au film (Au film was about 100nm thick in this case).

During annealing at 250°C-450°C, even though different Au-In compounds are observed by various research groups due to different processing conditions applied, the reaction process of Au-In-P can be divided roughly into three stages: i) Au-In solid solution formation, ii) Au_3In and Au_2P_3 formation and iii) Au_3In-to-Au_9In_4 transition. Each stage is controlled by a different mechanism. In the first stage (<300°C) the interaction of Au and InP begins with the entry of In and P into the Au via a dissociative diffusion process. Stage I continues until the In content in the Au reaches the solid solubility limit. This process is controlled by the vacancy generation rate at the free surface of the metallization. The P atoms, released when In enters the metal initially, remain unreacted and either leave the system or occupy nonlattice sites in the metal. Stage I proceeds very rapidly even at room temperature, but can be affected by the mechanical condition of the surface of the contact metallization. For instance, a SiO_2 capping layer on the free surface of the gold film suppresses the metal-semiconductor reaction rate by inhibiting the vacancy generation rate at that surface [52]. In the second stage (320°C-370°C), individual islands of Au_3In

(or Au_7In_2) nucleate and grow more or less uniformly over the metallization layer. The highly mobile In diffuses interstitially from the InP-metal interface to the front of Au_3In, and occupies substitutional sites in the metal lattice by displacing Au atoms. This is called a "kick-out" mechanism that results in an elevated concentration of highly mobile interstitial Au. These Au atoms become substitutional again by annihilating the vacancies that have been generated at the InP-metal interface during In diffusion into the metal. The Au atoms then react with unbound P, remaining there to form interfacial Au_2P_3. The rate-limiting step in this stage is the release of In from the InP and its insertion interstitially into the Au lattice. In entry continues until the metallization is converted from the saturated Au(In) solid solution to the compound Au_3In. In the third stage, the Au-InP reaction takes place with the result that Au_3In transforms to Au_9In_4 (or Au_2In). This transition is controlled by an Au-In exchange or kick-out process which takes place at the interface between the Au_3In phase and the Au_9In_4 phase. Meanwhile, the P released during this stage leaves the system unreacted.

In a closed Au/InP system, for a thin layer of Au (system composition is noted as "x" in Fig. 4-1b [46]), there are three phases when the system reaches equilibrium, i.e., Au_9In_4 (or Au_2In), Au_2P_3 and InP. But for an open Au/InP system, gas phase P will be generated from the system, with the evaporation of P increasing very abruptly above 550°C [57, 58]. The local composition near the contact area is changed. In rich Au-In compounds ($AuIn_2$ or Au_3In_2) are observed, with no additional Au_2P_3 forming in the system.

The Schottky barrier of a Au/InP contact remains stable up to 350°C annealing. Above this temperature, the Schottky barrier is catastrophically degraded due to Au-In and Au_2P_3 compound formation. A large two-to-three order of magnitude drop in the contact resistance occurs when Au/InP contact is annealed at 400°C [32]. At this point, the character of the contact changes from Schottky to ohmic [59].

4.1.2. Gold-based/InP contacts

Au-based metallization schemes provide the advantage of introducing an external dopant (either p-type or n-type) source, which can alloy into the adjacent semiconductor through solid or liquid phase reaction during annealing and form a p^+ or n^+ region. This highly doped region would then reduce the width of the depletion layer associated with the

potential barrier formed at the metal semiconductor interface. Tunneling of charged carriers in both directions across the interface would then be possible, making the contact essentially ohmic. The values of specific contact resistance r_c for several Au-based contacts are summarized in Table 4-2. The r_c of Au-based contacts is less than that of pure Au contacts. Au has a high solubility for In and the dopant element and can react with In and P to form several kinds of compounds, which makes InP decompose and dopant incorporation into InP relatively easy. Au-based contacts have to be annealed at a temperature between 350°C and 480°C in order to form a thin, heavily doped layer between the metal and the semiconductor.

For contacts to p-type InP substrates, Au-Zn [60-65] and Au-Be [64-70] have been commonly used. In the AuZn/InP system, the metallization layers are made by either depositing Au and Zn metal layers separately or co-depositing a Au and Zn mixture. The contact structures are Au/Zn/InP or Au-Zn/InP in the as-deposited specimens. Zn reacts with Au to form a AuZn phase during deposition. On annealing up to 340°C, both Au and Zn in-diffuse to the substrate and In out-diffuses to the metallization. It is found that Au diffuses into InP more rapidly than Zn does. Au reacts with Zn and P. AuZn transforms to Au_3Zn before Au-In phase formation (about 360°C). The contact resistance decreases and the contact becomes ohmic at about 380°C. The optimum specific resistance ($r_c=1.8\times10^{-4}\Omega cm^2$ with a doping level of $5.5\times10^{18}cm^{-3}$ in InP) is associated with the formation of a Au-In phase (Au_3In_2 or Au_9In_4) and Au_2P_3 in the temperature range of 420°C and 480°C. Meanwhile, Zn occupies the lattice sites created by In out-diffusion to create a layer of higher carrier concentration required for achieving lower contact resistance and also segregates in the Au_2P_3 clusters. At higher temperature (about 510°C), ZnP_2 forms and contact resistance increases again.

Because of the great difference in the vapor pressure of Au and Zn, and a very low sticking coefficient of Zn on III-V semiconductor surfaces, some specific technological problems, associated with the deposition and alloying of Au-Zn contacts can arise. Typical examples of the problems are preferential evaporation of Zn prior to Au deposition, poor adhesion, non-homogeneity of Au-Zn depositions and re-evaporation of Zn during the alloying of Au-Zn metallizations. As a result, Au-Be metallizations have been studied. The interactions between Au, Be, In and P in the Au-Be/InP system are very similar to those in the Au-Zn/InP system except no Au-Be and Be-P compounds form. To obtain ohmic properties and low specific contact resistance values, it is necessary to alloy the contact at elevated temperatures (above 400°C). The contact resistance decreases with increasing

annealing temperature. At about 420°C - 450°C, the contact is composed of Au_9In_4 and Au_2P_3 phases. Contact resistance can be as low as $8\times10^{-5}\ \Omega cm^2$ with a doping level of $1\times10^{18} cm^{-3}$ for p-InP substrates It is found that the Au/Be ratio influences the optimum heat treatment time and temperature but not the value of specific resistance. The minimum value of r_c is independent of the method of sample preparation and the amount of dopant alloyed into the InP surface with the Au film.

In addition to Au-Zn and Au-Be metallizations, Au-Mn [70], Au-Mg [71] and Au-Ni [72] systems have been applied to p-InP. The specific contact resistance for these contacts are $6\times10^{-4}\ \Omega cm^2$ with a doping level of $2\times10^{18} cm^{-3}$, $1\times10^{-4}\ \Omega cm^2$ with a doping level of $4\times10^{17} cm^{-3}$ and $9\times10^{-4}\ \Omega cm^2$ with a doping level of $2\times10^{18} cm^{-3}$ respectively.

Au-Ge metallizations are used for n-type InP substrates [67, 73-76]. The metallizations are based on a Au-12.5wt%Ge eutectic alloy. The Au-Ge contact was originally chosen for its low eutectic melting temperature (360°C). Alloying it at the eutectic melting temperature, drives the dissolution of InP. Then, In out-diffuses into the Au and Ge is likely incorporated preferentially on In sites, becoming a donor. When Au-Ge/InP is annealed at temperatures between 320°C and 450°C, the phase changes in the metallization are: $GeP \rightarrow GeP+Au_3In \rightarrow GeP+Au_3In+Au_2P_3 \rightarrow GeP+Au_9In_4+Au_2P_3$. The contact becomes ohmic after annealing at 320°C. At 375°C to 400°C the lowest specific contact resistance ($r_c=1\times10^{-7}\ \Omega cm^2$, InP substrate doping level $3\times10^{18} cm^{-3}$) is observed. Alloying the contact at 450°C and higher results in significant out-diffusion of P and enhanced formation of P vacancies. This leads to degradation of the contact electrical properties.

Au-Sn is another metallization that is used for n-InP contacts [77,78]. Au-Sn/InP contacts have ohmic behavior in a narrow alloying temperature range between 380°C and 410°C. The minimum specific contact resistance, $r_c=1.8\times10^{-6}\ \Omega cm^2$, is observed by annealing at 390°C for 30s. Au_4In, AuSn and polycrystalline InP are the main phases in the contact at alloying temperatures between 380°C and 410°C. Above 410°C the contact is composed predominantly of Au_3In .

It seems that the reaction processes for Au-based/InP contacts are similar to that of Au/InP contacts except for the formation of some M-Au, M-P or M-In binary phases (M=Zn, Sn or Ge). For instance, Au-In and Au_2P_3 binary phases form in the same temperature range as for the Au/InP system. The lowest values of specific contact

resistance for Au-based/InP contacts are obtained in those samples annealed in the temperature range of 390°C to 420°C, which is also the optimum temperature for Au/InP contact processing. Comparison of values of specific contact resistance (Table 4-2), for the n type InP specimens with the same doping level, shows that the r_c values of Au-based contacts are 1-2 orders of magnitude lower than those for pure Au contacts. This implies that doping by Sn or Ge is important in Au-based contacts.

Generally, there is a relatively thick Au layer on top of Au-based metallizations, which provides a low resistance contact to the rest of the circuit and protects the metallization from oxidation. On the other hand, the Au layer drives the undesired out-diffusion of P and the dopant element, which can degrade the electrical proprieties and decrease device reliability. Some results have demonstrated that these contacts degrade with time. Values of r_c increase by about 20% several weeks after initially testing [79]. In order to eliminate the problem, another metal layer is often deposited between the top Au layer and the Au-based contact to serve as a diffusion barrier for P and the dopant element. For instance, Au-Be/Cr/Au [70, 79], Au-Zn/TiW/Au [80] and AuGe/Ti/Au [81] metallization systems have been studied. It has shown that the diffusion barrier layer (Cr, TiW or Ti) not only prevents the out-diffusion of P from the semiconductor but also prevents the migration of Au from the top layer into the semiconductor during heat treatment. With the diffusion barrier, the dopant remains at the contact-semiconductor interface. The contacts do not degrade with time and, the reliability of devices indeed is superior to those without diffusion barriers. The electrical properties of these contacts are also given in Table 4-2.

All the Au-based contacts suffer from the same general disadvantages:

1. nonuniform depth of interaction (spikes of Au alloy penetration) and spatial composition, leading to nonuniform current density through the contact;
2. lack of long-term metallurgical stability;
3. poor morphology and edge definition;
4. relatively high specific contact resistances.

These deficiencies make Au-based contacts incompatible with the fabrication geometry of submicron planar devices or higher current density application devices.

4.2. Near noble transition metal-based metallizations

Near noble transition metal-based metallizations are introduced into ohmic contact schemes in order to overcome the deficiencies involved in the processing and performance of Au-based contacts to both p-type and n-type semiconductors, in particular, their unstable nature and lateral nonuniformity. Because of the more stable thermodynamic properties and less reactive nature of these metals, the near-noble transition metal-based metallizations provide a less reactive and more thermally stable contact microstructure during heat treatment at higher temperature. Their ohmic nature is obtained by both heavily doping the semiconductor layer under the metals and by the formation of narrow band gap intermetallic phases in the metal/semiconductor interface through a limited reaction when annealing the contacts.

4.2.1. Near noble transition metal element contacts

The first step toward understanding the behavior of a complex near-noble metal-based metallization system is to investigate the interaction between single metal layer and compound semiconductor substrates and to determine the role of the near-noble metal in the metallization system. The commonly used near noble transition metals in contacts are Ni, Pd, Co, Rh, Pt and Ir due to their particular properties, such as ease of deposition, low reaction temperature with III-V compound semiconductors, resistance to oxidation and compound formation with both A and B elements. It has been found that, in general, the final phases in contacts, which are in equilibrium with the AB substrate, are M-A or M-B (M=Ni, Pd, Co, Rh, Pt, or Ir).

Ni/GaAs contacts

The reactions between Ni and GaAs have received considerable attention since Ni is commonly used in ohmic contacts in combination with Au and Ge. The evolution of reactions of Ni films on GaAs is given by Fig. 4-2. Due to its low heat of vaporization (370.4kJ/mol) [33] and weak bonds, Ni can react readily with GaAs even during deposition [82,83]. At temperatures below 300°C, Ni penetrates a native oxide layer between the Ni film and GaAs, and reacts with GaAs to form a ternary phase Ni_xGaAs that is the first phase in the reactions. There is widespread disagreement in the literature as to the composition of the ternary phase. It is reported to be Ni_2GaAs [84-86], Ni_3GaAs [82,87,88] and to vary from $Ni_{2.5}GaAs$ to Ni_4GaAs [89,90]. The ternary phase has a

hexagonal structure with a=0.387nm, c=0.503nm. It is characterized by an epitaxial relationship with the GaAs substrate:

$[2\bar{1}\bar{1}0]$ Ni_xGaAs ‖ [011] GaAs
$(01\bar{1}2)$ Ni_xGaAs ‖ (011) GaAs

Ni atoms are found to be the dominant diffusing species during the ternary phase growth. After Ni is consumed completely, the ternary phase is uniform and remains so until above 400°C. Above 400°C Ga and As become mobile, leading to the decomposition of Ni_xGaAs into NiGa and NiAs. The grains of NiAs and NiGa are laterally spread, i.e., both NiAs/GaAs and NiGa/GaAs interfaces exist in approximately equal proportions [86,91]. NiGa and NiAs both have epitaxial relationships with GaAs [84-86,91]:

[100] NiGa ‖ [100] GaAs
(011) NiGa ‖ (011) GaAs
$[2\bar{1}\bar{1}0]$ NiAs ‖ [011] GaAs
$(01\bar{1}2)$ NiAs ‖ $(0\bar{1}1)$ GaAs

According to the Ni-Ga-As ternary phase diagram at 600°C (Fig. 4-3) [87], both NiGa and NiAs are in equilibrium with GaAs over a broad range of composition.

Pd/GaAs contacts

The metallization reactions of Pd/GaAs are depicted in Fig. 4-4. Pd is the most active element of all near-noble elements. It has the lowest value of heat of vaporization (357kJ/mol) [31] and the weakest bonds. Pd begins reacting with GaAs during deposition [92-94], forming a hexagonal ternary phase (a=0.672nm, c=0.340nm [92]). The reported composition of the ternary phase is variable, with several different compositions reported: $PdGa_{0.3}As_{0.2}$ [92], Pd_2GaAs [95], $Pd_5(GaAs)_2$ [93,96] and $Pd_2(Ga_{1-x}As_x)$ $(0.57 \leq x \leq 1)$ [94]. The orientation relationship of the ternary phase with GaAs is :

[0001] $Pd_5(GaAs)_2$ ‖ [011] GaAs
$(2\bar{1}\bar{1}0)$ $Pd_5(GaAs)_2$ ‖ (100) GaAs

$Pd_5(GaAs)_2$ is the dominant reaction product in the as-deposited state and after annealing at temperatures up to 315°C. Pd is the dominant moving species at these temperatures. It's diffusion toward GaAs results in complete dispersion of the thin native oxide layer [83]. A

second ternary phase, which is also hexagonal (a=0.92nm, c=0.37nm) [96], is the dominant phase in contact with GaAs at higher temperatures (350°C - 410°C). The composition of the second ternary phase reported by various groups is: $Pd_4(GaAs)$ [93,96], $Pd_{3.3}Ga_{1.2}As_{0.8}$ [83], $PdGa_{0.6}As_{0.4}$ [92] and $Pd_5(Ga_{1-x}As_x)_3$ ($0.16 \leq x \leq 0.47$) [94]. This ternary phase exhibits the following orientation relationship with GaAs:

$$[0001]\ Pd_4(GaAs) \parallel [011]\ GaAs$$
$$(\bar{2}\bar{1}30)\ Pd_4(GaAs) \parallel (100)\ GaAs$$

Further annealing results in the decomposition of the ternary phase and the subsequent formation of binary compounds. From the Pd-Ga-As phase diagram (Fig. 4-5) [97], the final equilibrium phases with GaAs are PdGa and $PdAs_2$. If significant As loss occurs during processing, only PdGa can be obtained in the contact [83,92,95,98-100].

Co/GaAs contacts

The reaction between Co and GaAs starts at 260°C. A thin amorphous layer forms at the interface of Co/GaAs [101,102]. The amorphous phase is stable kinetically below 280°C because the diffusion of Co in GaAs is much faster than Ga or As in GaAs [103,104]. Co rapidly diffuses through the amorphous layer into GaAs as an interstitial species. The amorphous layer crystallizes, on annealing at 300°C for long times (over 3 hours) or at higher temperatures, forming a highly oriented ternary phase Co_2GaAs with the B_{31} structure (orthorhombic) at the amorphous layer/GaAs interface [101,102,105-107]. The phase is sometimes called a solid-solution of CoAs [108,109] because it has an orthorhombic structure with a lattice parameter similar to that of CoAs. The orientation of Co_2GaAs with respect to GaAs is:

$$[010]\ Co_2GaAs \parallel [011]\ GaAs$$
$$(101)\ Co_2GaAs \parallel (011)\ GaAs$$

Annealing at 400°C for longer times (>24hours), results in the formation of two distinct layers. The one contacting GaAs is the ternary phase and the outer one is a mixture of CoGa and CoAs with no unreacted Co (Fig. 4-6). Once the mobilities of Ga and As are sufficient in the ternary phase (>500°C), the ternary phase will decompose into binaries, i.e., CoGa and CoAs. Both of these are found to grow epitaxially on GaAs:

[001] CoGa || [001] GaAs
(220) CoGa || (220) GaAs
[101] CoAs || [001] GaAs
(020) CoAs || (220) GaAs

CoGa and CoAs are stable phases with GaAs until 700°C if As is not lost from the contact surface. Fig. 4-7 shows the Co-Ga-As phase diagram at 600°C [110].

Rh/GaAs contacts

Reactions of thin Rh films to GaAs have been investigated by several groups [91,111,112]. The reactions are schematically represented in Fig. 4-8. No reaction is observed in as deposited specimens. At 200°C RhAs has formed at the interface of Rh/GaAs. Initially this phase is supersaturated with gallium. Ga replaces As in RhAs giving $RhAs_xGa_{0.5-x}$, where x=0.25-0.30 [111]. RhAs is highly textured and exhibits the following orientation relationship:

[110]RhAs || [011]GaAs
(001)RhAs || (100)GaAs

It is believed that Rh is the predominant diffuser through RhAs at low temperature because of the formation of Kirkendall voids at the Rh/GaAs interface. At temperatures above 300°C, RhAs decomposes, which is hastened by the formation of Kirkendall voids that reduce the diffusion flux of Rh to the reaction interface. Nucleation of RhGa occurs at the Rh/RhAs interface. The decrease in the diffusion flux of Rh through RhAs also brings about the nucleation of $RhAs_2$ at the RhAs/GaAs interface. RhGa and $RhAs_2$ grow and consume the supersaturated RhAs phase. Although RhGa is not in contact with GaAs, the same orientation relationship for RhGa and GaAs is observed [91]:

[011]RhGa || [011]GaAs
(011)RhGa || (100)GaAs

The texture observed for RhGa may be due to nucleation from the highly textured RhAs phase or may be a result of preferred growth, perhaps due to anisotropy of the diffusion kinetics. After annealing at 500°C and above, the Rh film is completely consumed and a layered structure $RhGa/RhAs_2/GaAs$ is obtained [111,112]. From the Rh-Ga-As ternary

phase diagram (Fig. 4-9)[113], this layered structure is stable after annealing the contact at 800°C.

Pt/GaAs contacts

Pt has a relatively high heat of vaporization (510kJ/mol) and stronger bonds than either Ni or Pd. Below 200°C, only an amorphous layer is observed between the Pt film and GaAs substrate [114]. Fig 4-10 shows schematically the morphological development during Pt/GaAs interfacial reactions. The initial stage of reaction involves the diffusion of Ga into the Pt layer, and reaction between Pt and As, resulting in the formation of an interfacial layer of $PtAs_2$ above 220°C [115]. The dominant relationship between the grains of cubic $PtAs_2$ and GaAs is [116]:

$$[011]\ PtAs_2 \parallel [011]\ GaAs$$
$$(1\bar{2}2)\ PtAs_2 \parallel (100)\ GaAs$$

After annealing at 350°C Pt_3Ga forms at the interface of $Pt/PtAs_2$, giving a layered structure sequence of $Pt/Pt_3Ga/PtAs_2/GaAs$ which remains until the unreacted Pt is consumed. With further annealing (>450°C), Pt becomes the primary diffuser in the contact. Pt diffuses through $PtAs_2$ from Pt_3Ga or the Pt layer to the $PtAs_2/GaAs$ interface to form $PtAs_2$. After the Pt layer is consumed, the continuous diffusion of Pt and Ga causes Pt_3Ga to transform to PtGa. The final phases in this contact are PtGa, PtAs and GaAs (Fig. 4-11) [117]. In contrast to Ni/GaAs and Pd/GaAs, there is no ternary phase formation in the Pt/GaAs contact reactions. It is noteworthy that the native oxide layer, which is originally at Pt/GaAs interface, is located within the reacted film after the reaction. This morphology indicates that both Ga and Pt are moving species in the reactions.

Ir/GaAs contacts

When Ir and GaAs are brought into contact at temperatures above 400°C, GaAs decomposes at the Ir/GaAs interface, thereby releasing Ga and As as separate species. Ga diffuses into Ir, whereas As remains at the Ir/GaAs interface and reacts with Ir to form $IrAs_2$ [118], which is the first phase in the system. (Fig. 4-12). Ga diffuses into Ir until the solubility is exceeded locally whereupon IrGa nucleates and grows. Strong texturing is obtained for the $IrAs_2$ phase with the orientation relationship:

$$[5\bar{2}1]IrAs_2 \parallel [100]GaAs$$
$$(11\bar{3})IrAs_2 \parallel (011)GaAs$$

In the 500°C to 650°C temperature range, Kirkendall voids are formed at the GaAs interface rather than on the Ir side, indicating that Ga and As are the moving species in the Ir/GaAs contact reaction. The layered sequence structure is Ir/IrGa/$IrAs_2$/GaAs, which indicates that Ga diffuses faster than As does. Above 700°C, the IrGa phase transforms into the more stable Ir_3Ga_5 phase in the presence of unreacted Ir [91,119]. The Ir-Ga-As ternary phase diagram is shown in Fig. 4-13 [120,121]. Instead of a ternary compound only a limited solution of As in Ir_3Ga_5 is found. The final layered sequence in the contact is Ir_3Ga_5/$IrAs_2$/GaAs until 1000°C.

In summary, there are indeed some similar characteristics involving the reactions of near noble metal/GaAs contacts:

1. If the metal is the predominant diffuser in the initial reaction stage, the reaction between metal and GaAs can occur at low temperatures. The first phase formed is not the final stable phase with GaAs, and will decompose into the final stable phases after Ga and As become mobile in the contact.
2. If Ga and As are the predominant diffusers in the reaction, the first phase formed is the final stable phase. The MAs phase layer contacts directly to GaAs, which indicates that Ga mobility is higher than As.
3. The first phases formed in the contacts have epitaxial relationships with GaAs substrate.

Table 4-3 list some characteristics of those contacts.

A summary of the electrical measurements of five near noble metal/GaAs diodes is given in Table 4-4 [122]. The values of ϕ_{Bn} are the highest ϕ_{Bn} of the diodes in a series of annealed diodes for each system. From the annealing temperatures at which these diodes are obtained, it is known that the contacts possess the highest Schottky barrier after the first (or second) metastable phases form. Further annealing leads to degradation in the Schottky barrier, which can be correlated to the formation of laterally irregular interface morphology, decompositions of metastable phases or interdiffusion of metal, Ga and As atoms.

Ni/InP contacts

Nickel is a common metal in ohmic contacts to InP, not only because it is widely used in the NiAuGe contact to n-type InP, but also because it shows potential on its own as an ohmic contact to n-type InP. For instance, Appelbaum et al [123] reported that evaporated Ni films exhibited low specific contact resistance on n-InP ($r_c=3\times10^{-6}\Omega cm^2$). All binary and ternary intermetallic compounds of the Ni-In-P ternary system, reported in

the literature, are listed in Table 4-5 [42, 124-129]. There are twelve Ni-In intermetallic phases, eight intermetallic Ni-P phases and three ternary phases in the Ni-In-P system. Three isothermal sections of the Ni-In-P ternary phase diagram, at 470°C, 600°C and 800°C respectively, are given in Fig. 4-14 [129,130]. The diagrams differ from each other because of two ternary phases with low melting points (526°C for Ni_2InP and 736°C for $Ni_{57}In_{22}P_{21}$) at which most ohmic contacts are formed.

Several groups have investigated the reaction of Ni films on n-InP during annealing at 200°C - 500°C in forming gas (5%H_2, 95%N_2) ambient [123,131,132]. After the contact is annealed for 15min at 200°C, initial reaction of Ni/InP contact system produces an interfacial amorphous layer. An electron diffraction pattern from this layer shows an intense halo corresponding to a spacing of 0.21nm. The composition of the amorphous layer, from energy-dispersive x-ray (EDX) analysis, is $Ni_{2.7}InP$. This amorphous layer crystallizes at above 300°C to form a hexagonal phase with the same composition $Ni_{2.7}InP$ (defined as $Ni_{57}In_{22}P_{21}$ by Shiau et al [129]). The lattice parameters for crystalline $Ni_{2.7}InP$ are a=0.412nm and c=0.483nm. After annealing at 360°C for 60min. 95% of the reaction layer consists mainly of the ternary phase (Ni_2InP), which is monoclinic with a=0.68nm, b=0.529nm, c=1.28nm and β=95°. This phase exhibits a strong crystallographic texture and orientation relationship with InP:

$$[001]Ni_2InP \parallel [100]InP$$

The other 5% of the contact layer is partially oxidized thin In films at the Ni_2InP grain boundaries. The Ni_2InP is stable at temperatures up to 500°C in specimens capped with SiO_2. A schematic presentation of morphology of Ni/InP contact described above is shown in Fig. 4-15. The Ni-InP reactions are extremely sensitive to annealing ambient, for example, the Ni-InP reaction is dominated by binary phases such as Ni_2P and Ni_2In if annealing takes place at temperatures above 300°C with direct exposure to a helium ambient [123]. The layer sequence is Ni-In/Ni-P/InP. For annealing temperature above 400°C, the contact structure is: In-O/Ni_2P/InP. Stremsdoerfer et al [132] reported that if annealing is done in an open-tube furnace in flowing dry nitrogen, the first phase is Ni_3P which changes to Ni_2P. From Ni-In-P phases diagrams the final equilibrium phases with InP, depending on the average composition of a given alloy, are In, Ni_2InP, Ni_2P or Ni_2P, Ni_5P_4 and NiP_2 below 526°C. Above that temperature binary phases, i.e., In, Ni_2P, Ni_5P_4 and NiP_2 may be in equilibrium with InP. The electrical properties of Ni/InP contacts consisting of only ternary phase morphology is not known yet, but for the Ni/InP

contact consisting of binary phase morphology, ohmic behavior appears at above 300°C with r_c being of the order of $10^{-6}\ \Omega cm^2$. This value of r_c remains constant for long times even at 500°C [132]. It is proposed that the Ni/InP contact becomes ohmic due to the existence of Ni_2P. Appelbaum et al [133] investigated the interaction of sputtered Ni_2P films on n-InP and p-InGaAs substrates and found that sputtered Ni_2P layers form ohmic contacts with low specific contact resistance on n-InP ($3\times10^{-6}\Omega cm^2$, $n=8\times10^{18}cm^{-3}$) and p-InGaAs ($2\times10^{-5}\Omega cm^2$, $n=3\times10^{18}cm^{-3}$). As a result, the Ni contact does not require additional dopants (Ge or Zn for n- or p-type respectively) to attain low specific contact resistance, thereby eliminating the need for a high temperature electrical activation treatment.

Pd/InP contacts

There has much interest in Pd thin films on InP substrates recently because several well known Pd-In refractory compounds may be formed, such as InPd, In_3Pd and In_3Pd_2 whose melting points are between 700°C and 1300°C. Pd or Pd based contacts on InP are expected to achieve thermal stability both during processing and in real applications. In contrast to Pd/GaAs contacts, very little has been done on the reactions between Pd and InP, specifically investigating morphology changes in Pd/InP contacts during processing. In Pd-In and Pd-P binary systems, there are seven Pd-In intermetallic compounds and eight Pd-P intermetallic compounds respectively [42, 129 134-138]. Mohney et al [139] have recently determined the Pd-In-P ternary phase diagram at 600°C by investigating bulk diffusion couples of Pd-InP specimens (Fig. 4-16). According to that phase diagram there are three Pd-InP ternary phases. Table 4-6 lists the binary and ternary compounds in the Pd-In-P system. In the limited work done on the Pd reaction with InP, similarities with the Pd/GaAs system are apparent. Diffusion of Pd into InP begins even before annealing [140]. With subsequent annealing at 175°C an amorphous ternary phase of approximate composition $Pd_{4.8}InP_{0.7}$ forms at the interface of Pd/InP. For samples annealed at 215°C-250°C, the morphology and composition are similar. The amorphous ternary phase crystallizes and is identified as a tetragonal phase Pd_5InP by TEM, EDX and SAD analysis. This ternary phase is the same as $Pd_{72}In_{14}P_{14}$ (which has a Pd_5TlAs-type structure) reported by El-Boragy et al [141]. The Pd_5InP layer is polycrystalline in morphology but shows a strong orientation relationship with InP substrate:

$$[020]Pd_5InP \parallel [022]InP$$
$$[\bar{1}10]Pd_5Inp \parallel [010]InP$$
$$[110]Pd_5InP \parallel [002]InP$$

$$(110)Pd_5InP \parallel (100)InP$$
$$(001)Pd_5InP \parallel (001)InP$$

Samples annealed with a SiO_2 capping layer have a variable composition ($Pd_{3-5}InP$) while samples annealed without capping layer are more uniform (Pd_xInP x=4.5-5). With further annealing (>450°C) Pd_5InP decomposes, and PdIn forms with two preferential orientations on InP:

$$[\bar{1}10]PdIn \parallel [022]InP$$
$$(110)PdIn \parallel (100)InP$$

and

$$[001]PdIn \parallel [002]InP$$
$$(100)PdIn \parallel (100)InP$$

Presumably P is lost to the atmosphere during processing. The morphology of the Pd/InP contact described above is shown in Fig. 4-17. Stremsdoerfer et al [142] investigated the reaction between Pd and n-InP in the specimens where Pd films are deposited by acidic bath. They reported that PdIn, Pd_2In and $PdIn_3$ appear in the contact but no ternary phase is found and the best value of specific contact resistance is 5×10^{-7} Ωcm^2 in the temperature range 300°C to 350°C. The r_c remains low until an annealing temperature of 500°C.

4.2.2 Near noble transition metal-based/GaAs contacts

Near noble transition metal-based/GaAs contacts are multi-elemental metallizations. There is a wide variety in contact structure, and the multi-elemental reactions to form the contact structures are complex. Despite this complexity, these reactions have three features in common: i) a group IV element, either Ge or Si, is a component of the metallization, ii) an electronegative metal in which Ga has a high solubility (e.g. Au or Pd) is also a component of the metallization and iii) the contact is annealed at a temperature between 300°C and 500°C. The result of the annealing treatment is expected to be the formation of a thin layer of n^+ type GaAs between the metal and the GaAs substrate, so that the contacts become ohmic.

AuGeNi/GaAs contacts

Of all the near noble transition metal-based contacts that have been reported in the literature, the AuGeNi based metallization is one of the most widely used ohmic contacts to n-type semiconductors (GaAs or InP). The contact structure of this traditional alloy system, before annealing, consists of the deposition of an eutectic (12.5wt% Ge) Au-Ge alloy and a nickel layer in various thicknesses with either the Au-Ge alloy layer or the Ni layer adjacent to the semiconductor. An epitaxial regrowth mechanism has been postulated to explain thermal reaction processes in this type of contact. Annealing such configurations at temperatures above or slightly below the eutectic temperature of the metallization-compound semiconductor system would result in the dissolution of the compound semiconductor and the subsequent precipitation or regrowth of a heavily doped or alloyed epitaxial layer. Consequently, ohmic properties of the Au-Ge-based contact are attributed to the formation of a Ge-doped GaAs layer by dissolution and regrowth. Ni was added originally to maintain a smooth surface morphology during the alloying process, but it was recognized later that Ni enhances the diffusion of Ge into the semiconductor, catalyzes the reaction of Au with the semiconductor, changes the wetting characteristics of the melt and improves the contact electrical properties.

A large number of papers have been published on the topic of metallurgical structure and the electrical properties of the AuGeNi/GaAs contacts [143-152]. During annealing at 250°C to 600°C, AuGeNi/GaAs contacts have a very complex structure. Various intermetallic compounds of Au, Ge, Ni, Ga and As are able to form, such as α-AuGa, β-AuGa, Au_7Ga_2, NiAs, Ni_2AsGe (or NiAs(Ge)), Ga_4Ni_3, Ni_3Ge and NiGe. The thermal reactions in the contacts are rather complex, and very much dependent on the as-deposited contact structure and the conditions used in the annealing process. Actually, the reported formation sequences, reaction products and their distributions in the literature are quite different from group to group. On the other hand, however, some common features for the reactions can be found by careful analysis of the reported experimental results. For the sake of benefit to further study, these common features are summarized in the following. During the initial stage of annealing (<300°C), Ga and As are immobile, whereas Ge diffuses rapidly toward the Ni layer to form NiGe or Ni_3Ge, and the Ni and Au diffuse toward the GaAs substrate. The contact is not ohmic at this stage. During the middle stage of annealing (300°C - 400°C), Ga and As become mobile. Although GaAs may be decomposed partially through its reaction with Ni, it is mostly decomposed through the interaction between Au and Ga. This is because Ga moves toward the surface to a larger extent than As does, creating Ga vacancies in the GaAs crystal. The products of

reaction are Au-Ga (including Au(Ga,As), α-AuGa; Au_7Ga_2), NiAs and NiGe. The contact resistance is still high ($>10^{-4}$ Ωcm^2) at this stage. With annealing at temperatures of 400°C and 500°C, more Ge, which has been trapped in NiGe phase, diffuses toward NiAs and GaAs to form Ni_2AsGe or NiAs(Ge), or enters the Ga sites in the GaAs crystal forming a heavily doped n-type layer. The morphology of the contact consists of binary β-AuGa grains and Ni_2AsGe (or NiAs(Ge)) grains. The lowest contact resistance is observed at this stage (about 10^{-6} Ωcm^2 or 0.08 Ωmm, $n=10^{18} cm^{-3}$). The mean values of the contact resistance and their spreads are found to be strongly influenced by the interfacial microstructure. The distribution of compounds in the contacts is found to be the key factor in determining the electrical properties of the contacts. The NiAs(Ge)/GaAs interface is important in lowering the contact resistance. The contact resistance is inversely proportional to the area fraction of NiAs(Ge)/GaAs interface [145], because a heavily doped n^+ GaAs layer can easily be formed at the interface by the diffusion of Ge across the boundary. The spread in resistance value is affected by the uniformity of the contact metal/GaAs interface. An ideal interface structure for a AuGeNi/GaAs ohmic contact with a small spread in contact resistance value, according to experimental results [152], is suggested to be a two-layer structure, with a high density of the NiAs(Ge) grains in the bottom layer contacting GaAs and a homogeneous β-AuGa phase in the top layer. Further annealing (600°C or 400°C for 90 hours) leads to the segregation of the NiAs(Ge) grains, reduction in the contact area between the NiAs(Ge) grains and GaAs substrate, and liquid-like flow of the β-AuGa phase due to the low melting point of β-AuGa (about 375°C). This deteriorates the interface uniformity, so that the contact resistance increases and electrical properties become poorer.

In spite of providing low resistance and excellent reproducibility, AuGeNi contacts have several disadvantages. For instance, the surface morphology of the contact is rough, the diffusion depth of the contact materials is deep and thermal stability after contact formation is poor above 350°C even though the contacts are prepared at temperatures higher than 400°C [155]. A lot of work has been done to improve the quality of AuGeNi contacts. One method to improve the morphology is to deposit a metal or alloy layer between the top Au layer and the AuGeNi metallization to serve as a diffusion barrier to reduce or prevent the in-diffusion of the overlayer metal (Au) into the interface region and out-diffusion of Ga, As and contact compounds. Lakhani et al [153] used a film of SiO_2 to passivate the AuGeNi metallization. They found the passivated metallization produce a smooth surface and interfaces, and consistent specific contact resistances of 3×10^{-6} Ωcm^2 ($n=2\times10^{17}$ cm^{-3}) over a wide range of annealing times and temperatures. Lustig et al [154]

added only 6nm of Au to a contact with a W layer on the top (conventional AuGeNi contacts contain Au layers thicker than 100 nm). The volume fraction of the low melting point β-AuGa compound is found to be reduced by a factor of about 100 as compared with conventional AuGeNi contacts (estimated from XRD results). The contact provides a resistivity less than 0.2 Ωmm after annealing at a temperature around 650°C for 30s. This contact (AuGeNi/W/Au) remains almost unchanged both electrically and morphologically after repeat heating to 400°C for 6 hours. In some other experiments, Ti, Mo, ZrB_2 and WSiN crystalline or amorphous layers have also been introduced as the diffusion barriers in the AuGeNi contacts [155-160].

In addition, other near noble metals, Pd or Pt, are used to replace Ni in contacts to improve the thermal stability of the contact. These elements and Ni belong to the same column in the Elemental Periodic Table, and are believed to be similar in performance in Au-Ge ohmic contact formation. Kazior et al [161] evaluated the temperature stability and long term reliability of AuGePd and AuGeNi ohmic contacts to n-GaAs ($n=10^{17}$ - 10^{18} cm^{-3}). They found:

1. A low resistance ($r_c=10^{-6}$ Ωcm^2) AuGePd contact can be achieved for a broad range of furnace (370-470°C) and flash annealing (390-430°C in graphite susceptor) temperatures.
2. AuGePd contacts stored for 4000 hours at 280°C show a much slower rate of increase in contact resistance compared to AuGeNi contacts.
3. The current in gateless FETs with AuGePd contacts does not decrease under bias-temperature stress measurement conditions (The devices biased under constant drain voltage were stored at a 200°C base plate temperature in a N_2 ambient for extended periods of time and the drain current was monitored at two hour intervals). In contrast, the current in the devices with AuGeNi contacts decreases more than 20% in 4000 hours at 280°C.
4. Failure analysis revealed significant electromigration along the drain fingers of devices with AuGeNi contacts, but no appreciable electromigration with AuGePd contacts. Therefore, the AuGePd ohmic contacts appear to be more thermally stable and more resistant to electromigration.

Zheng [162] found, in Au/Ag/AuGe/Pd/GaAs contacts, that Pd reacts with GaAs to form a ternary phase Pd_4GaAs at room temperature. Subsequent reaction of Ge with Pd_4GaAs at a relatively high temperature results in the decomposition of the Pd_4GaAs phase and the epitaxial regrowth of a Ge-doped GaAs layer. The contact resistance reaches $r_c=2\times10^{-6}$ Ωcm^2 at 500°C for 30s. The experimental results indicate that using Pd to replace Ni as the

first layer in the contact considerably reduces contact resistance ($r_c=10^{-5}\,\Omega cm^2$ for a Au/Ag/AuGe/Ni/GaAs contact in the same experiment) and provides good adherence to the substrate.

Au/Ni/Ge, Au/Pd/Ge and Au/Pt/Ge contacts on n-GaAs (annealed at 400°C for 30s) have been compared with one another [163]. It has been found that AuGa and $NiAs_2$ are present in Au/Ni/Ge contacts, GeAs and Ge_8Pd_{21} in Au/Pd/Ge contacts and $AuGa_2$ and Ge_3Pt_2 in Au/Pt/Ge contacts respectively. Au/Ni/Ge contacts have the largest grains (on the order of microns), Au/Pd/Ge contacts have smaller grains with sizes from several hundred nanometers to one micron and Au/Pt/Ge contacts have the smallest grains (submicron) and are very uniformly distributed. The best specific contact resistance obtained in the experiment is $9.02\times10^{-7}\,\Omega cm^2$ for Au/Pt/Ge contacts. Consequently, Au/Pt/Ge contacts are considered to be the best in terms of electrical characteristics as well as surface morphology in that investigation. A summary of specific contact resistances for AuGeNi(or Pd or Pt) systems discussed above is given in Table 4-7. It seems that all these contacts have low contact resistance even with different "recipes". However, the morphology, reproducibility and long term stability of the contact depend critically on the specific choice of layer sequence, layer thickness and processing conditions.

Pd-based/GaAs contacts:

Since AuGeNi contacts often result in a nonplanar interface morphology and the fast diffusion of Au in GaAs often leads to reliability problems, nonspiking low resistance ohmic contacts using Pd-based systems have been developed. In this contact system, the regrowth mechanism of heavily doped GaAs on the substrate is based on the reaction-driven decomposition of intermediate phases that occur in the solid state at temperatures well below the melting point of the interfacial phases, thereby producing laterally uniform regrown layers. The regrowth process can be described as follows [164]: Films of two elements M (as a metallic transport medium) and M' are deposited on a compound semiconductor substrate AB. The film adjacent to the substrate consists of a metal M that reacts at low temperatures to form a ternary phase M_xAB

$$xM + AB = M_xAB$$

The second film consists of an element M' that is chosen such that it reacts with M_xAB to form a compound MM'_y that is sufficiently stable so as to drive the reaction

$$(xy)M' + M_xAB = AB + xMM'_y$$

to the right . Because of the proximity of the crystalline AB substrate, epitaxial regrowth of AB is likely. Moreover, regrown AB may be doped or alloyed with M'. The contacts formed by this mechanism are more suitable for shallow junctions since no lateral or vertical spiking is involved and the contact metallization can be placed arbitrarily close to the gate region The Pd-based contact scheme involves the deposition of a metallic transport medium, Pd, onto which a layer of amorphous Ge or Si is then deposited. Usually, the contacts are annealed at temperatures between 300°C and 550°C in order to form a good ohmic contact with the lowest specific contact resistance.

In Ge/Pd/GaAs contacts, the contacts are rectifying in the as deposited state. The regrowth process begins with a limited low temperature reaction (about 100°C) between the Pd and the GaAs substrate to produce an intermediate Pd_4GaAs phase. The thickness of this phase is uniform and estimated to be about 10-15nm [165]. After annealing at 225°C for 30 min, the top Ge layer reacts with Pd to form PdGe at the interface of Pd/Ge. The lateral structure of the contact is Ge/PdGe/Pd_4GaAs/GaAs at this stage. The contacts exhibit poor ohmic behavior ($r_c=10^{-3}\ \Omega cm^2$, $n=10^{18}cm^{-3}$) [166]. A subsequent reaction at 325°C-350°C between the Ge overlayer and the intermediate Pd_4GaAs phase results in the decomposition of Pd_4GaAs phase and the epitaxial regrowth of a Ge-doped n^+GaAs layer (2nm thick) on the surface of GaAs substrate. The excess Ge is then transported across the PdGe layer and epitaxially grows on the GaAs [165-170]. The contact structure consists of PdGe/Ge/n^+GaAs/GaAs. A schematic representation of reactions in Ge/Pd/GaAs contacts is shown in Fig. 4-18. The contacts exhibit good ohmic behavior with $r_c=3\times10^{-7}\Omega cm^2$ [171]. Further annealing (over 450°C) deteriorates the electrical properties of the contacts because of the reaction between PdGe and GaAs, which consumes the n^+GaAs layer and forms a highly resistive layer. If processed by rapid thermal annealing (RTA), the contacts show higher reliability. The lifetime of contact, defined as the time to 10% deterioration, is estimated to be over 10^9 years at 70°C or 10^4 years at 150°C [172].

It is noteworthy that: i) Pd must initially be in contact with the GaAs substrate for low r_c ohmic contact formation with this system. In Pd/Ge/GaAs contacts, low temperature reaction only occurs between Pd and Ge. During contact processing, the reaction products are PdGa, $PdAs_2$, Pd_2Ge and PdGe. No ternary Pd_4GaAs and regrown n^+GaAs appear in the reaction, so that the contact resistance only reaches $10^{-5}\ \Omega cm^2$ [173,174]. ii) The ratio of Ge/Pd must be appropriate. The amount of Ge must be more

than the amount necessary for PdGe formation in order to form a low resistance ohmic contact. According to the Marshall et al [168] the ratio of thickness for Ge/Pd is 253:100.

The Si/Pd/GaAs contact system is in many ways similar to Ge/Pd/GaAs contact system. It is necessary that the Si/Pd atomic ratio be greater than 0.65 in order to obtain ohmic contacts [175]. During low temperature annealing, Pd_4GaAs and Pd_2Si form at the interfaces of Pd/GaAs and Si/Pd respectively. Ohmic behavior is obtained after annealing at 375°C for 30 min, with $r_c=2\times10^{-6}\ \Omega cm^2$ ($n=10^{18}cm^{-3}$) [175,176]. The contact consists of $Si/Pd_2Si/n^+GaAs$ at that stage. Schematic illustrations of the alloying sequence on Si/Pd/GaAs are given in Fig. 4-19 [176]. Si atoms incorporated in regrowth of GaAs are also realized by decomposition of Pd_4GaAs in which Si is dissolved. The difference in morphology between the Si and Ge based contacts is that the excess amorphous Si layer remains on top of Si/Pd/GaAs contact without being transported to the Pd_2Si/n^+GaAs interface.

The Si/Pd contacts offer satisfactory thermal stability and smooth interface and surface morphologies, but the contact resistance is a factor of about 10 higher than that for the Ge/Pd contacts. In order to make a good ohmic contact in Si/Pd system with contact resistance comparable to that Ge/Pd system, two modified Si/Pd contact schemes have been investigated [177]. A thin (about 1.5nm) layer of additional Ge or Si embedded in the Pd layer of the Si/Pd contact structure is used to reduce the contact resistance without causing a loss of thermal stability. The modified contact structures are Si/Pd/Si/Pd/GaAs and Si/Pd/Ge/Pd/GaAs respectively in the as deposited state. The contact resistance as a function of annealing temperature for Si/Pd, Ge/Pd, Si/Pd(Si) and Si/Pd(Ge) contacts and thermal stability for the Si/Pd(Si), Si/Pd(Ge) and Ge/Pd layer at 400°C are shown in Fig. 4-20[175]. The specific contact resistance values of Si/Pd(Ge) and Si/Pd(Si) contacts are $2\text{-}4\times10^{-7}\ \Omega cm^2$. The values increase to $4\times10^{-6}\ \Omega cm^2$ after annealing at 400°C for 50 hours, which indicates that thermal stability for these contacts is much higher than for the Ge/Pd contacts. The specific contact resistances of Pd-based/GaAs contacts reported in the literature are summarized in Table 4-8.

4.2.3. Near noble transition metal-based/InP contacts

Since near noble transition metal-based metallization have been employed successfully to fabricate ohmic contacts on GaAs devices, similar metallizations on InP

substrates have been investigated recently to determine the relationship between microstructural changes and electrical properties during processing.

AuGeNi/InP contacts

The situation for AuGeNi on InP is similar to that on GaAs. The interaction of the metallization and InP substrate is complex, and no universally applicable current transport model for this contact system has emerged yet. Since varying deposition contact structures are studied, such as Au-Ge/Ni [178,179], Ge/Au/Ni [72,180-182], Au/Ge/Ni [180], AuGe/Ni/Au [180,183,184], Ni/Ge/Au [185] and Ni/Ge/Ni/Au [64,186,187], the reaction products, the morphology and electrical properties are different from each other, as are the controlling factors for low contact resistance. From the results reported in the literature the characteristics of AuGeNi/InP contacts during processing are summarized in the following. The usual migrating tendency of elements in the contacts are: i) Ge moves from the Au-Ge layer to Ni layers during the initial reaction stage (200°C - 250°C); ii) Ni, separated from InP by other layers, in-diffuses to the surface of the InP substrate; iii) In out-diffuses to the Au layer or the surface of the contacts; iv) Au migrates to the InP substrate. The reaction products are NiGe [72,183,185], Ni_xP_y (including NiP, Ni_2P, Ni_3P, Ni_4P) [180,185,186], Ni_xInP [185], Au_xIn [185], Au_2P_3 [181,182], AuGeP [182], AuGeNiP [186] and In_2O_3 [186]. The annealing temperature range for obtaining ohmic contacts is 300°C - 450°C, the minimum specific contact resistances observed are 10^{-5}-10^{-8} Ωcm^2 (Table 4-9). The contact surface becomes non-uniform after higher temperature or longer time annealing, which leads to an increase and spread in contact resistance.

It is reported that no evidence of a Ge doped n^+ InP layer is observed, although Ge was present several microns into the InP [181]. Since the sharp drop in r_c for the Ni/InP, Ni/Au/InP and Ni/Ge/Au/InP contact systems occurred at the same temperature [72,180], it seems that the addition of Ge to the Au-Ni system is not necessary to achieve r_c values in the 10^{-8} Ωcm^2 range. Some investigators believe that it is Ni_xP_y phases that are responsible for the lower value of r_c in the contact systems [72,180,186]. Moreover, Anderson et al [182] suggested the appearance of a AuGeP layer at the interface acts as an effective barrier to the growth of Au_2P_3, making the contact morphology more uniform, so that the thickness and integrity of AuGeP are the principal factors controlling the contact ohmic character and stability. The formation of Au_2P_3 [181,182] or Au_xIn_y [185] phases at the interface of contacts breaks the contact morphology uniformity and degrades the electrical properties. In spite of the critical roles played by various reaction products in the AuGeNi/InP contacts described above, our understanding of the mechanism responsible

for AuGeNi/InP ohmic contact formation is far from satisfactory. Most of the recipes have been empirically optimized for low contact resistance but are rarely reproducible from one laboratory to another. Therefore, it is necessary to study systematically the details of metallurgical and electrical behavior of the contacts during annealing.

Pd-based/InP contacts

Very few investigations have been done, thus far, concerning the reaction products and electrical properties of Pd-based/InP contacts. Some of these have been carried out by means of Backside Secondary Ion Mass Spectrometry (sputter-etching from the semiconductor side) and transmission-line mode (TLM) electrical resistance measurement techniques [188-190]. The following reaction sequence is proposed in [188]. In Ge/Pd/InP contacts, Pd_2Ge forms during deposition. At 200°C a Pd-In-P alloy layer forms at the interface of Pd/InP. Subsequent processing at 350°C results in the dissolution of Pd-In-P and regrowth of 10nm thick liberated InP. Ge is detected in the regrowth region but not in InP substrate [188]. The contact structure is PdGe/Pd-In-P/n^+InP/InP. The specific contact resistance is $1.27\times10^{-5}\Omega cm^2$ ($n=5.3\times10^{18}$) [189]. In Si/Pd/(2nm)Ge/Pd/InP contacts [190], annealed at 200°C, the contact consists of Pd_2Si, PdGe and Pd-In-P. The SIMS depth profile shows that Ge is rejected by the Pd-In-P interfacial alloy and resides in the Pd-Ge layer. Upon further annealing (325°C for 30 min.), the profile shows a well-defined Pd-Si-Ge layer and intrusion of Si and Ge in Pd-In-P layer. The contact structure is Pd_2Si/Pd-Si-Ge/Pd-In-P/InP. No electrical results are reported in the investigation. The details of the relationships between reactions and electrical properties in Pd-based/InP contacts is not clear now. In addition, more work is required in order to understand the ohmic contact formation mechanism in Pd-based contacts.

In addition to application on n-type InP, Pd-based metallizations are employed to p-type InP. For instance, Pd/Zn/Pd/Au metallizations have been used to fabricate ohmic contacts on p-type InP [191]. Experimental results show a strong correlation between the electrical results and the microstructural changes that occurred during annealing. The initial decomposition of InP is driven by Pd at the InP surface, and not by Au at the contact surface at low temperature (<350°C). The first reaction product is an amorphous layer with a composition of Pd_2InP at the Pd/InP interface. The amorphous layer crystallizes and grows epitaxially on InP by 350°C. Meanwhile, Au in-diffuses to Pd_2InP and InP, In out-diffuses to the Au layer and Zn reacts with Pd forming a thin PdZn layer at the interface of Pd and Pd_2InP. The contact structure is Au(In,Pd,Zn)/Pd/PdZn/Pd_2InP(Au)/InP, and

the contacts are still Schottky barriers at this stage. At 450°C, Zn is liberated by PdZn decomposition and dissolves in the Au layer, in Pd_2InP and presumably in InP, which leads to a transformation to ohmic behavior with a minimum contact resistance value of $7\times10^{-5}\ \Omega cm^2$. Pd liberated during PdZn decomposition reacts with InP, by diffusing through the Pd_2InP layer, forming PdP_2 and Pd_2InP. The contact structure consists of Au(In,Pd,Zn)/PdP_2/Pd_2InP(Au,Zn)/InP; the morphology is laterally uniform. Further annealing results in formation of Au-In-Pd ternary layers at the contact surface and PdP_2/InP interface, which results in a break down of the uniform contact structure and an increase in the contact resistance. The contacts exhibit Schottky behavior again. The contact resistances of Pd-based metallizations on n- and p-InP substrates are also listed in Table 4-9.

GaAs and InP are both III-V compound semiconductors and have the same zinc-blende crystal structure. There are many similar features of the reactions in metal/GaAs contacts and in metal/InP contacts as described in this chapter, but the differences in reaction processes in the two system are indeed apparent. For instance, the reactions between Ni or Pd and InP result in the ohmic contacts. In contrast, the reactions of Ni or Pd with GaAs result in Schottky barriers. Therefore, one can not simply apply the experimental results of metal/GaAs contacts to metal/InP contacts. Compared with metal/GaAs systems, our knowledge of the relationship between reactions and electrical properties of metal/InP systems, both element/InP system and multimetallization/InP systems, is very limited. As the number of applications of InP increases, more techniques are being used to carry out further research work on the formation, structures and properties of metal/InP contacts.

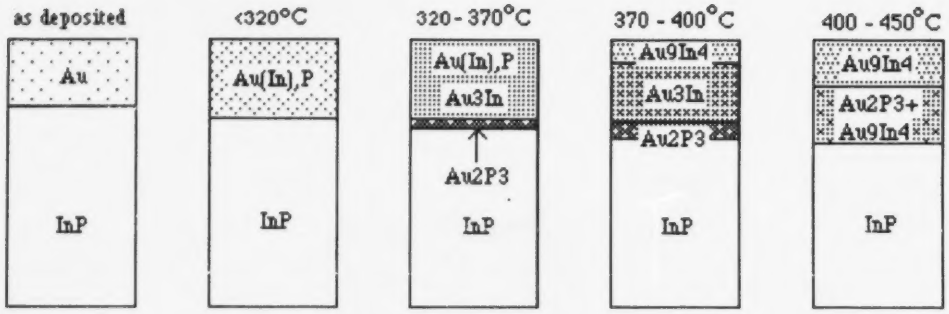

Fig. 4-1a Schematic representation of the reactions of Au films on InP substrates.

Fig. 4-1b has been removed due to copyright restrictions.

Fig. 4-1b Au-In-P phase diagram [47].

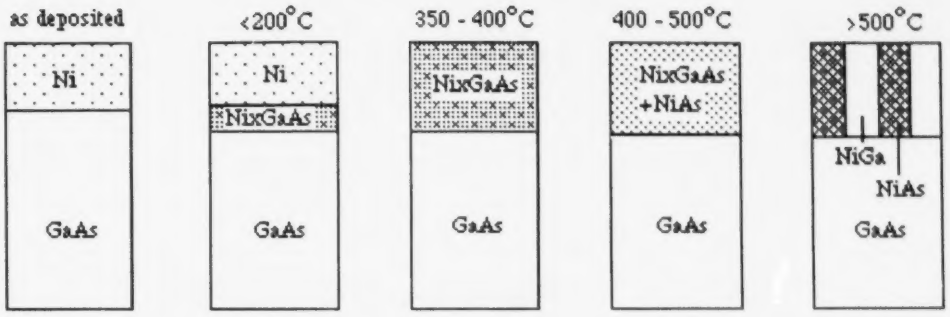

Fig. 4-2 Schematic representation of the reactions of Ni films on GaAs substrates

Fig. 4-3 has been removed due to copyright restrictions.

Fig. 4-3 Ni-Ga-As phase diagram at 600°C. Equilibria not determined by experiment are denoted by dashed lines [87].

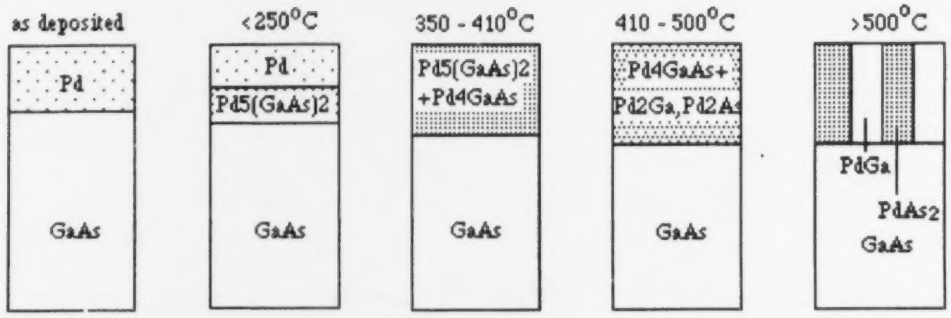

Fig. 4-4 Schematic representation of the reactions of Pd films on GaAs substrates.

Fig. 4-5 has been removed due to copyright restrictions.

Fig. 4-5 Pd-Ga-As phase diagram at 600°C [97].

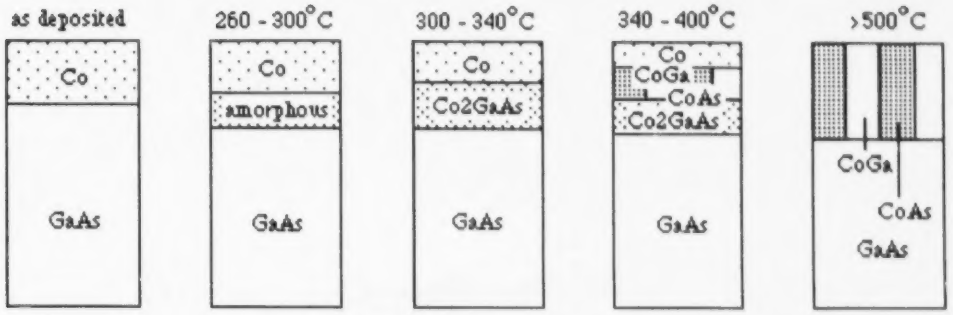

Fig. 4-6 Schematic representation of the reactions of Co films on GaAs substrates.

Fig. 4-7 has been removed due to copyright restrictions.

Fig. 4-7 Co-Ga-As phase diagram at 600°C. Equilibria not determined by experiment are denoted by dashed lines [106].

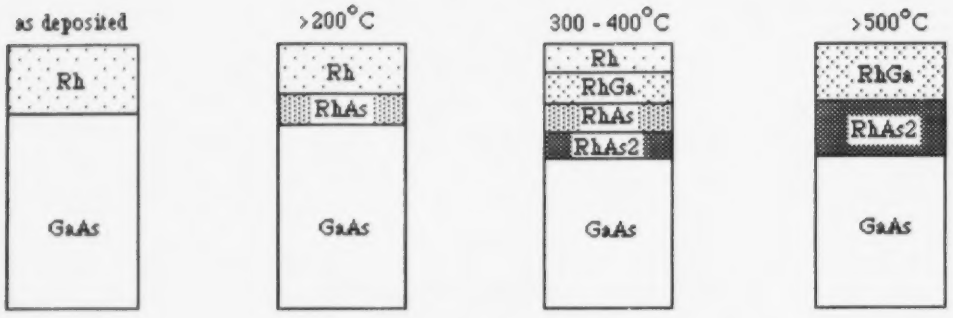

Fig. 4-8 Schematic representation of the reactions of Rh films on GaAs substrates.

Fig. 4-9 has been removed due to copyright restrictions.

Fig. 4-9 Rh-Ga-As phase diagram at 800°C. Equilibria not determined by experiment are donated by dashed lines [109].

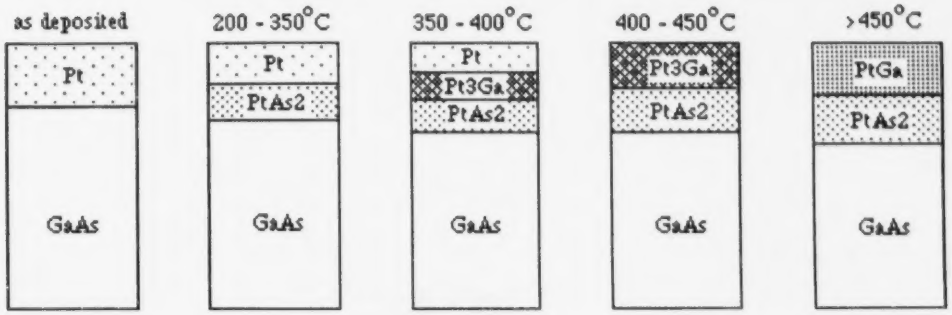

Fig. 4-10 Schematic representation of the reactions of Pt films on GaAs substrates.

Fig. 4-11 has been removed due to copyright restrictions.

Fig. 4-11 Pt-Ga-As phase diagram at 600°C. Equilibria not determined by experiment are denoted by dashed lines [113].

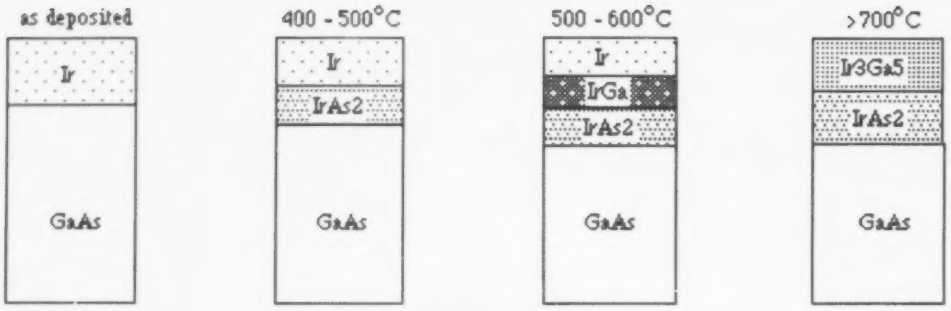

Fig.4-12 Schematic representation of the reactions of films on GaAs substrates.

Fig. 4-13 has been removed due to copyright restrictions.

Fig. 4-13 Ir-Ga-As phase diagram at 600°C. Equilibria not determined by experiment are denoted by dashed lines [116,117].

a) at 470°C

Fig. 4-14a has been removed due to copyright restrictions.

b) at 600°C

Fig. 4-14b has been removed due to copyright restrictions.

c) at 800°C

Fig. 4-14c has been removed due to copyright restrictions.

Fig. 4-14 Ni-In-P phase diagram at a) 470°C, b) 600°C and c) 800°C. Equilibria not determined by experiment are denoted by dashed lines [129,130].

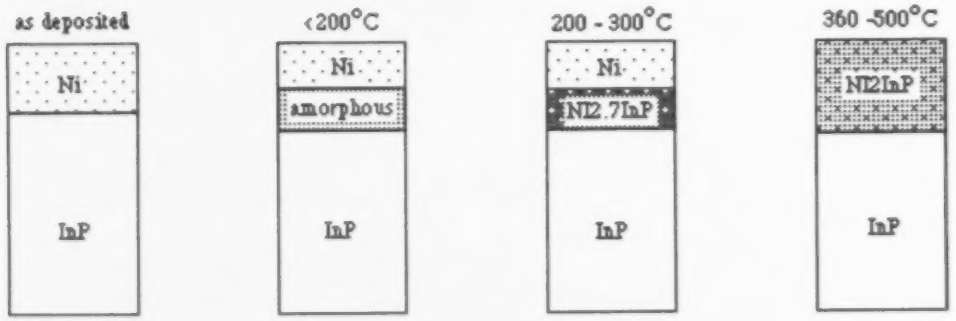

Fig. 4-15 Schematic representation of the reactions of Ni films on InP substrates[131].

Fid. 4-16 has been removed due to copyright restrictions.

Fig. 4-16 Pd-In-P phase diagram at 600°C [139].

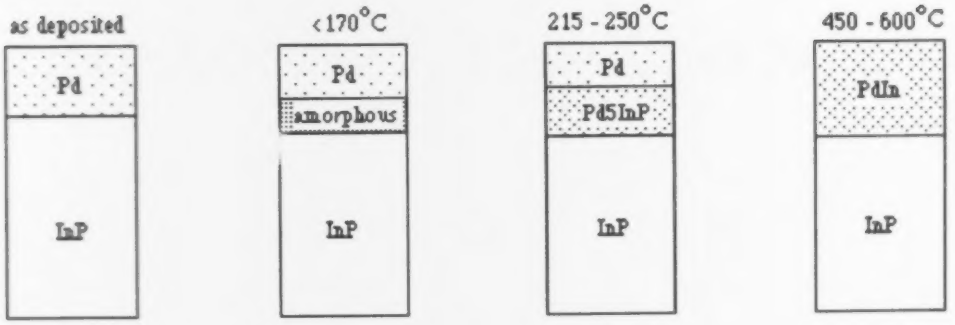

Fig. 4-17 Schematic representation of the reactions of Pd films on InP substrates [140].

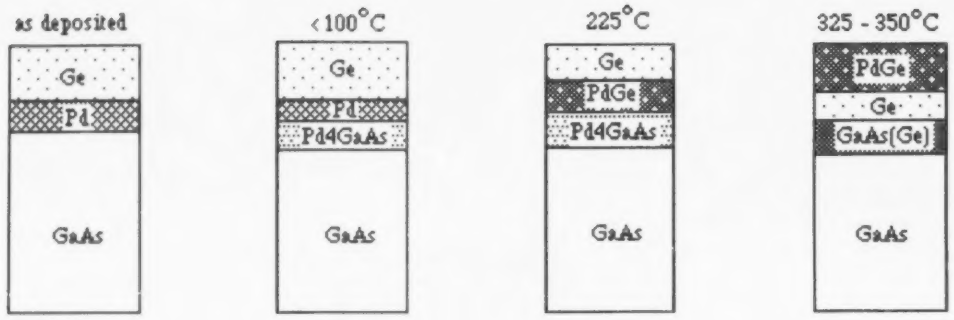

Fig. 4-18 Schematic representation of the reactions of Ge/Pd/InP contacts [165-170].

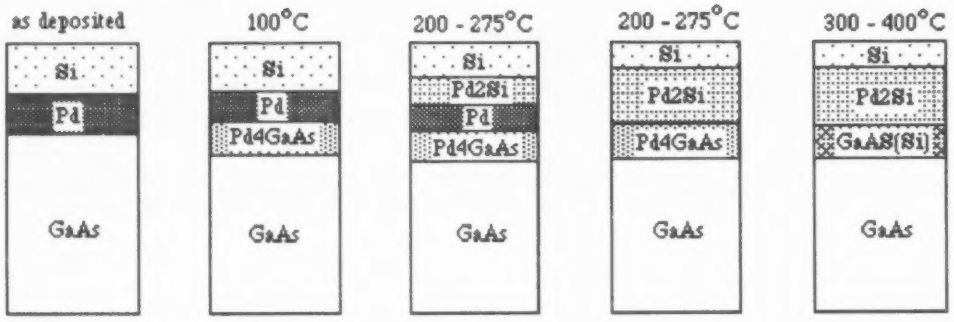

Fig. 4-19 Schematic representation of the reactions of Si/Pd/InP contacts [176].

Fig. 4-20a has been removed due to copyright restrictions.

Fig. 4-20a Contact resistance as a function of annealing temperature for the Si/Pd, the Si/Pd(Ge), the Si/Pd(Si) and the Ge/Pd contact systems. The annealing time at 350°C was 1 hour; 30s at 400°C and 10s at 500°C [177].

Fig. 4-20b has been removed due to copyright restrictions.

Fig. 4-20b Thermal stability for Si/Pd(Ge), Si/Pd(Si) and Ge/Pd contacts at 400°C. The initial anneals are 450°C for 30s for Si/Pd(Ge) and Si/Pd(Si) contacts and 325°C for 30 min. for the Ge/Pd contact respectively. The solid line indicates a degradation rate of $t^{1/2}$ [177].

Table 4-1 Au-In intermetallic compounds [40-42]

Phase	at %In	Formula	mp(°C)	ΔH kJ/mole Au	Pearson symbol	Structure type	Lattice Parameter nm
α	0-12.7	Au(In)	649-1064	0- -8.78	CF4	Cu	a=0.4106
α'	12-14.3	$Au_{87}In_{13}$	641-649	-13.54- -9.20	hP16	Ni_3Ti	a=0.2909, c=0.95
ξ	13-23	Au_7In	492-641	-8.78- -17.56	hP2	Mg	a=0.2917, c=0.4798
ξ_1	21.5-22.2	Au_7In_2		-16.72	hexagonal		a=1.053, c=0.4788
		$Au_{11}In_3$			OC28	$Cu_{11}Sb_3$	a=0.4784, b=2.0437,c=0.5071
	21.7-22.5	$Au_{10}In_3$			hP26	$Cu_{10}Sb_3$	a=1.0539, c=0.4786
ε ε'	24.5-25	Au_3In	481-492	-16.72- -17.97	OP8	β-Cu_3Ti	a=0.5864, b=0.4745, c=0.5165
γ'	29.8-30.6	Au_7In_3	457-487	-21.74	hP60	Au_7In_3	a=1.2215, c=0.8509
γ	28.8-31.4	Au_9In_4			CP52	Cu_9Al_4	a=0.9829
		Au_2In					
ψ	35.3-39.5	Au_3In_2	454-458	-28.84- -31.35	hP5	Ni_2Al_3	a=0.4538, c=0.5645
AuIn	50-50.1	AuIn	510	-44.73	triclinic		a=0.43, b=1.059, c=0.356
							α=90.54°, β=90°,γ=90.17°
$AuIn_2$	66.7	$AuIn_2$	541	-76.08	CF12	CaF_2	a=0.6507

Table 4-2 Au-based contact to InP

Metallization	InP	Doping level (cm^3)	Resistance r_c ($\Omega\ cm^2$)	Processing condition	Ref.
40nmAu/40nmZn/250nmAu	p	5.5×18^{18}	2×10^{-3}	420°C, 3min.	60
65nmZn/200nmAu	p	10^{16}	9.4×10^{-3}	430°C, 6min.	61
20nmAu/40nmZn/270nmAu	p	5.5×10^{18}	1.8×10^{-4}	420°C, 3min.	64
250nm (Au-Be)	p	5.5×10^{18}	2.2×10^{-4}	460°C, 3min.	64
80nm(Au-Be)/210nmAu	p	1×10^{18}	$\leq8\times10^{-5}$	420°C, 10min.	66
100nm(Au-Be)	p	1.5×10^{17}	1×10^{-3}		67
	p	1.3×10^{18}	2×10^{-4}		
100nm(Au-Be)/200nmAu	p	5.5×10^{17}	7×10^{-4}	420-430°C	68
	p	2×10^{18}	4.5×10^{-4}	3-4min.	
20nmMn/150nmAu	p	2×10^{18}	6×10^{-4}	450°C, 15s	71
400nmMg/160nmAu	p	6×10^{17}	1×10^{-4}	446°C, 50min.	72
40nmNi1/40nmAu	p	2×10^{18}	9×10^{-4}	400°C, 30s	73
300nm(Au-Ge)	n	3×10^{18}	1×10^{-7}	375°C, 30s	74
100nm(Au-Ge)/100nmAu	n	1.7×0^{17}	*0.07Ωmm	420°C, 30-270s	76
	n	1.6×10^{18}	*0.03Ωmm		
250nm(Au-Sn)	n	3×10^{18}	1.8×10^{-6}	390°C, 30s	77
60nmAuBe/50nmCr/300nmAu	P	5.5×10^{17}	1×10^{-4}	420°C, 4min,	69
	p	2×10^{18}	3.5×10^{-4}	420°C, 3min.	
80nmAuBe/20nmCr/200nmAu	p	1×10^{18}	5×10^{-5}	410°C, 3-4min.	79
25nmAuZn/50nmTiW/1000nmAu	p	1×10^{18}	3.7×10^{-5}	410°C, 30s	80
45nmGe/80nmAu/50nmTi/300nmAu	n	1×10^{18}	4×10^{-7}	480°C, 90s	81
200nmAu	n	1×10^{18}	5×10^{-5}	400°C, 60s	33

Table 4-3 Date summary: Ni, Pd, Co, Rh, Pt and Ir on GaAs

	Heat of Vaporization kJ/mol	Starting reaction temperature	First reacted phase	Structure of first phase	Orientation reactionship of first phase with GaAs	Decomposed temperature of first phase	Final phase with GaAs
Ni	370.4	As deposited	$Ni_{2-4}GaAs$	hexagonal	$[2\bar{1}\bar{1}0]$ Ni_xGaAs // [011] GaAs $(01\bar{1}2)$ Ni_xGaAs // (011)GaAs	400°C	NiAs NiGa
Pd	357.0	As deposited	$Pd_5(GaAs)_2$	hexagonal	[0001] $Pd_5(GaAs)_2$ // [011] GaAs $(2\bar{1}\bar{1}0)$ $Pd_5(GaAs)_2$ // (100) GaAs	250°C	PdGa $PdAs_2$
Co	376.4	260°C	Co_2GaAs	orthorhombic	[011]Co_2GaAs // [011]GaAs (101)Co_2GaAs // (011)GaAs	500°C	CoGa CoAs
Rh	493.0	200°C	RhAs	orthorhombic	[110]RhAs // [011]GaAs (001)RhAs // (100)GaAs	400°C	RhGa $RhAs_2$
Pt	510.0	220°C	$PtAs_2$	cubic	[011] $PtAs_2$ // [011] GaAs $(1\bar{2}2)$ $PtAs_2$ // (100) GaAs		PtGa $PtAs_2$
Ir	604.0	400°C	$IrAs_2$	monoclinic	$[5\bar{2}1]IrAs_2$ // [100]GaAs $(11\bar{3})IrAs_2$ // (011)GaAs		Ir_3Ga_5 $IrAs_2$

Table 4-4 Summary of electrical measurements on five types of diodes after annealing [122]

Metal-GaAs	Annealing temp. °C	Schottky barrier ϕ_{Bn} (V)	Leakage current at -0.4V (A/cm^2)
Ni-GaAs	220	0.886	5×10^{-6}
Pd-GaAs	250	0.869	1.5×10^{-6}
C0-GaAs	<300	0.854	6×10^{-6}
Rh-GaAs	300	0.848	1.5×10^{-5}
Pt-GaAs	350	0.940	8×10^{-7}

Table 4-5 Ni-In-P intermetallic compounds [42, 124-129]

Phase	at%Ni	mp (°C)	pearson symbol	structure type	Lattice parameter (nm)
Ni_3In	74.5 - 75.5	850	hP8	Ni_3Sn	a=0.532, c=0.424
Ni_3In			CP4	$AuCu_3$	a=0.375
Ni_2In	66.7	670	hP6	Ni_2In	a=0.4179, c=0.5131
$Ni_{13}In_9$	59.5 - 62.5	876	hP4	NiAs	
NiIn	49.5 - 50.5	860	hP6	CoSn	a=0.4545, c=0.4353
NiIn			CP2	ClCs	a=0.3060
Ni_4In			CI2	W	c=0.2929
Ni_3In_2			mP22		a=0.74, b=0.426, c=1.046,β=90
$Ni_{29}In_{21}$			mC44	In_3Pt_4	a=1.4646, b=0.8329, c=0.8977, β=35.35
Ni_2In_3	40 - 40.1	870	hP5	Al_3Ni_2	a=0.4396, c=0.521
$Ni_{28}In_{72}$	29.5 - 30	410	CI52	γ-Cu_5Zn_8	
Ni_3In_7			CI40	Ge_7Ir_3	a=0.918
$NiIn_2$			t*12		a=0.6199, c=0.6128
ξ- Ni-In	62 -66.97		monoclinic		4=0.418, c=0.512-0.518
Ni_3P	75	970	tI32	Ni_3P	a=0.8954,c=0.4386
Ni_5P_2	71.7	1175	hP168		a=1.322,c=2.4632
$Ni_{12}P_5$	70.5		tI34	$Ni_{12}P_5$	a=0.8646,c=0.507
Ni_2P		1106	hP9	Fe_2P	a=0.5864,c=0.3385
Ni_5P_4		850	hP36	Ni_5P_4	a=0.6789,c=1.0986
NiP			OP16	NiP	a=0.605,b=0.4881,c=0.689
NiP_2			CP12	FeS_2	a=0.54706
NiP_2			mC12	PdP_2	a=0.6366,b=0.5615,c=0.6072,β=126.22
NiP_3			CI32	As_3Co	a=0.80151
Ni_2InP		526	monoclinic		a=0.681,b=0.529,c=1.280,β=95
$Ni_{21}In_2P_6$			CF116	$Cr_{23}C_6$	a=1.1112
$Ni_{57}In_{22}P_{21}$		736	hexagonal		a=0.412,c=0.483
$Ni_{2.7}InP$					

Table 4-6 Pd-In-P intermetallic compounds [42, 128 134-138]

Phase	at%Pd	mp (°C)	pearson symbol	structure type	Lattice parameter (nm)
$Pd_{15}P_2$	89.2	799	hP17	$Pd_{15}P_2$	a=0.71067,c=1.70867
Pd_8P					
Pd_5P	81.9	771	mP24	Pd_9P_2	a=0.5004,b=0.7606,
$Pd_{4.5}P$					c=0.8416,β=95.63
Pd_6P	85.5 - 87.5	792	mP28	Pd_6P	a=0.5674,b=0.94409,c=0.821,β=110.41
Pd_6P			mC16		a=0.2837,b=0.9441,c=0.7695,β=90.2
Pd_3P	75 - 80	1047	OP16	CFe_3	a=0.5947,b=0.7451,c=0.517
Pd_7P_3	69.2	814	hR20	Pd_7P_3	a=1.1976,b=0.7055,
Pd_5P_2		860			
PdP_2	66.2 - 67.7	1150	mC12	PdP_2	a=0.6207,b=0.5857,c=0.5874,β=111.8°
PdP_3			CI32	As_3Co	a=0.7705
Pd_3In	74 - 75.2	1304-1365	tI2	In	a=0.407,c=0.38
Pd_2In	63.5 - 67.2		OP12	Co_2Si	a=0.5611,b=0.4218,c=0.8237
Pd_5In_3			OP16	Ge_3Rh_5	a=0.56,b=1.102,c=0.424
PdIn	48 - 61.5	1285	CP2	ClCs	a=0.326
Pd_2In_3	39 - 39.5	709	hP5	Al_3Ni_2	a=0.453,c=0.55
$PdIn_3$	25	664	cubic	$D8_{1-3}$	a=0.94144
Pd_5InP			tP7	Pd_5TlAs	a=0.393,c=0.692
$Pd_5In_2P_2$			tetragonal		a=0.8376,c=0.8158
$Pd_{3.8}InP$					

Table 4-7 Resistance of AuGeM (M=Ni, Pd or Pt)/GaAs contacts

Metallizations	Doping level cm^{-3}	Contact resistance Ωcm^2	Processing conditions	Ref
100nmAu-Ge/20nmNi/50nmAu	2×10^{17}	9×10^{-7}	410°C, 115s	145
20nmGe/20nmNi/200nmAu	1×10^{18}	5.6×10^{-6}	330°C, 100hrs	146
20nmGe-Au/20nmNi/200nmAu	1×10^{18}	1.6×10^{-5}	330°C, 100hus	146
100nmGe-Au/20nmNi	1×10^{18}	9.3×10^{-6}	330°C, 100hrs	146
100nmAuGeNi/AuNi	7.8×10^{17} 6.6×10^{18}	1.3×10^{-5} 2.7×10^{-6}	460°C, 3min.	147
120nmAu/40nmGe/150nmNi/600nmAu	8×10^{17}	8.6×10^{-6}	380°C, 15min.	148
25nmNi/32.5nmGe/65nmAu/10nmTi/100nmAu		2.56×10^{-7}	470°C, 60s	156
5nmGe/5nmNi/50nmAuGe/30nmMo/110nmAu	6×10^{18}	0.074Ωmm	380-480°C, 20s	157
5nmNi/45nmAu/20nmGe/50nmZrB_2/20nmAu		0.06Ωmm	440°C	159
5nmNi/20nmGe/25nmAu/100nmWSiN/75nmAu	2×10^{17}	2.9×10^{-7}	475°C,7s	160
130nmAu-Ge/36nmNi/200nmSiO_2	2×10^{17}	3×10^{-6}	360-450°C, 30min.	153
30nmPd/40nmGe/400nmAu	2×10^{17}	1×10^{-6}	370-470°C	161
5nmPd/100nmAuGe/100nmAg/100nmAu	2×10^{17}	2×10^{-6}	450-500°C	162
43nmGe/30nmPt/87nmAu		9×10^{-7}	450°C, 30s	163

Table 4-8 Specific contact resistance of Pd-based/GaAs contacts

Metallizations	Doping level cm^{-3}	Contact resistance Ωcm^2	Processing conditions	Ref
47nmPd/150nmGe	1×10^{18}	$3\text{-}5\times10^{-7}$	350°C, 30nim.	171
50nmPd/200nmGe	3×10^{18}	7.5×10^{-6}	570°C, 10s	172
50nmGe/50nmPd	1.5×10^{18}	3.5×10^{-5}	500°C, 2hrs	174
41nmGe/125nmPd	2×10^{17}	4×10^{-4}	550°C, 20min	173
75nmPd/100nmSi	1×10^{18}	2×10^{-6}	375°C, 30min	176
12.5nmPd/1-2nmGe/62.5nmPd/130nmSi		4×10^{-7}	500°C, 10s	177
12.5nmPd/1-2nmSi/62.5nmPd/130nmSi		2×10^{-7}	400°C, 30min	177

Table 4-9 Resistance of near noble transition metal-based/InP contacts

Metallization	Doping level cm^{-3}	Resistance Ωcm^2	Processing condition	Ref
150nm(Au-Ge)/30nmNi	8×10^{17}	0.09-0.16Ωmm	360-630°C, 30s	178
125nm(Au-Ge)/25nmNi		8×10^{-6}	375°C, 3min.	179
20nmGe/40nmAu/140nmNi	1.7×10^{18}	10^{-7}	400°C,<20min.	180
40nmAu/20nmGe/140nmNi	1.7×10^{18}	10^{-8}	400°C, <5min.	180
50nmGe/500nmAu/5nmNi	10^{15}	1.5×10^{-6}	330-390°C, 15min.	182
60nm(Au-Ge)/15nmNi/40nmAu	2×10^{18}	2×10^{-7}	430-450°C, 2s	183
50nm(Au-Ge)/75nmNi/100nmAu		8×10^{-7}	450°C, 25s	184
25nmNi/50nmGe/40nmAu	10^{17}	10^{-7}	400°C, 10s	185
25nmNi/50nmAu/25nmGe/5nmNi	$5\text{-}9\times10^{15}$	10^{-4}	450°C, 1min.	186
300nm(Au-Ge)/70nmNi	8×10^{17}	1.2×10^{-6}	350-400°C, 2min.	64
40nmNi/300nm(Au-Ge)/70nmNi	8×10^{17}	2.3×10^{-6}	400°C, 2min.	64
50nmPd/115nmGe	5.3×10^{18}	1.27×10^{-5}	300°C	189
*10nmPd/5nmZn/20nmPd/60nmAu	2×10^{18}	7×10^{-5}	420-425°C, 30-70s	191

* Contact to p-type InP substrate

Chapter 5 Experimental Methods

5.1. Experimental materials

Fe doped <001> oriented InP semi-insulating wafers were used as the substrates for the contacts. Au (99.9999%), Pd (99.995%), Ge (99.999%), Ti (99.995%) and Pt (99.995%) were used for multilayer metallization deposition.

5.2. Metal thin film deposition

Deposition of metal thin films on InP substrates was done at Bell Northern Research, Ltd. (BNR). For the multilayer metallizations, a 0.2μm thick layer of InP, doped to a level of $1\times10^{17}cm^{-3}$ with Si, was grown on InP using low pressure metallorganic chemical vapor deposition (MOCVD). The following conditions were used in the MOCVD process:

Growth pressure = 75 torr
Growth temperature = 630°C
P source = PH_3 @ 115 sccm
In source = trimethyl indium @225 sccm (660 torr)
Si dopant source = 100ppm Si_2H_6 in UHP H_2
total gas flow after H_2 dilution = 8.5 slm

The relatively low doping level was chosen in order to allow for measurement of the contact resistance using a transmission line method. Prior to deposition, the substrates were polished with 5%Br in CH_3OH solution and rinsed in methanol, degreased with a solution of equal parts HCl and H_2O, rinsed again and then etched and cleaned in a 1%Br in CH_3OH solution. The metals, i.e., palladium, gold and germanium, were rinsed in methanol. Metal layers were then deposited on the InP substrates by means of electron beam evaporation using a 10 kV beam at 100-500mA. The deposition sequences and layer thicknesses for this research were:

1. 60nmPd on semi-insulating InP substrates,
2. 25nm Pd/50nm Ge/40nm Au on the grown InP layers,
3. 10nm Pd/5nm Ge/25nm Pd and 10nm Pd/20nm Ge/25nm Pd on the grown InP layers.

Blanket layers were prepared for transmission electron microscopy, while other specimens were patterned for electrical measurement using a lift off technique in the form of circular contacts with gaps from 2.5μm to 175μm. After these specimens were

annealed, a further sequence of 25nm Ti/25nm Pt/250nm Au was deposited on the circular contact structure in order to reduce the influence of the metal layers' resistance on the measurements of contact resistance.

5.3. Annealing procedure

After deposition, wafers were sectioned into about 1cm×1cm pieces. The Pd/InP samples were sealed in Pyrex glass tubes under a vacuum of 10^{-4}torr and annealed at temperatures between 175°C and 500°C for various periods. The Pd/Ge/Au and Pd/Ge/Pd contacts were annealed in a flowing nitrogen ambient at temperatures ranging from 250°C to 450°C for various times. The annealing regime is listed in Table 5-1.

5.4. Microstructural characterization

5.4.1. X-ray diffraction experiments

Prior to transmission electron microscopy (TEM) analysis, all specimens were characterized by x-ray diffraction with Cu-K_α radiation. The x-ray diffractometer is comprised of a Rigaku-Denki D-F3 generator, a Philips PW1380 goniometer, a Philips PW1965/20/30 proportional counter, a PM8000/06/07 chart recorder and a PW/1370/00/01/60/61 circuit panel. The obtained x-ray spectra were identified by calculating the interplanar spacings according to Bragg's law and comparing with data from the JCPDS Powder Diffraction Files [192]. Phase growth and transformations were monitored by measuring changes in peak position and intensity in the x-ray spectra.

5.4.2. Transmission electron microscopy (TEM)

The microstructural features of the contacts after annealing were analyzed by TEM. The microscopes used in this experiment were a Hitachi H-600 TEM/STEM equipped with a Kevex, Be window Si x-ray detector; a JEOL-2010 TEM equipped with a Noran, ultra thin window, Ge x-ray detector; a Hitachi H-7000 TEM with an accelerating voltage of 125kV and a Philips EM-400 with an accelerating voltage of 120kV.

5.4.2.1. TEM specimen preparation

Both plan view and cross section TEM specimens were prepared using chemical and ion-milling techniques reported in the literature [73, 193]. The procedure for plan view specimen preparation included the following steps:

1. 3mm discs were cut from wafers with an ultrasonic cutter,
2. discs were polished from the InP side down to a thickness of about 200μm with 600 grit SiC abrasive paper,
3. the discs were dimpled from the InP side to a central thickness of about 50μm using a Gatan Dimple Grinder with 1μm diamond paste,
4. the discs were chemically thinned from the InP side to the point of perforation with a 0.5%Br in methanol solution,
5. final thinning was done by ion milling in a Gatan Duo Mill 600CTMP.

One or two Ar^+ ion guns were employed to sputter the sample at an angle of 13° to the horizontal, with an accelerating voltage range of 3-4kV; the ion gun current varied from 0.3mA to 0.4mA. The sputtering process depended on the location and thickness of the layer to be studied in the contacts.

The procedure for cross section specimen preparation was as follows [194]:

1. The samples to be examined were cut into 1.5mm×5mm slabs. Some InP slabs were also cut to the same dimensions to be used as filler materials.
2. Two slabs of each sample were glued together (face to face) with a silver-loaded epoxy. Three filler slabs were glued to each side of the sample pieces (Fig. 5-1) [194].
3. The structure was squeezed gently, to produce thin, bubble free glue layers, using a small vice. Most samples and vice were then cured in a furnace at 90°C for 1 hour.
4. After curing, the structure was polished with 600 grit SiC abrasive paper down to a thickness of about 600μm. A 3mm disc was cut from the structure using a Gatan ultrasonic disc cutter. This sample was further ground down to a thickness less than 200μm with 600 grit SiC abrasive paper.
5. One side of the disc was dimpled to about half the sample thickness, by means of a Gatan Dimple Grinder, with 1μm diamond paste. This side of the disc was then polished with the polishing wheel and the same polishing paste to produce a highly reflective surface.

6. The opposite side of the disc was dimpled until either a very small hole appeared or the center of the disc became optically transparent. The sample was then polished using the same method as in step 5.
7. The sample was ion milled using an Ion Tech or Gatan Duo Mill 600CTMP Ion Mill. Mounted on a cold stage by vacuum grease, the sample was kept cold with liquid nitrogen under a base pressure of $<10^{-6}$torr. Two Ar^+ ion guns were employed to sputter the sample with the same angle as in the plan view sample sputtering process, a 4kV accelerating voltage and a 0.4mA ion gun current for 45 minutes to 1 hour. The sample was rotated during the whole process to obtain a relative large, thin and flat foil of the desired area.

5.4.2.2. Phase identification

Because of the complexity of the contact metallurgy, structural information from selected area diffraction (SAD), convergent beam electron diffraction (CBED) and energy dispersive x-ray spectroscopy (EDX) was combined to identify phases that formed at the metal/InP interfaces. The Diffract v1.5b software, provided by Virtual Labortories, was used for simulating the diffraction (SAD and CBED) patterns.

Selected area diffraction (SAD)

One method of identifying polycrystalline and epitaxial growth phases was selected area diffraction (SAD). A single crystal diffraction pattern consists of a simple array of bright spots; each spot represents a set of lattice planes with the same d-spacing. A polycrystalline ring diffraction pattern is formed by a large number of small discrete areas, each with exactly the same atomic array, but at different orientations to one another. If the discrete areas have the same orientation, as with an epitaxial growth phase, the diffraction pattern is just like a single crystalline diffraction pattern.

Ring and spot SAD patterns were observed with the H-7000 TEM. The InP substrate served as an internal calibration standard in order to minimize the systematic error.

Convergent beam electron diffraction (CBED)

CBED patterns were obtained from both the H-7000 TEM and Philips EM-400 TEM. The smallest incident beam size obtained was 300nm in the H-700 TEM and 40nm

in the Philips EM-400 TEM respectively. Camera constants were determined using the same methods discussed above.

Energy dispersive x-ray spectroscopy (EDX)

The H-600 and JEOL-2010 TEMs were used for energy dispersive x-ray spectroscopy to analyze the composition of individual layers and phases. The composition in a given phase can be determined by:

$$\frac{C_A}{C_B} = K_{AB}\frac{I_A}{I_B} \tag{5-10}$$

or

$$\frac{X_A}{X_B} = K_{AB}\frac{I_A W_B}{I_B W_A} \tag{5-11}$$

where, C_A and X_A are the concentration of element A in weight percent and atomic percent respectively, as are C_B and X_B for element B. I_A and I_B are the intensities from element A and B in the EDX spectrum, and K_{AB} is the Cliff-Lorimer proportionality factor. The K_{AB} factors are independent of specimen composition and thickness but dependant on instrument conditions. In this experiment, approximate compositions were determined using appropriate Cliff-Lorimer "K" factors. These were determined using a standardless approach or from appropriate standards [196].

5.4.3. Specific contact resistance measurements

Electrical measurements were only made on multilayer metallizations; the Pd/InP metallization was only studied to better understand its reactions with InP. Contact resistances were measured at BNR using a modified transmission line method. In the more commonly used transmission line model with rectangular contacts, the current flow at the edge of the contacts can significantly affect the contact resistance measurement results due to the nonuniform current flowing. A mesa etch is required to eliminate the unwanted current flow pattern. By using the circular test pattern, all the current is confined and flows uniformly from the positive to the negative, because of the inherent self-isolation of the circular symmetry, which eliminates the need for the mesa and therefore simplifies the fabrication procedure [197]. Measurements of specific contact resistance r_c were carried out with a circular transmission line resistor with varying gaps as shown in Fig. 5-2. The

geometry factors, in the circular contacts, for resistance measurement are listed in Table 5-2. The voltage drop ΔV across the separation d in the test pattern is given by Eq. (5-12) [198]:

$$\Delta V \cong \frac{i_o R_s}{2\pi}\left[\ln\frac{r_1}{r_1-d} + L_T\left(\frac{1}{r_1}+\frac{1}{r_1-d}\right)\right] \qquad (5\text{-}12)$$

where, i_o is the test current, R_s is the semiconductor sheet resistance (Ω/square), r_1 and r_1-d are the radii of the contacts (μm) and L_T is the transfer length (μm). Eq. (5-12) can be rewritten as:

$$R_{mes} = \frac{\Delta V}{i_o} = \frac{R_s}{2\pi}\ln\left(\frac{r_1}{r_1-d}\right) + \frac{R_s L_T}{2\pi}\left(\frac{1}{r_1}+\frac{1}{r_1-d}\right) \qquad (5\text{-}13)$$

Where R_{mes} is the test structure resistance (Ω).

If $y = R_{mes}$, $a_o = R_s$, $a_1 = R_s L_T$, $X_o = \frac{1}{2\pi}\ln\left(\frac{r_1}{r_1-d}\right)$ and $X_1 = \frac{1}{2\pi}\left(\frac{1}{r_1}+\frac{1}{r_1-d}\right)$, then

$$y = a_o X_o(x_L) + a_1 X_1(x_L) \qquad (5\text{-}14)$$

The method of least squares was then used to obtain the values of a_o and a_1, i.e., R_s and $R_s L_T$. The specific contact resistance r_c is obtained from the following:

$$r_c = L_T^2 R_s \qquad (5\text{-}15)$$

The viability of Eq. (5-12) requires that r_1 and r_1-d be greater than L_T by at least a factor of 4; otherwise, errors can occur due to the linear approximation. For contact structures with finite circular pattern radii, smaller values of L_T can reduce error. This eliminates any necessary correction, because of the relationship between L_T, r_c and R_s:

$$L_T = \left(\frac{r_c}{R_s}\right)^{1/2} \qquad (5\text{-}13)$$

A lower doping level in the semiconductor can reduce the value of L_T. The contacts in this experiment were deposited on the 0.2μm thick layers of InP (10^{17}cm^{-3} doped level),which had been deposited on top of the semi-insulating Fe doped InP substrate. The contacts consisted of a 50μm diameter contact in the center surrounded by a second contact. The

separation d between the two contacts varied from 2.5 to 175μm. The test structure resistances were obtained from i_o and the voltage drop across the contacts measured by a four point probe (two probes as a current source and two to measure the voltage drop). The resistance values obtained from these four contacts were then used to extract the sheet resistance R_s, transfer length and the specific contact resistance r_c by the method described above.

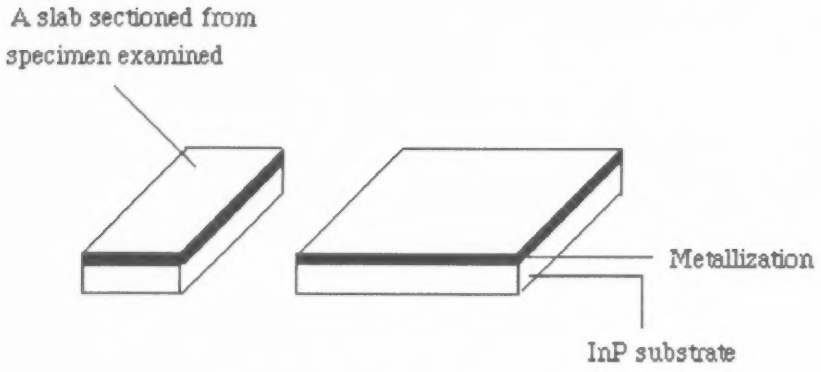

Fig. 5-1a Schematic showing a slab cut from an annealed specimen. The thicknesses for both the metal film and InP substrate are not to scale [194].

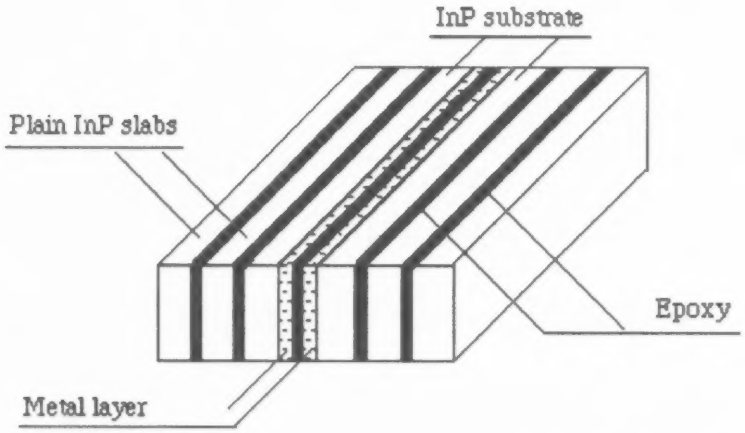

Fig. 5-1b Composite of specimen slabs, plain InP slabs and epoxy. The dimensions are not to scale.

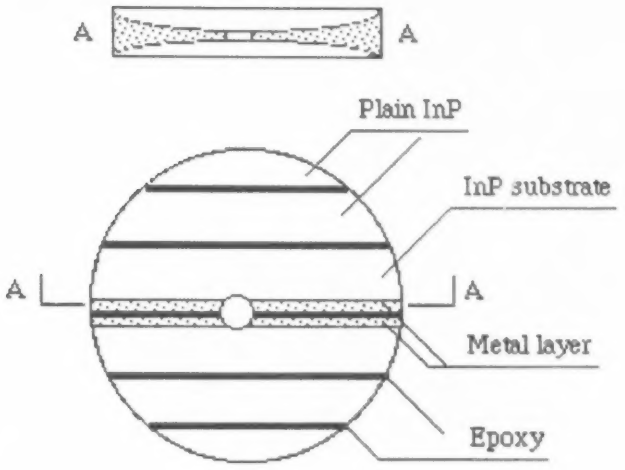

Fig. 5-1c Schematic showing the dimpled and polished composite disc (not to scale).

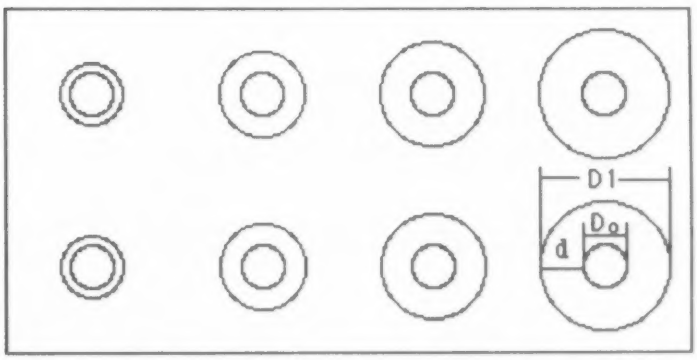

Fig. 5-2 Circular test pattern for contact resistance measurement.

Table 5-1 Annealing regime

60nm Pd		25nm Pd/50nm Ge/ 40nm Au		10nm Pd/5nm Ge/ 25nm Pd		10nm Pd/20nm Ge/ 25nm Pd	
Temp. (°C)	Time (min)	Temp. (°C)	Time (s)	Temp. (°C)	Time (s)	Temp. (°C)	Time (s)
175	5	250	5	250	10	250	10
225	5	250	10	250	20	250	20
225	8	250	20	250	40	250	40
225	15	250	40	250	80	250	80
275	5	250	60	250	120	250	120
350	5	250	90	250	160	250	160
350	30	250	120	250	320	250	320
350	120	250	180	300	5	300	5
350	1440	325	5	300	10	300	10
400	5	325	10	300	20	300	20
400	30	325	40	300	40	300	40
400	90	325	60	300	60	300	60
400	180	325	90	300	90	300	90
400	360	325	120	300	120	300	120
400	720	325	180	300	180	300	180
400	1440	350	5	350	10	350	10
450	5	350	10	350	20	350	20
500	5	350	20	350	40	350	40
500	30	350	40	350	80	350	80
500	60	350	60	350	120	350	120
500	1440	350	90	350	160	350	160
500	21000	350	120	350	320	350	320
		350	180	400	5	400	5
		400	10	400	10	400	10
		400	20	400	20	400	20
		400	40	400	40	400	40
		400	80	400	60	400	60
		425	10	400	90	400	90
		425	20	400	120	400	120
		425	40	400	180	400	180
		425	80	400	360	400	360
		450	10	400	720	400	720
		450	20	425	5	425	5
		450	40	425	10	425	10
		450	80	425	20	425	20
				425	40	425	40
				425	60	425	60
				425	90	425	90
				425	120	425	120
				425	180	425	180
				425	360	425	360
				425	90min		
				425	120min		
				425	180min		
				425	300min		
				425	720min		
				450	60		

Table 5-2 Geometry factors in planar contacts

D_0 (μm)	D_1 (μm)	d (μm)
50	55	2.5
50	90	20
50	200	75
50	400	175

Chapter 6 Reactions between Pd thin films and InP

6.1. Reactions between Pd thin films and InP

The Pd layer in the as deposited specimen was uniform (≈53 nm thick) and exhibited <111> preferred orientation perpendicular to the InP surface. Palladium reacted with InP during deposition, forming an amorphous layer (≈13 nm thick) with a variable composition - Pd-rich near the amorphous layer/Pd interface and Pd-poor near the amorphous layer/InP interface. The overall composition was close to, but slightly less than, Pd_3InP (Fig. 6-1). Amorphous phase formation in the Pd/InP system has been reported previously, [140,199] as noted above, and the composition reported here lies within the same range. Any compositional variations may be a result of different annealing environments and/or relatively poor accuracy in determining k factors (at least in our experiments). For convenience, the amorphous phase is referred to as Pd-In-P.

Pd-In-P grew and remained amorphous on annealing to about 225°C. The amorphous layer at this point was approximately 60 nm thick, while the remaining Pd layer was about 30 nm thick. The first signs of crystallinity were detected in specimens annealed for 5 min at 225°C. Crystalline islands, with a Pd content similar to that of the amorphous phase, nucleated at the InP surface in the amorphous layer (Fig. 6-2a). It was not possible to determine the particle composition accurately, since the x-ray spectra, obtained from plan view specimens, included information from the amorphous matrix as well as the particles. The islands grew epitaxially on InP with a crystal structure that matched very well with the $L1_2$-type structure. Five orientations were obtained; two of these are shown in Fig. 6-2b. The lattice parameter and orientation behavior (with respect to InP) of the crystalline phase were the same as reported previously for a Pd-In-P ternary phase (Pd_2InP) in a Au/Pd/Zn contact to InP [191]. For this reason the crystalline phase is believed to have a composition closer to Pd_2InP than Pd_3InP and is, therefore, referred to as Pd_2InP. A lattice parameter of 0.415 nm was determined as well as the following epitaxial relationship:

$$(100)\ Pd_2InP \parallel (110)\ InP$$
$$[001]\ Pd_2InP \parallel [001]\ InP$$

The islands had a pyramidal shape, with the sides making an angle of ≈50° with the InP surface, suggesting preferred growth along {111} planes.

The islands grew together with further annealing, as is evident from the series of micrographs and diffraction patterns ([001] orientation) shown in Figs. 6-2 and 3, from samples annealed at 225°C for 5, 8 and 15 min respectively. There is no apparent change in the composition of Pd_2InP. Several interesting features are evident from Fig. 6-2 and 3, however. First of all, the amorphous ring, which is quite prominent in the diffraction pattern for the 5 min specimen, gradually disappears as the crystalline phase grows and consumes the amorphous layer. Pd_2InP forms a continuous layer (≈40-50 nm thick) after annealing for 15 min. (Fig. 6-3a). The amorphous layer has not been fully consumed at this point (30-40 nm remain) and remnants of the original Pd layer (10-15 nm) are still present. The Pd_2InP pattern appears to be present for all the annealing times shown, but additional spots are prominent for the 15 min anneal (Fig. 6-3b). The additional spots are interpreted as being from another phase, most likely the particles (≈5–15 nm in size) shown in the image in Fig. 6-3c (15 min). The extra spots appear to match with the tetragonal Pd_5InP phase, which was discussed in chapter 4. Three orientations ([001], [110] and [$\bar{1}$10]) are superimposed on the Pd_2InP pattern, as demonstrated in the computer generated pattern in Fig.6-4 We were unable to index some of the spots, although, overall the match was quite good. One other orientation ([013]Pd_2InP - not shown) was obtained and agreement with the calculated SAD pattern was also quite good. Assuming that this phase is Pd_5InP, the following orientation relationships can be inferred:

$[001]Pd_5InP \parallel [001]Pd_2InP$
$(020)Pd_5InP \parallel (020)\ Pd_2InP$
$[110]Pd_5InP \parallel [001]Pd_2InP$
$(003)Pd_5InP \parallel (\bar{1}10)Pd_2InP$
$[\bar{1}10]Pd_5InP \parallel [001]Pd_2InP$
$(003)Pd_5InP \parallel (110)Pd_2InP$

The limited spatial resolution of the microscope prevented any detailed composition analysis of the particles, although they did contain Pd, In and P and were Pd-rich. We were, therefore, unable to determine whether the particle composition matched that of Pd_5InP. Also, in the image of the 15 min specimen (Fig. 6-3c), there is a 'boundary' type structure, which may be remnants of the amorphous phase and represents regions of contact of the growing crystalline islands. The majority of the particles appear to precipitate at these boundaries, as is evident from the dark field image in Fig. 6-3d.

All of the Pd layer layer was consumed by 275°C and the amorphous layer was fully crystalline. The microstructure at 275°C resembled that at 225°C (for 15 min.), although the extra spots (due to Pd_5InP) in the diffraction pattern were more prominent, indicating an increase in the volume fraction of Pd_5InP. X-ray microanalysis of this sample yielded an average composition for this layer of $Pd_{\sim 2.4}InP$ (suggesting a volume fraction of $Pd_5InP \approx 10$-15%). This composition included contributions from Pd_2InP and Pd_5InP, which we were unable to separate because of the size and distribution of Pd_5InP particles in the Pd_2InP layer.

Structural changes began to occur at 350°C for annealing times greater than 5 min. Gradual transformation to another ternary phase of approximately the same composition as the first crystalline phase took place (Fig. 6-5). This phase is referred to as Pd_2InP(II) here. The structure (cubic) and lattice parameter (a= 0.830 nm), as well as the epitaxial behavior, were identical to those reported previously [199]. Pd_2InP(II) was stable to about 400°C.

At 400°C, Pd_2InP(II) decomposed into PdIn (cubic) and PdP_2 (monoclinic). Decomposition was completed after annealing for 3 hours at 400°C. PdIn and PdP_2 continued to grow with further annealing and were stable even after annealing at 500°C for 350 hours (verified by x-ray diffraction). The only change in microstructure was in the size and distribution of the phases (Fig. 6-6). PdIn and PdP_2 were, therefore, in thermal equilibrium with InP (for a closed system). PdP_2 was unstable in air, however, resulting in phosphorus loss at room temperature. Fig. 6-7 shows micrographs of a specimen annealed at 500°C for 30 min. Fig. 6-7a shows a micrograph, of the specimen, taken very soon after annealing, and Fig. 6-7b shows a micrograph of the same specimen examined several days later. The PdP_2 regions have become quite porous, due to the loss of P.

6.2. Discussion

6.2.1. Amorphous formation

The first reaction product in the Pd/InP system is a Pd-In-P amorphous phase that starts to form during Pd deposition and continues to grow when the contacts are annealed at temperatures below 225°C. Usually an amorphous material can be produced by three methods, i.e., a rapid quenching of a melt, chemical or physical vapor deposition, and low

temperature solid state reaction. The Pd-In-P amorphous phase is achieved by both Pd vapor deposition and low temperature solid state reaction. From Refs. 201 and 202, solid state amorphization is governed by a combination of two factors, i.e., rapid diffusion of one constitute of a diffusion couple in the other and a large negative value for the heat of mixing between the two constituents. Among the two factors, fast diffusion is considered to be more important. In the Pd/InP case, both In and P atoms are essentially immobile whereas Pd can move easily when the system is annealed below 250°C. This is because InP has a zinc blende structure whose packing factor is 0.34 whereas palladium has a fcc structure with a packing factor of 0.74. Therefore, InP has a more open structure. This condition allows rapid diffusion of Pd into InP substrate. Even though an accurate diffusion constant of Pd in InP is not known, it can be roughly estimated from the following argument. From the diffusion constant of Pd in the GaAs ($2.36\times10^{-12}cm^2/s$ at 450°C [202]), it may be inferred that the diffusion constant of Pd in InP should be $\geq2.36\times10^{-12}cm^2/s$. This is because the melting point of InP (1070°C) is lower than that of GaAs (1238°C). Moreover, the lattice constant of InP (0.587nm) is larger than that of GaAs (0.565nm), while the density of InP ($4.79g/cm^3$) is smaller than that of GaAs ($5.32g/cm^3$). All these comparisons suggest that the activation energy for Pd diffusion in InP should be smaller than that in GaAs. As a result, Pd should have a larger diffusivity in InP than in GaAs. On the other hand, the diffusion constant for In and P in InP are $3.8\times10^{-20}cm^2/s$ and $7.6\times10^{-28}cm^3/s$ at 450°C respectively [302]. Therefore, the diffusion constant for Pd in InP at 450°C are 7 and 15 orders of magnitudes larger than those for In and P, respectively. Although the heat of mixing for Pd-In-P formation is not known at this point, according to the comparison of the diffusivities above, it is believed that the formation of Pd-In-P amorphous is due to rapid diffusion of Pd in InP.

The Pd/amorphous layer and amorphous layer/InP interfaces are quite smooth, because palladium has a strong ability to penetrate the laterally non-uniform native oxide layer which is always present under conventional device processing conditions. The uniform amorphous layers at the InP surface are beneficial in the fabrication of high quality contacts. First of all, the amorphous layer provides good metallization adhesion to the InP substrate, which is necessary for producing a contact with good electrical and physical properties. In addition, with further annealing, the amorphous layer transforms into the crystalline phases, either epitaxial growth of Pd_xInP or polycrystalline binary phases (PdIn and PdP_2), maintaining uniform contact morphology.

Thus far, only palladium and nickel are known to be able to penetrate the native oxide layer on InP surface during low temperature annealing. The study by Sands et al [83] demonstrates that palladium is superior to nickel in its ability to penetrate laterally non-uniform native oxide layers. Therefore, the use of palladium in the ohmic contact is more desirable due to the requirement for uniform morphology.

6.2.2. Ternary phase formation

Three different ternary phases (as well as an amorphous phase) have been identified in this study. Crystallographic data for these phases, as well as the binary phases that form at higher temperatures, are summarized in Table 6-1. These are, in order of formation, Pd_2InP, Pd_5InP and Pd_2InP(II). All three phases have been identified in previous studies [140,191,199], although not in the same study (the Pd_2InP and Pd_2InP(II) were identified by our group, while the Pd_5InP was identified by Caron-Popowich et al [140]). Differences in annealing environments (vacuum vs. inert or forming gas) and annealing temperature range may be, at least in part, responsible for any discrepancies.

The first ternary phase detected here (Pd_2InP) had been detected in ref. 191, after low temperature annealing (200-400°C) of a Au/Pd/Zn contact metallization to InP. The structure is $L1_2$-type, with a lattice parameter and orientation relationship corresponding to that in ref. 191.

The second ternary phase to form (Pd_5InP) was the only crystalline ternary phase detected by Caron-Popowich et al in their study of Pd/InP reactions [140]. Their annealing was done over a similar temperature range as this study. In ref. 140, they show an indexed diffraction pattern, consisting of three orientations of Pd_5InP on [100] oriented InP, which looks very much like the one shown in Fig. 6-3b (15 min at 225°C) and reproduced schematically in Fig. 6-4. A schematic of their pattern is shown in Fig. 6-8a. The actual SAD pattern could not be reproduced because of its poor quality. In fact, it is virtually impossible to see the reflections, which are close to the transmitted spot, so there is some question as to the exact position of these spots. We agree with their indexing of the Pd_5InP spots, but question their indexing of InP. Some of the diffraction spots that are assigned to InP cannot possibly match. These would have to be 100 and 110 spots, which are, of course, forbidden reflections. It is more likely that the improperly indexed spots correspond to lower order reflections from the three orientations of Pd_5InP. The computed pattern shown in Fig. 6-8 is proposed, with three orientations of Pd_5InP ([001], [110] and

[$\bar{1}$10]) superimposed on [001] InP. Note, that the lower order reflections (those close to the transmitted spot) are shifted slightly relative to the pattern shown in Fig. 6-8. Another possibility is that the two phases represented by the diffraction pattern, from ref. 140, are Pd_5InP and Pd_2InP and not Pd_5InP and InP. From the information given in ref. 140, we cannot distinguish between the two possibilities.

The reason Pd_5InP forms after Pd_2InP is not clear. Presumably Pd_2InP forms first because of kinetic considerations, i.e., it is closer in composition than Pd_5InP to the amorphous phase. Pd_2InP has a lower Pd content relative to the amorphous phase from which it forms. Initial Pd_2InP formation takes place at the InP/Pd-In-P interface, where the Pd content is the lowest compared with anywhere else along the thickness of the Pd-In-P layer. Palladium is rejected and accumulates ahead of the Pd_2InP growing front. It is assumed that at the reaction temperatures involved (≈225°C), Pd is the predominant diffusing species. The last portions of the amorphous phase to crystallize are Pd-rich, which results in the formation of Pd_5InP in the 'boundary' region of Fig. 6-3c.

$$\text{Pd-In-P} \rightarrow Pd_2InP + x\ Pd$$
$$x\ Pd + \text{Pd-In-P} \rightarrow y\ Pd_5InP$$

The above equations are not balanced. Additional Pd is provided through diffusion from the original deposited layer, so that the following reaction is also likely:

$$2\ Pd + InP \rightarrow Pd_2InP$$

Pd_5InP and Pd_2InP later decompose, forming Pd_2InP(II) according to the following:

$$2\ Pd_5InP + 3\ InP \rightarrow 5\ Pd_2InP(II)$$
$$Pd_2InP \rightarrow Pd_2InP(II)$$

The ternary phase reaction sequence is shown schematically in Fig. 6-9.

The structure of Pd_2InP(II) (referred to as Pd_2InP in ref. 199) has been studied in detail [199]. Pd_2InP(II) has a complex cubic structure with 16 Pd atoms, 8 In and 8P atoms per unit cell. Its structure very much resembles that of Pd_2InP, possessing a lattice parameter twice that of Pd_2InP. The higher degree of order in Pd_2InP(II) shows up as the

additional spots in the [013] oriented diffraction pattern (see Figs. 6-2b and 6-5). Pd_2InP(II) was the only ternary phase identified in ref. 199 due presumably to the limited annealing range (250-450°C) in that study. However, re-examination of SAD patterns from the low temperature anneal (250°C) in ref. 199 indicate the presence of weak diffracted intensity, which can be attributed to Pd_5InP.

In the 350-450°C range, Pd_2InP(II) is the only phase remaining on InP - the Pd layer has been completely consumed and Pd_2InP and Pd_5InP have decomposed. Annealing above 400°C, leads to Pd_2InP(II) decomposition to PdIn and PdP_2.

$$2\ Pd_2InP(II) + InP \rightarrow 3\ PdIn + PdP_2$$

6.2.3. Pd-In-P phase diagram

From our long term annealing experiments, we can draw, at least, the Pd-poor portion of the isothermal section of the Pd-In-P phase diagram (Fig. 6-10). This portion is excellent in agreement with that of the Pd-In-P phase diagram determined recently by Mohney et at [139]. They used Pd and InP powders as starting meterials. The samples were annealed up to 600°C. The phases were determined by wavelength dispersive spectroscopy and x-ray diffraction techniques. However, we are unable, at this time, to determine the Pd-rich portion of the diagram, because of the limitation in variation of sample's compositions.

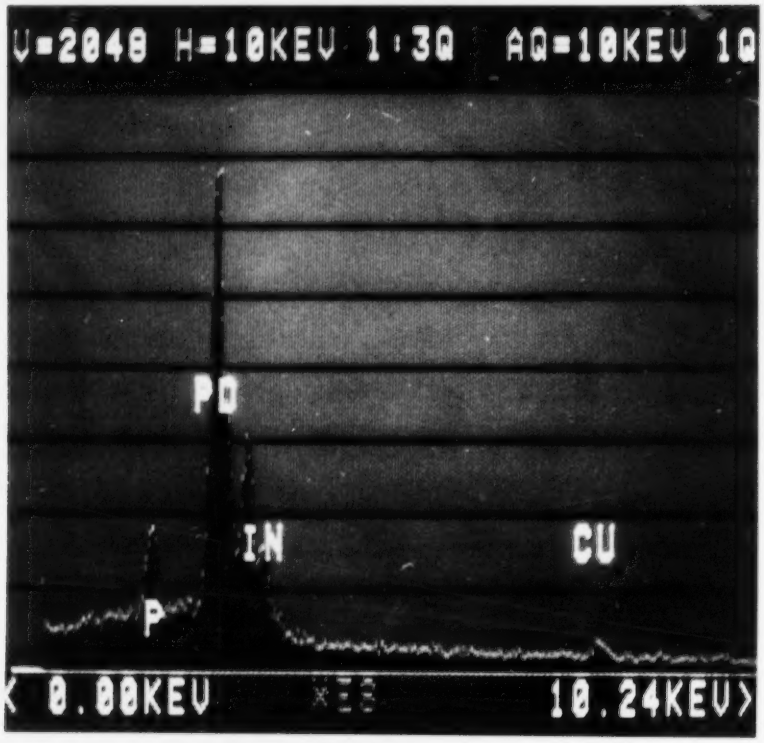

Fig. 6-1 X-ray spectrum from the amorphous Pd-In-P layer. This was taken from a plan view specimen, providing an average composition through the thickness of the layer.

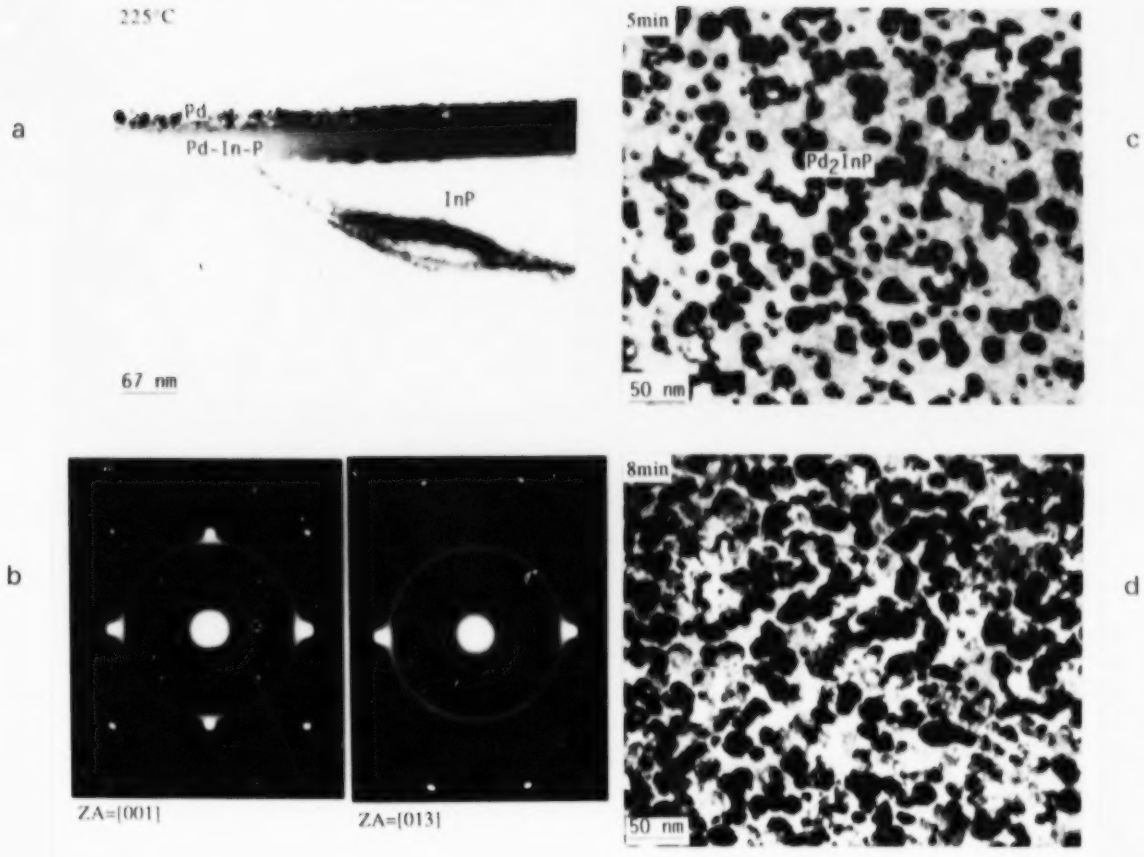

Fig. 6-2 Bright field micrographs and SAD patterns from specimens annealed at 225°C: a) cross-section view, b) [001] and [013] oriented SAD patterns of Pd_2InP, c) and d) plan views.

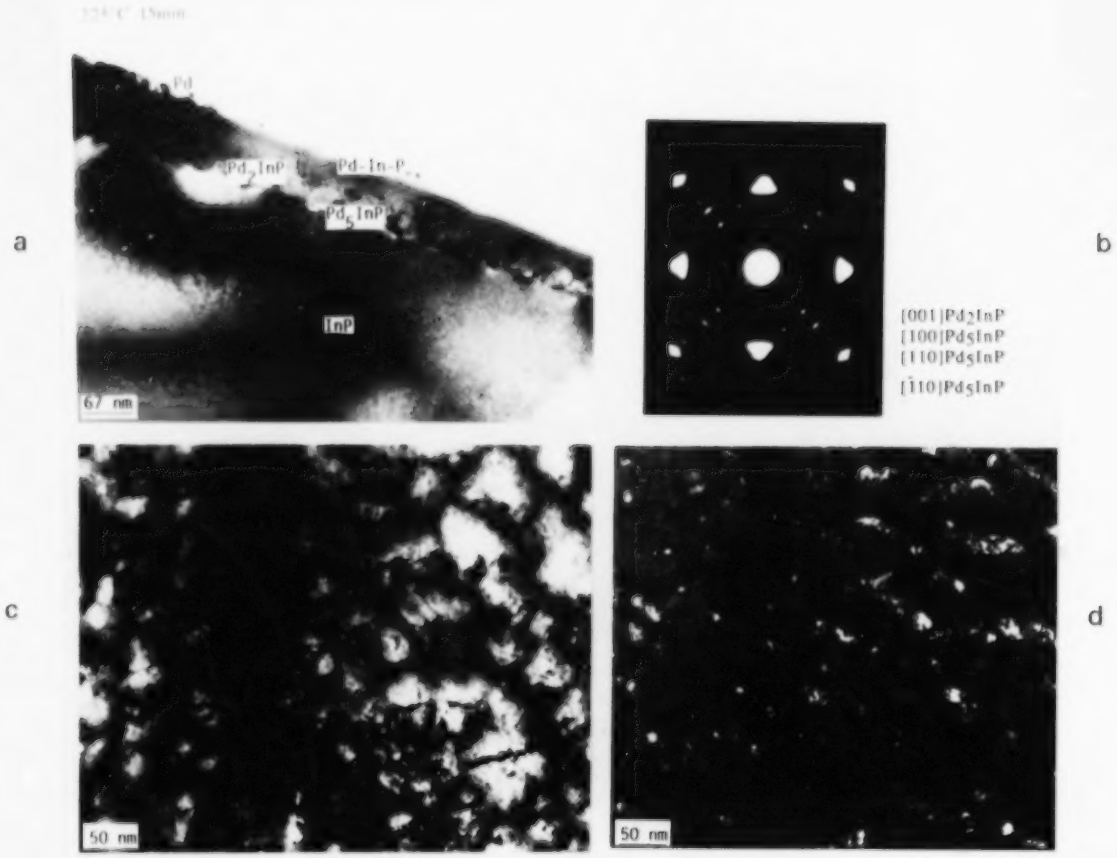

Fig. 6-3 a) Bright field image of a cross-section, b) SAD pattern of Pd_2InP and Pd_5InP, c) Bright field and d) dark field images of a plan view from the sample annealed for 15 min. at 225°C. The Pd_5InP particles show up bright in the dark field image. The dark field image was taken using a (002) reflection from Pd_5InP.

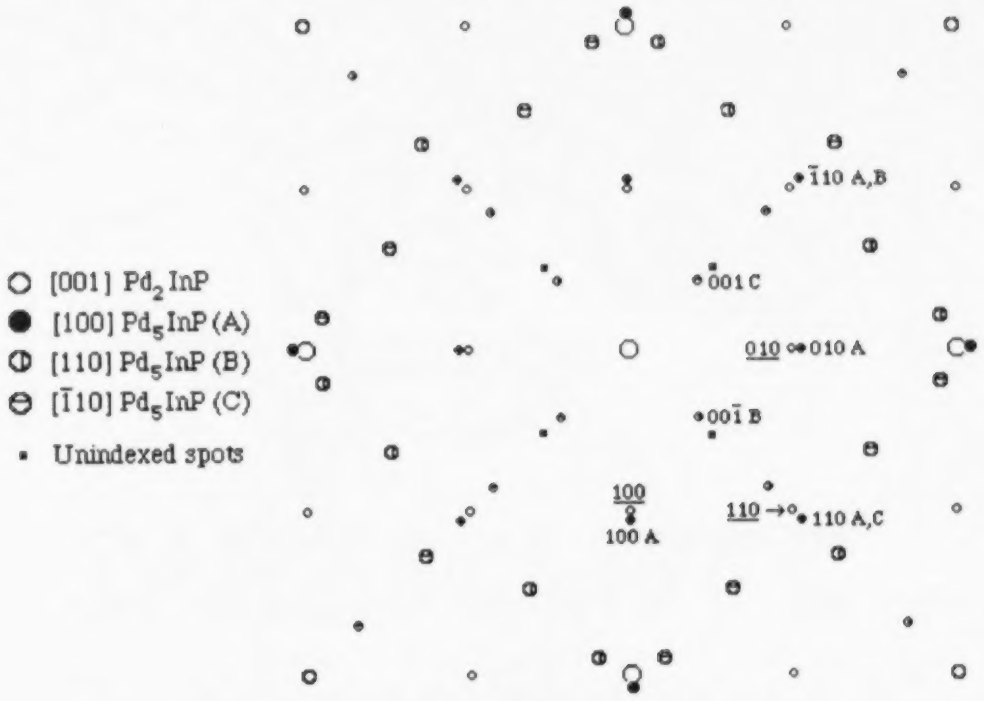

Fig. 6-4 Computed SAD pattern corresponding to Fig. 6-3c. Three orientations of Pd_5InP ([001], [110] and [$\bar{1}$10]) are superimposed on [001] Pd_2InP. The Pd_2InP reflections are underlined.

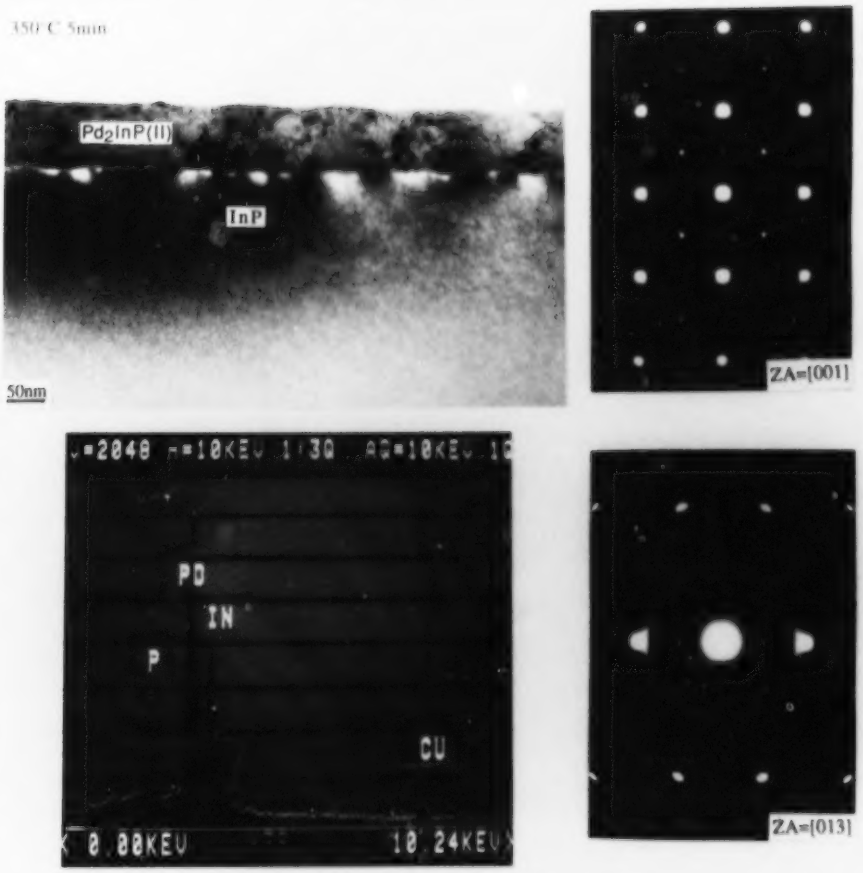

Fig. 6-5 Bright field image of a cross section, SAD patterns of $Pd_2InP(II)$ and x-ray spectrum of the layer shown in the cross section image from the sample annealed at 350°C for 5 min.

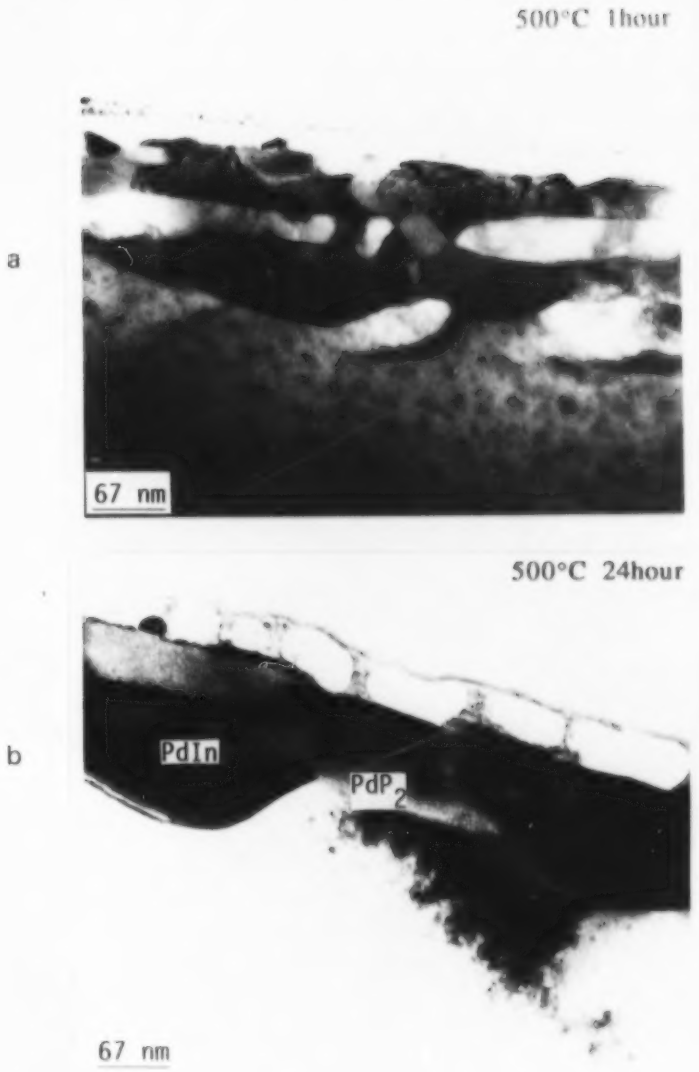

Fig. 6-6 Bright field micrographs (cross sections) from specimens annealed at a) 500°C for 60 min. and b) 500°C for 24 hours. The light contrast regions are PdP_2, while the darker regions are PdIn.

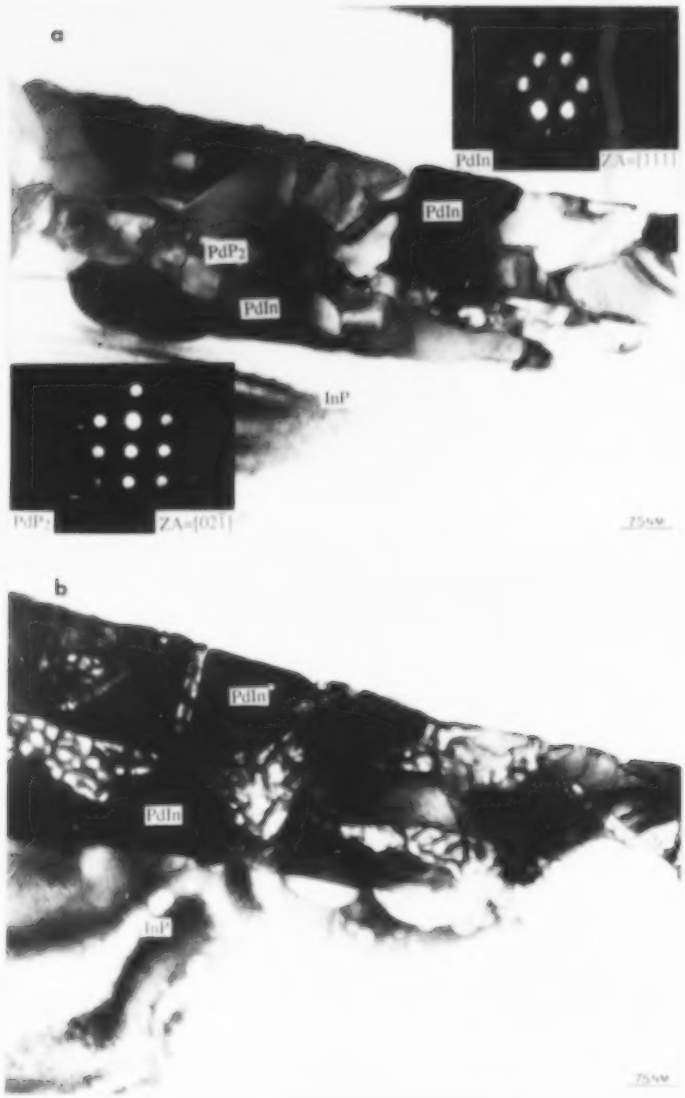

Fig. 6-7 Bright field micrographs (cross section) from identical regions of specimen annealed at 500°C for 5 min. The porous areas in b) correspond to regions of P loss to the atmosphere.

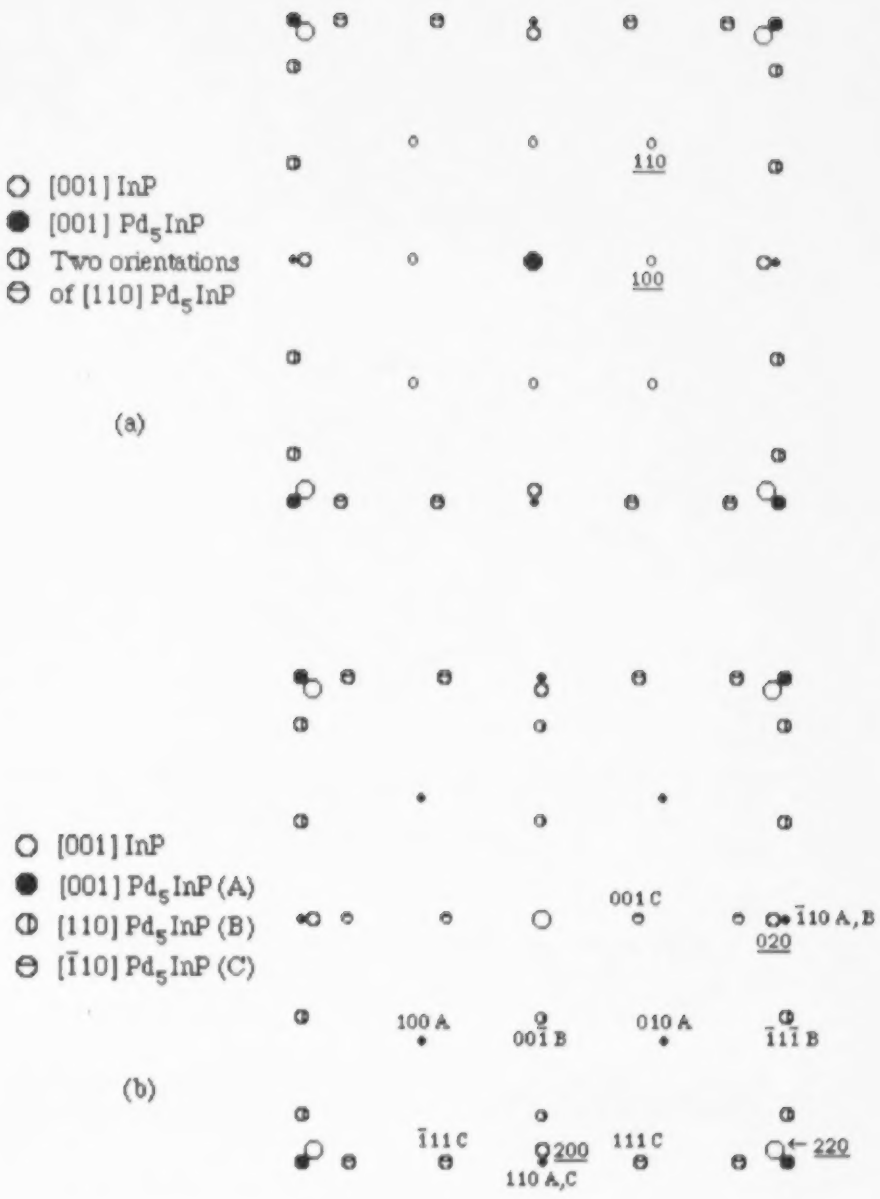

Fig. 6-8 a) Schematic SAD pattern from Ref. 140, showing three Pd_5InP orientations superimposed on [001] InP. Improperly indexed InP reflections are shown. b) Our interpretation of the diffraction pattern in a). Pd_5InP reflections are indexed with letters A, B and C used to distinguish between the three orientations. InP reflections are underlined.

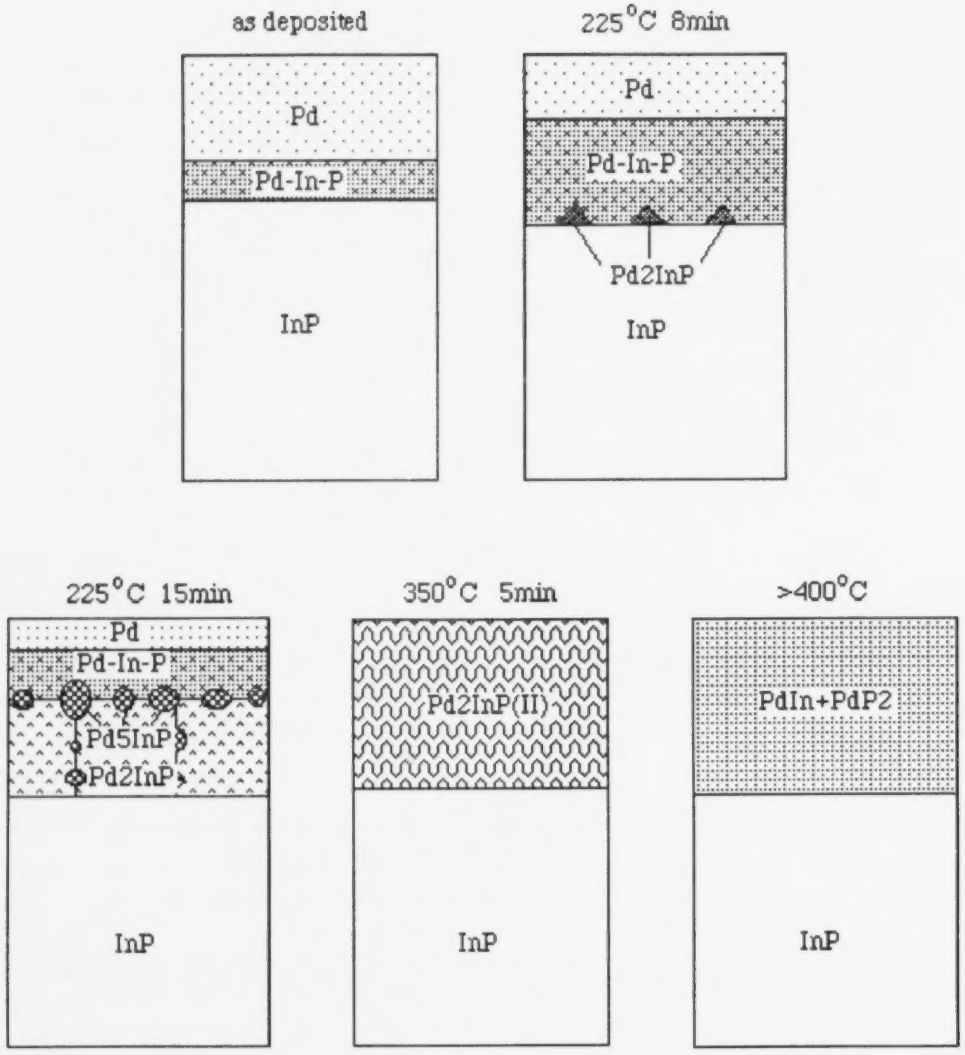

Fig. 6-9 Schematic representation of the reactions of Pd films on InP substrates.

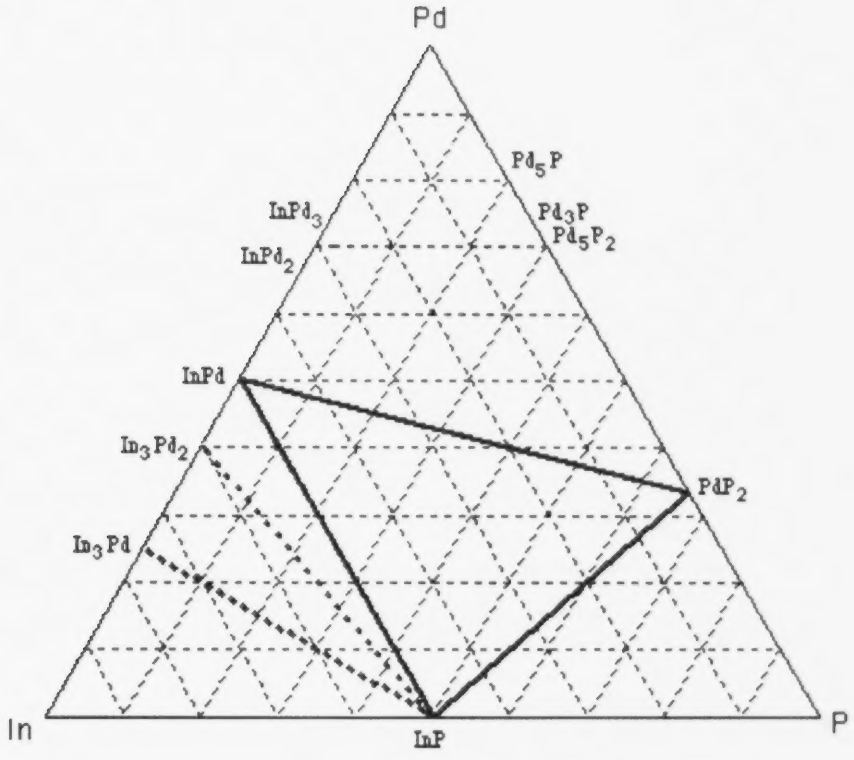

Fig. 6-10 Isothermal section of the Pd-In-P phase diagram, showing the stable tie lines for the Pd-poor portion. The dashed lines are inferred from the experimentally determined solid lines.

Table 6-1 Summary of crystallographic data for ternary and binary phases

Phase	Structure	Lattice parameters (nm)
Pd-In-P	amorphous	
Pd_2InP	cubic ($L1_2$)	a=0.415
Pd_5InP	tetragonal (Pd_5TlAs)	a=0.393, c=0.692
Pd_2InP(II)	cubic	a=0.83
PdIn	cubic (CsCl)	a=0.353
PdP_2	monoclinic	a=0.621, b=0.586, c=0.587, β=111.8°

Chapter 7 Reactions between multilayer metallizations and InP

7.1. Au/Ge/Pd/InP contacts

For the Au/Ge/Pd/InP contact system, the electrical properties and microstructure were studied in detail in the annealing temperature range from 250°C to 450°C for times as long as 320 seconds.

7.1.1. Resistance measurements

Ohmic behavior was obtained after annealing the metallizations at 300°C to 375°C (Fig.7-1). It is evident from Fig. 7-1 that the specific contact resistances of the contacts decreased with increasing annealing times. The resistances dropped dramatically after annealing for short times (<100s). For longer annealing times, the resistance dropped at much slower rates. The best contacts, i.e., those with the lowest resistance values, were the ones annealed at 350 and 375°C. The specific contact resistance r_c reached a minimum of $2.5\times10^{-6}\Omega cm^2$ for an annealing time of 320s at 350°C. There was some scatter in the curves. One source of scatter may be related to the distribution of phases in the metallization. The r_c values for contacts annealed below 300°C and above 400°C were also measured. Since all these contacts exhibited Schottky behavior, the r_c values are not plotted here.

7.1.2. Microstructural evolution

Several observations can be made regarding the as-deposited specimen (Fig. 7-2a). The metallization consisted of several layers, i.e., Au, Ge, Pd, native oxide and amorphous layers. EDX analysis indicated significant interdiffusion between the metal layers. Traces of Ge were detected in both the outer Au layer (Fig. 7-2b) and the inner Pd layer (Fig. 7-2d). Traces of both Au and Pd were found in the Ge layer (Fig. 7-2c). A limited solid phase reaction took place between Pd and the substrate, with Pd penetrating the oxide layer and reacting with underlying InP to form a 15nm thick Pd-In-P ternary amorphous layer. Approximately 5nm of the Pd layer was consumed to form the ternary phase layer. This layer was very similar in composition to the amorphous phase identified in reactions involving a single Pd layer on InP described in Chapter 6.1.

Significant changes in the microstructures of specimens annealed at 250°C are evident in Fig 7-3a. Only three layers existed in the contacts at this point. EDX, SAD, CBED and x-ray diffraction analysis indicated that the outer layer (about 40nm thick) consisted of Ge and two Au-based phases. One was Au-rich, containing In, Ge and Pd. The crystal structure was similar to that of $Au_{10}In_3$, i.e., hexagonal structure with lattice parameters of a=1.05nm and c=0.479nm. The other phase was α-Au with In, Pd and Ge in solution. A bright field image of a plan view specimen from this layer is shown in Fig. 7-3b. Heavily twinned $Au_{10}In_3$ grains (with sizes from 15nm to 75nm) are shown. EDX analysis detected that In was present in the layer, which indicated that the InP substrate decomposition was driven by the strong reaction tendency between In and Au. The middle layer was about 40nm thick. Remnants of the oxide layer are visible throughout the layer (Fig. 7-3a). The layer was identified as PdGe phase (orthorhombic, a=0.578nm, b=0.348nm, c=0.626nm) with Au in solution. The average grain size was 3.5nm as shown in Fig. 7-3c. Adjacent to the InP substrate was a fine grained polycrystalline layer approximately 7nm thick. The bright field image of this thin layer is shown in Fig. 7-3d. Accurate composition analysis of this layer was not possible because of its thin nature, however, the presence of Au, Ge, Pd and P was detected by EDX (Fig. 7-3d). The phase is referred to as Au-Ge-Pd-P in this experiment. Even though the Au-Ge-Pd-P phase appeared to be polycrystalline, SAD patterns were single crystal (Fig. 7-3d), which suggested that the Au-Ge-Pd-P phase was preferentially oriented with respect to the InP substrate. The structure appeared to be an fcc type crystal structure with a=0.41nm. The epitaxial relationship, based on an fcc structure, is given below:

$$[001]\text{Au-Ge-Pd-P} \parallel [001]\text{InP}$$
$$(100)\text{Au-Ge-Pd-P} \parallel (110)\text{InP}$$

The formation of this quaternary phase was driven primarily by the inward diffusion of Au to the InP surface. In the Pd/InP contact system, the amorphous ternary phase (Pd-In-P), which formed during deposition, crystallized and grew epitaxially on InP as described in Chapter 6. This was not the case here, presumably because Au-Ge-Pd-P formation is thermodynamically more favorable than Pd-In-P crystallization.

When annealed between 325°C and 350°C, $Au_{10}In_3$ and PdGe grain growth occurred. The PdGe grain size changed from 50-70nm at 325°C for 5s to 150nm at 350°C for 180s. The two outer layers grew together, forming a single layer (Fig. 7-4a,b), whose

thickness was approximately 75nm. A bright field image of this layer in a plan view specimen, annealed at 350°C for 180s, shows (Fig. 7-5a) that there are two phases in this layer. The grains with twinned features (dark contrast areas) were identified as $Au_{10}In_3$ (Fig. 7-5b) by CBED and EDX, while the other grains (light contrast) were PdGe (Fig. 7-5c). In addition, the epitaxial Au-Ge-Pd-P phase decomposed completely and transformed into a single layer (inner layer in Fig. 7-4a,b) of two phases. This decomposition was driven by the continuous diffusion of Au and Ge from the outer layers to the InP substrate. The two phases in the mixture (Fig. 7-6) are an Au-In phase (dark contrast) and a Ge-P phase (white contrast), as determined by EDX (Fig. 7-6). Because the layer was very thin and the grain sizes of both phases were very small, it was impossible to obtain SAD patterns from this layer or CBED patterns from any single grain. Consequently, the structures of the phases have not been identified at this point. It is believed that the decomposition of the epitaxial Au-Ge-Pd-P phase corresponded to a decrease in contact resistance and subsequent ohmic behavior. No regrowth of the semiconductor (InP) was observed in this study although regrowth of GaAs in similar metallizations to GaAs had been reported in the literature [165,168].

Annealing at higher temperatures (400°C - 450°C) did not cause any further changes in the outer layer, except for changes in the grain sizes and distribution of the two phases (Fig. 7-7a,b). The outer layer was about 80nm thick. During annealing, the grains grew up to 230nm in size for $Au_{10}In_3$ and 160nm for PdGe respectively. Significant changes were detected in the inner layer. As is shown in Fig. 7-8, this layer is continuous and much thicker than in the 325°C to 350°C anneals. CBED analysis indicated that the phase, which appeared as a continuous network, was GeP and the other phase was $Au_{10}In_3$. The Ge-P phase layer became a continuous layer adjacent to the outer layer. The layer was about 20nm to 50nm thick (Fig. 7-7a) by 400°C. With further annealing (450°C), the GeP region increased in volume, and the layer thickness of GeP varied from 25nm to 100nm. Meanwhile, spiking of Au-In phase became more and more prominent with increasing temperature. The $Au_{10}In_3$ grain size changed from 60nm at 400°C to 200nm at 450°C. The spiking and the formation of a continuous GeP network corresponded to an increase in contact resistance and eventual reversion to Schottky behavior. The reason for this will be discussed in Section 7.3.

The microstructural changes which occurred during annealing are depicted in Fig. 7-9 and can be summarized by the following reaction equations:

$$Pd + InP \rightarrow Pd\text{-}In\text{-}P \quad \text{(as deposited)}$$

$$Au + Ge + Pd + Pd\text{-}In\text{-}P + InP \rightarrow PdGe[Au] + Au\text{-}Ge\text{-}Pd\text{-}P + Au_{10}In_3[Ge,Pd] \quad (250\text{-}325°C)$$

$$Au\text{-}Ge\text{-}Pd\text{-}P + InP \rightarrow PdGe + Au_{10}In_3 + GeP \quad (\geq 325°C)$$

The above equations have not been balanced because of the uncertainty in the concentrations of the amorphous Pd-In-P phase and Au-Ge-Pd-P. The overall or net reaction is :

$$10Au + 4Ge + Pd + 3InP \rightarrow Au_{10}In_3 + PdGe + 3GeP$$

Mass balance calculations show that about 35nm-40nm of the InP is consumed and about 25% of the P released during InP decomposition is lost to the atmosphere.

7.2. Pd/Ge/Pd/InP contacts

The microstructural and electrical behavior of Pd/Ge/Pd/InP contacts have been studied in detail. Two types of contacts were studied, i.e., those with 5nm Ge layers and those with 20nm Ge layers.

The contact resistance measurements are listed in Table 7-1. Most contacts exhibited Schottky behavior except those annealed at 425°C for 180s to 360s, or at 400°C for 360s to 720s. The lowest resistance values were $1\times10^{-5}\Omega cm^2$ and $3\times10^{-5}\Omega cm^2$ for the 5nm Ge and 20nm Ge contacts respectively.

Pd/5nm Ge/Pd Contacts

Examination of the as deposited specimen (Fig. 7-10a) revealed the presence of three layers with a total thickness of 50nm. EDX and SAD analysis indicated that reactions between Ge and Pd and Pd and InP occurred during deposition. An amorphous layer (15nm thick) of Pd-In-P was visible, with the same composition as the amorphous layers in both the Pd/InP and the Au/Ge/Pd/InP contacts. A second layer (approximately 10nm thick), composed of both Pd and Ge, was detected by EDX (Fig. 7-10c). A bright field

image of this layer is shown in Fig. 7-10c. The crystalline grains do not show up well due to the presence of oxide and the amorphous layer. This layer was identified as Pd_2Ge from an SAD pattern (Fig. 7-10c) despite the presence of a diffuse ring from the underlying amorphous layer. An oxide layer was present throughout this layer; it was at the original interface of Ge/Pd. The approximately 25nm thick outer layer was the originally deposited Pd layer. A bright field image of this layer from a plan view specimen (Fig. 7-10b) shows a Pd grain size ranging from 10nm to 40nm. No trace of Ge was detected by EDX in this layer (Fig. 7-10b).

On annealing at 250°C, the Pd-In-P amorphous layer grew until it was approximate 35nm thick (Fig. 7-11). The first signs of crystallinity were detected in the specimens annealed for 10s. A series of micrographs and SAD patterns of this layer obtained from plan view specimens annealed for 10s, 20s and 40s are shown in Fig. 7-12. The reaction products and reaction sequence for the crystallization process were the same as those observed in single Pd films on InP, except for the grain size. The Pd_2InP islands nucleated first (Fig. 7-12a) at the amorphous/InP interface and grew with annealing time (Fig. 6-12b). Pd_5InP nucleated at the Pd_2InP grain boundaries (Fig. 7-12c). The epitaxial growth relationships between Pd_2InP and InP and that between Pd_5InP and Pd_2InP were also the same as those described in Pd/InP system (Fig. 7-12). The grain sizes of the Pd_2InP and the boundary structure were smaller than those observed in the Pd/InP contact system, because the annealing conditions were different in the two systems. The heating rate was faster in the Pd/Ge/Pd/InP system. The middle Pd_2Ge layer maintained the same thickness and grain size. The outer Pd layer became thinner, about 15-20nm thick. Some of the Pd diffused through the Pd_2Ge layer to enter the Pd-In-P amorphous layer. The contact structure annealed at 250°C was $Pd/Pd_2Ge/Pd\text{-}In\text{-}P/Pd_2InP+Pd_5InP/InP$.

Diffusion of Pd from the outer layer, consumed the unreacted Pd. By 350°C, the original deposited Pd layer had disappeared (Fig. 7-13a). The top layer in this figure was a very thin oxide layer containing Pd as the major component and traces of Ge, P and In which could be detected by EDX (Fig. 7-13b). A bright field image of this layer from a plan view specimen is shown in Fig. 7-13b. The underlying layer was a discontinuous Pd_2Ge layer. The thickness of the layer was a bit thinner than that observed in the low-temperature annealed samples (about 8nm thick) but the Pd_2Ge grain size became larger than in the as deposited state. This can be seen in the micrograph of a plan view specimen (Fig. 7-13c). The Pd-In-P amorphous layer had completely transformed at this point, leaving a single crystal layer, i.e., no boundary structure or particles were observed by

TEM. SAD analysis indicated that both Pd_2InP and Pd_5InP had transformed into the Pd_2InP(II) phase. The epitaxial relationship of Pd_2InP(II) with the InP substrate was the same as described in the previous chapter. The thickness of the Pd_2InP(II) single crystal layer was 90-95nm. EDX analysis (Fig. 7-13d,e) showed traces of Ge in the Pd_2InP(II) layer close to the Pd_2Ge/Pd_2InP(II) interface, but no Ge in the area close to the Pd_2InP(II)/InP interface. This means that Ge had started to diffuse into the underlying layer, driven by the following reaction:

$$Pd_2Ge + InP \rightarrow Pd_2InP(II) + [Ge]$$

The contact structure was $Pd_2Ge/Pd2InP(II)[Ge]/InP$ at 350°C.

The first signs of decomposition of Pd_2InP(II) to form PdIn and PdP_2 were detected by SAD analysis at the Pd_2Ge/Pd_2InP(II) interface in the specimen annealed at 400°C. The crystal particles were visible from micrographs of cross section specimens (Fig. 7-14a). An SAD pattern from this area showed a spot pattern overlapping with a ring pattern (Fig. 7-14b). Some of rings were from Pd_2Ge. The other rings were from PdIn and PdP_2. In addition to the diffraction spots of Pd_2InP(II), there were some spots on the PdIn rings beside the Pd_2InP(II) (400) and (440) diffraction spots. These spots were (110) and (200) refections of PdIn, as demonstrated in the computer generated pattern in Fig. 7-14c. This suggested that the PdIn grains had an initial weak preferred orientation with respect to Pd_2InP(II).

$$[001]PdIn \parallel [001]Pd_2InP(II)$$
$$(110)PdIn \parallel (400)Pd_2InP(II)$$

Decomposition of Pd_2InP(II) at the Pd_2Ge/Pd_2InP(II) interface was caused by the continuous outward diffusion of In and P from the InP substrate and the decomposition of Pd_2Ge. The freed Ge entered the underlying Pd_2InP(II) layer. Traces of Ge were also detected by EDX in the Pd_2InP(II) layer close to the Pd_2InP(II)/InP interface. In the Pd_2InP(II) layer close to InP substrate, SAD analysis showed some new features in the diffraction pattern of the Pd_2InP(II). Satellite spots along <110> directions around the principal reflections and streaking along <110> directions are visible in four SAD patterns from different zone axes (Fig. 7-14d). According to previous investigations [200,201], the satellite spots and streaking are characteristic of microstructural defects, such as microtwins

or tweed structure. Therefore, it appears that additional micro-defects had been created in the single crystal Pd_2InP(II) layer during processing.

Significant microstructural changes occurred after annealing at 425°C, as shown in Fig. 7-15. Signs of decomposition of Pd_2InP(II) were detected not only at the Pd_2Ge/Pd_2InP(II) interface, but also within the Pd_2InP(II) layer and at the Pd_2InP(II)/InP substrate interface. The contacts started showing ohmic character at 425°C (180s), with a specific contact resistance of $1\times10^{-5}\ \Omega cm^2$. It is believed that the decomposition of Pd_2InP(II) at the Pd_2InP(II)/InP interface to form PdIn and PdP_2 is responsible for the onset of ohmic behavior, which will be discussed later. From the image of the cross section specimen (Fig.7-15a) annealed for 90 min, it can be seen that the outer layer is uniform and contains three phases, i.e., Pd_2Ge, PdIn and PdP_2. Both the outer layer's thickness and the grain sizes of these phases were larger than those in lower temperature annealed specimens. The total contact thickness at this point was still 75nm, the same as that at 400°C for 180s. By 425°C for 120 min, there was still some undecomposed Pd_2InP(II) (Fig. 7-15b) and the contact morphology was no longer uniform. Some areas of the contact consisted of PdIn, PdP_2 and Pd_2Ge, but other areas still consisted of Pd_2InP(II) and Pd_2Ge phases. The Pd_2InP(II) was fully decomposed after annealing at 425°C for 180 min, with the contact consisting of only Pd_2Ge, PdIn and PdP_2. The grain sizes of PdIn, PdP_2 and Pd_2Ge were much larger than those obtained at lower temperature. Mass balance calculations show that approximate 65nm of InP was consumed at this point. Further annealing to 300 min, resulted in more InP decomposition, which led to more In and P diffusion into the metallization layer, reacting with Pd_2Ge to form PdGe, PdIn and PdP_2 (Fig. 7-16a). Mass balance calculations indicated that another 7.5nm of InP was consumed in these reaction. A bright field image of the outer layer, from a plan view specimen is shown in Fig. 7-16b. The phase shown is PdP_2. Examination, by bright field imaging of a plan view specimen and EDX and CBED analysis (Fig.7-16c), suggested that PdIn, PdP_2 and PdGe were distributed in a random way in the contacts. An image of a plan view specimen from the contact shows that the PdP_2 phase was porous, due to the loss of P when the TEM specimen was exposed to the atmosphere. The SAD pattern shows preferred orientation of PdIn in the contact although the Pd_2InP(II) had completely disappeared (Fig. 7-16d). The contact thickness varied from 120nm to 180nm at this point.

Microstructural changes which occurred during thermal annealing are schematically shown in Fig. 7-17 and can be summarized by the following reaction equations:

$$Ge + 3Pd + InP \rightarrow Pd\text{-}In\text{-}P + Pd_2Ge \qquad \text{(as deposited)}$$

$$xPd + Pd\text{-}In\text{-}P \rightarrow Pd_2InP + Pd_5InP \qquad (250°C)$$

$$2Pd_5InP + 4InP + Pd_2InP + Pd_2Ge \rightarrow 7Pd_2InP(II)[Ge] \qquad (350°C)$$

$$2Pd_2Ge + 3InP + Pd_2InP(II) \rightarrow 4PdIn + 2PdP_2 + 2[Ge] \qquad (400°C)$$

$$3Pd_2InP(II) + InP \rightarrow 4PdIn + 2PdP_2 \qquad (425°C\ <120min.)$$

$$3Pd_2Ge + 2InP \rightarrow 3PdGe + 2PdIn + PdP_2 \qquad (425°C\ >300min.)$$

The above equations have not been balanced because of the uncertainty in the concentration of the amorphous Pd-In-P phase. The overall or net reaction is:

$$4Pd + Ge + 2InP \rightarrow PdGe + 2PdIn + PdP_2.$$

The amount of InP consumed, from mass balance calculations, amounts to 72.5nm.

Pd/20nm Ge/Pd Contacts

For annealing temperatures lower than 425°C, the reactions were similar to those for the 5nm Ge contacts. The only difference in contact morphology was in the thickness of the Pd_2Ge and $Pd_2InP(II)$ layers. Fig. 7-18 show micrographs of cross section specimens annealed at 250°C for 20s and 350°C for 10s. The contact structure at 250°C was 15nm Pd/25nm Pd_2Ge/20nm Pd-In-P/islands of Pd_2InP/InP. The contact structure at 350°C was 50nm Pd_2Ge/35nm $Pd_2InP(II)$/InP. In both cases the Pd_2Ge layers were much thicker and the $Pd_2InP(II)$ or Pd-In-P layers were thinner than those in the 5nm Ge contacts. Moreover, the Pd_2Ge grain size was much larger than in 5nm Ge contacts.

At 425°C, the $Pd_2InP(II)$ phase was less stable than for the 5nm Ge metallizations. The microstructural changes that occurred for various times are shown in Fig. 7-19. Initial signs of decomposition of $Pd_2InP(II)$ were evident for the specimen annealed for 60s. Further decomposition occurred with longer annealing times (Fig. 7-19b). The $Pd_2InP(II)$/InP interface had been broken down by the PdIn and PdP_2 particles. The PdIn phase had the same preferred orientation with respect to $Pd_2InP(II)$ as in the 5nm Ge contacts. $Pd_2InP(II)$ decomposed fully after annealing at 425°C for 180s (Fig. 7-19c). The contact structure consisted of two layers. The outer layer was uniform with a thickness of 35nm. A micrograph and a SAD pattern of a plan view specimen (Fig. 7-20)

suggested that this layer was Pd_2Ge only, which is in contrast to the 5nm Ge metallizations. The average grain size of Pd_2Ge was 75nm. The inner layer was a mixture of PdIn and PdP_2 phase, giving a total contact thickness of 85nm. The contact morphology was fairly uniform, with a specific contact resistance of $3\times10^{-5}\ \Omega cm^2$. The total amount of InP consumed for the above reactions was approximately 21 nm, which was significantly less than the amount of InP consumed for the 5nm Ge contacts.

7.3. Discussion

Since the main objective of this study is to investigate the microstructure and electrical properties of the Au/Ge/Pd/InP and the Pd/Ge/Pd/InP contacts, the discussion in this section will be focused on the following aspects:

1. The processing/microstructure/electrical properties interrelationship with emphasis on reaction processes and the corresponding microstructures that can either result in good ohmic contacts or degrade ohmic behavior.
2. Comparison of Au/Ge/Pd/InP contacts with the Pd/Ge/Pd/InP contacts in terms of contact properties such as contact resistance, uniformity of metallization layers and contact thermal stability, etc.
3. The mechanism of ohmic contact formation based on the experimental results from this study and proposed models from other researchers.

7.3.1. Reactions in the Au/Ge/Pd/InP contact system

From the contact morphology features and electrical properties, the reaction process in the Au/Ge/Pd/InP contact system can be roughly divided into three stages. During the first stage (annealing temperatures <300°C), the contacts were rectifying, and their morphology featured uniform layers. After the first stage, the contact was made up of three layers, Au-In+Ge/PdGe/Au-Ge-Pd-P on InP (Fig. 7-3a). The as deposited structure consisted of four layers, Au/Ge/Pd/Pd-In-P on InP (Fig. 7-2a). It appears that the Ge and Pd layers in the as deposited structure had been replaced by a single layer, i.e., PdGe. The thickness of the PdGe layer, measured from TEM micrographs, was about 40nm. Using chemical stoichiometry and the density of PdGe, the amount of pure Pd and Ge, required to produce 40nm of PdGe through the reaction

$$Pd + Ge \rightarrow PdGe$$

is estimated to be ≈19nm and ≈29nm respectively. In addition, comparison of the thickness and composition of the Pd-In-P amorphous layer in the contact with the results obtained in the Pd/InP system, suggests that approximately 6-7nm Pd had been consumed to form the amorphous layer during the deposition process. As mentioned in the experimental procedure section, the total thickness of Pd in the Au/Ge/Pd/InP contacts was 25nm. Therefore, it can be inferred that virtually all the Pd layer in the as deposited structure was consumed by PdGe formation. The reaction between Pd and Ge to form PdGe is, therefore, thermodynamically or kinetically, more favoured than the formation of Pd-In-P. Therefore, the thickness of the Pd-In-P amorphous layer, which transforms into an epitaxial layer later on, can be controlled by the amount of Ge in the contact scheme. This is important for the manufacture of planar devices. The unreacted Ge diffuses into both the outer and the inner layers of the contacts. Inward diffusion is useful for doping during higher temperature annealing.

From the experimental results, the original Au layer in the as deposited structure had become, after annealing, a two phase mixture consisting of $Au_{10}In_3$ and a Au-In solid solution. It is interesting that the PdGe layer contained less In than the Au+$Au_{10}In_3$ layer. Furthermore, very little In was detected in the Au-Ge-Pd-P layer. Considering that this layer originated from the Pd-In-P layer, it seems that the top layer can extract In from underlying layers. By way of comparison, no In was found, by EDX analysis, in the top (Pd) layer of an annealed Pd/InP contact. Instead, it was found that an In concentration gradient existed within the Pd-In-P amorphous layer in the annealed structure, with the highest In concentration located at the Pd-In-P/InP interface and the lowest at the Pd/Pd-In-P interface. The interaction between Au and In largely enhanced the outward diffusion of In to form a Au-In solid solution and compound mixed layer. Substantial out-diffusion of In might result in the decomposition of a thin InP layer at the interface of metallization/InP substrate and produce more vacancies in the InP substrate. The In site vacancies are very important in terms of doping the surface region of InP. Another significant change, during the first stage of annealing, was that the original Pd-In-P amorphous layer was replaced by an epitaxial Au-Ge-Pd-P layer. This was a strong indication of Au and Ge inward diffusion as well as In outward diffusion.

At stage II (annealing temperatures ranging from 300°C to 375°C), the contacts became ohmic, and their morphology featured two uniform layers, i.e., a $Au_{10}In_3$+PdGe layer and a GeP+$Au_{10}In_3$ layer (Fig. 7-4a,b). It can be inferred that three reactions took

place during stage II annealing. They were $Au_{10}In_3$ formation, which occurred both in the outer layer and at the metallization/InP interface, the decomposition of the epitaxial Au-Ge-Pd-P layer and the formation of GeP at the metallization/InP interface. Among these reactions, the decomposition of the Au-Ge-Pd-P quaternary phase and the reaction between Au and In at the metallization/InP interface are considered to be crucial processes for forming ohmic contacts. This was because the decomposition of the thin Au-Ge-Pd-P layer at the metallization/InP interface released additional Au and Ge. The freed Au reacted further with In forming $Au_{10}In_3$, which created more In site vacancies in the InP lattice. Moreover, some released Ge reacted with P forming GeP and some Ge diffused inward occupying In sites in the InP lattice. Thus a very thin highly doped n^+-InP layer at the metallization/InP interface was formed, which resulted in a tunneling junction and a decrease in the contact resistance, and ultimately an ohmic contact. About 10nm InP substrate was consumed in the reactions at this point.

After the third stage of annealing (beyond 400°C), the contacts became Schottky barriers again, while the contact uniformity was broken down. Although the reaction products of stage III were the same as those of stage II, i.e., GeP and $Au_{10}In_3$, the phase distribution and amounts were different. At stage III, with more Ge diffusing from the outer layer to the metallization/InP interface, GeP grew forming a 20nm thick, continuous layer at 400°C. By 450°C, the average thickness of this layer reached about 50nm. In addition to Ge, Au diffused through the GeP layer, and reacted with In to form additional $Au_{10}In_3$. Spiking of isolated $Au_{10}In_3$ into the InP substrate occurred, breaking down the uniformity of the contact. With increasing annealing temperature or annealing time, the grains became bigger resulting in rougher contact morphology. For instance, the largest $Au_{10}In_3$ grain identified was 30nm in the specimen annealed at 400°C, while at 450°C, the largest one reached 200nm (Fig. 7-7a,b). As a result, the metallization/InP interface was rather rough at 450°C. Both the significant growth of GeP and the spiking of $Au_{10}In_3$ into the InP substrate were undesirable. It is believed that the undesirable growth and spiking were responsible for reversion to Schottky behavior after stage III annealing, because these reactions could consume the very thin n^+-InP layer doped with Ge at the metallization/InP interface and destroy the tunneling junction. About 25-30nm InP was consumed at this stage. In addition, spiking of $Au_{10}In_3$ in the InP substrate destroyed the uniformity of the contact, likely resulting in non-uniform resistance values. From this point of view, significant GeP growth and $Au_{10}In_3$ spiking were considered to be the results of overreaction and should be avoided by controlling the annealing to temperatures less than 375°C in order to obtain good ohmic contacts in the Au/Ge/Pd/InP system.

7.3.2. Reactions in the Pd/Ge/Pd/InP contact system

As with the Au/Ge/Pd/InP contact system, the reaction processes in the Pd/Ge/Pd/InP system can be divided into three stages.

Before the contacts became ohmic (<425°C), Ge and Pd reacted together to form Pd_2Ge. Based on experimental results, this reaction started during metallization deposition and continued until all free Ge was consumed in the system. In this experiment, changing the ratio of Ge to Pd in the contact scheme did not affect the reaction product, i.e., Pd_2Ge, but the amount and grain size of Pd_2Ge was affected. The higher the Ge/Pd ratio, the thicker the Pd_2Ge layer and the larger the Pd_2Ge grain size. In the Au/Ge/Pd/InP system investigated here and the Ge/Pd/InP and the Si/Pd/Ge/Pd/InP systems investigated by Schware et al [190], the reaction products between Ge and Pd were PdGe. This was also true for Pd/Ge/GaAs [164,168,175]. The difference between those results and the results from this experiment might arise from the ratio of Ge/Pd. The ratio range in this experiment was 0.14 to 0.57 (estimated from the thickness of Ge and Pd layers), whereas the ratio of Ge to Pd used in the other investigations [164,168,175,190] changed from 2 to 2.6 (layer thickness ratio). It seems that PdGe formation is preferred if the Ge supply is about twice the Pd supply and that Pd_2Ge formation is preferred if Pd supply is about twice the Ge supply.

Another feature of the Pd_2Ge layer was the presence of a discontinuous oxide layer or a void layer (possibly Kirkendall voids), which can be seen in Fig. 7-10a, Fig. 7-11, and Fig. 7-13a, i.e., the line of tiny white spots in the Pd_2Ge layers. Since the original Ge layer was located between the two Pd layers, the growth of Pd_2Ge occurred along two opposite directions because of interdiffusion of Ge and Pd taking place at both the Pd/Ge and Ge/Pd interfaces, which left the oxide (or void) layer between the interface of the two layers. This layer acted as a marker layer, providing information on elemental migration during annealing. In the specimens with a 5nm thick germanium layer, the marker moved toward the surface during thermal reaction (Fig. 7-10a, Fig. 7-11 and Fig. 7-13a), indicating Pd inward diffusion from the outer layer through the Pd_2Ge layer into the underlying amorphous layer. When all the Pd was consumed, the top layer of the contact was Pd_2Ge and the marker was still within this layer. In the specimens with a 20nm thick original deposited Ge layer, the inner Pd layer had been completely consumed by Pd_2Ge and Pd-In-P formation during deposition. When the samples were annealed, the remaining Ge reacted with the outer Pd layer until all the Pd was consumed. As a result, the Pd_2Ge

layer thickness above the marker was 33-38nm consuming approximately 22-25nm of Pd, whereas the thickness of Pd_2Ge layer below the marker was 3-4nm consuming about 2-3nm of Pd. The marker maintained the same position in the Pd_2Ge layer during the annealing process, which indicated that the outer Pd_2Ge layer was the product of reaction between the outer Pd layer and Ge. After all the Pd was consumed, there was no more Pd inward diffusion. In other words, almost all the Pd outer layer was constrained to form Pd_2Ge during deposition and initial annealing and was restricted to Pd_2Ge during subsequent annealing. Moreover, from the experimental results obtained in the Pd/InP or the Au/Ge/Pd/InP systems, approximately 13-15nm of Pd-In-P formed during deposition, which consumed about 7nm of Pd. Since the same procedure was used for Pd deposition in these systems and the Pd/Ge/Pd/InP system, it is reasonable to say that about 7nm of the inner Pd layer was consumed to form Pd-In-P in the Pd/Ge/Pd/InP system. From the results discussed above, the reaction processes in stage I can summarized in the following paragraph.

During the inner Pd layer deposition, an amorphous Pd-In-P layer forms, which consumes about 7nm of Pd leaving about 3nm unreacted. During Ge deposition, the unreacted Pd is consumed by Pd_2Ge formation at the Ge/Pd interface. The amount of unreacted Ge depends on the thickness of the deposited Ge. Another Pd_2Ge layer nucleates and grows at Pd/Ge interface during the outer Pd layer deposition. In contacts with a 5nm Ge layer, almost all the Ge is already consumed during deposition, so that unreacted Pd in the outer layer can diffuse through the Pd_2Ge layer and react with InP to form more Pd-In-P during annealing. On the other hand, in contacts with a 20nm Ge layer, part of the Ge is left unreacted after deposition. During stage I of annealing, Pd could only react with the unreacted Ge forming Pd_2Ge. No further Pd-In-P amorphous growth took place. Therefore, Pd_2Ge growth competed successfully with Pd-In-P growth for Pd. Since the reaction between Pd and Ge was strongly preferred (another example can been seen in the discussion on the first stage of annealing of Au/Ge/Pd/InP contacts above), Pd_2Ge formation would occur and Pd-In-P growth would stop as long as unreacted Ge and Pd existed. As a result, controlling the thickness of the Ge layer or the Ge concentration in the contact scheme can affect the reaction between Pd and InP in the Pd/Ge/Pd/InP contact system. For a given amount of Pd, the amount of Ge effectively controls the amount of Pd-In-P formed and the amount of InP consumed. For instance, about 65nm of InP was consumed in the reactions between Pd and InP in the samples with 5nm of Ge, but only 21nm of InP was consumed in the samples with 20nm of Ge. The reactions between Pd and InP were similar to those in the Pd/InP system, i.e., the Pd-In-P

amorphous phase formed first during deposition. When the contacts were annealed, Pd-In-P continued growing in the 5nm Ge contacts, whereas no further growth of Pd-In-P occurred in the contacts with the thicker Ge layer. The subsequent reactions (Pd_2InP, Pd_5InP and Pd_2InP(II) formation) in both contacts were similar to the Pd/InP metallizations. Although the thickness of the Pd_2InP(II) layer was different in the contacts due to the different Ge/Pd ratios, the contact morphology were quite smooth in all specimens.

The most obvious difference in the contact microstructure after the second stage (400-425°C), compared to the first stage, was the decomposition of epitaxial Pd_2InP(II)[Ge]. After annealing at 400°C, Pd_2InP(II)[Ge] decomposed into PdIn and PdP_2, which were the same products as obtained in the Pd/InP system. From the micrographs of the specimens (Fig. 7-14a and Fig. 7-19a), some features were noteworthy, i.e., PdIn and PdP_2 were first detected at the Pd_2Ge/Pd_2InP(II)[Ge] interface, and PdIn and PdP_2 formed in different locations. However, in the Pd/InP case, decomposition of Pd_2InP(II) was detected at the Pd_2InP(II)/InP interface, and PdIn and PdP_2 were always side by side (in the same region). Based on these observations, it was inferred that decomposition in the Pd/Ge/Pd/InP contacts was driven by the reaction between In or P and Pd_2Ge. During decomposition of InP, both In and P out-diffused and reached the Pd_2Ge/Pd_2InP(II)[Ge] interface. Since no Pd was available, In and P reacted with Pd_2Ge according to the following formula:

$$Pd_2Ge + In + P \rightarrow PdIn + PdP_2 + [Ge]$$

The reaction products were the PdIn and PdP_2, because Pd_2InP(II)[Ge] was not a thermodynamically stable phase in this temperature range. The diffusion rates of In and P were not identical, so that PdIn and PdP_2 nucleated at different spots. The formation of small PdIn and PdP_2 particles might enhance the decomposition of Pd_2InP(II)[Ge] to PdIn and PdP_2 because no nucleation barrier existed. Therefore, as soon as the small PdIn and PdP_2 particles formed at the Pd_2Ge/Pd_2InP(II)[Ge] interface, the Pd_2InP(II)[Ge] phase around those particles decomposed into PdIn and PdP_2. Meanwhile, Ge released from Pd_2InP(II)[Ge] rapidly diffused into the underlying layer. As Pd_2InP(II)[Ge] decomposition continued, the reaction front approached the InP surface, so that the Ge released from the reactions could diffuse into InP. Consequently, a thin InP layer doped with Ge formed at the metallization/InP interface, which resulted in a decrease in contact resistance, i.e., the contact became ohmic.

Stage III of annealing included reactions that took place after complete $Pd_2InP(II)[Ge]$ decomposition (400°C to 425°C). After $Pd_2InP(II)[Ge]$ decomposed, the contact consisted of Pd_2Ge, PdIn and PdP_2. The reactions in the contact did not stop at this point because the system had not yet reached equilibrium. According to the results reported in Ref. 164, 168, 175 and 190, PdGe not Pd_2Ge is in equilibrium with InP. With longer annealing at 400 to 425°C, Pd_2Ge reacted with In and P forming PdGe, PdIn and PdP_2. This reaction degraded ohmic behavior because it consumed the highly doped InP layer, resulting in an increase in contact resistance. For instance, the specimens with a 5nm original Ge layer were annealed at 425°C for 5 hours and approximately 7.5nm of InP was consumed in the reaction between Pd_2Ge and InP to form PdGe. The contact became rectifying. If more Ge, at least more than the amount of Ge required for PdGe formation, was deposited in the contact metallization, the initial reaction of Ge with Pd would be PdGe rather than Pd_2Ge. The PdGe would be in equilibrium with InP, PdIn and PdP_2 after $Pd_2InP(II)[Ge]$ decomposition and the formation of the heavily doped thin layer of InP. As a result, no additional reaction involving InP would occur, so that the thin InP layer doped with Ge would remain intact and contact reliability would be be improved significantly. The ratio of Ge/Pd in this experiment was not the optimum for fabricating a reliable ohmic contact. More Ge or less Pd should be used in the contacts.

7.3.3. Comparison of Au/Ge/Pd/InP and Pd/Ge/Pd/InP contacts

From the experimental observations of the two contact systems described above, some common characteristics are apparent:

1. Both the Au/Ge/Pd/InP contacts and the Pd/Ge/Pd/InP contacts have strong metal/InP adhesion, because the first reaction in both systems is the formation of Pd-In-P at the metal/InP interface. This indicates that the presence of Pd in the metallization scheme indeed improves the wettability of the InP surface.
2. The contact structures of both systems contain an epitaxial layer (quaternary phase in the Au/Ge/Pd/InP contacts, ternary phase in the Pd/Ge/Pd/InP contacts) after the first stage annealing of each respective system. Neither phase is stable on InP, i.e., they are only transition phases.
3. In both systems, when the epitaxial phases decompose, the contacts become ohmic, although the annealing temperatures required are different (300°C - 375°C for the Au/Ge/Pd/InP contacts, 400°C - 425°C for the Pd/Ge/Pd/InP contacts).

4. The optimum contact structure, i.e., the microstructure corresponding to ohmic behavior, consists of binary compounds only, e.g., PdGe, $Au_{10}In_3$ and GeP in the Au/Ge/Pd/InP contact system and PdIn, PdP_2 and Pd_2Ge in the Pd/Ge/Pd/InP contact system.

There are also differences in terms of the electrical properties and contact morphology characteristics between the two systems. One of the most significant differences involves the specific contact resistances. The minimum contact resistance for the Au/Ge/Pd/InP contacts is $\approx 10^{-6}\ \Omega cm^2$, while a value of $\approx 10^{-5}\ \Omega cm^2$ is obtained for the Pd/Ge/Pd/InP contacts. Thus the Au/Ge/Pd/InP contacts have better ohmic behavior, which is in agreement with the experimental results reported in Ref. 172.

It is known that both Au and Pd can react with In and P forming various binary compounds in the Au/InP system and Pd/InP system respectively. In the Au/Ge/Pd/InP system, however, there is no Au-P compound formation because of competitive growth between various compounds. Similarly, no Pd-P compound is found in this experiment for the Au/Ge/Pd/InP system because Pd is restricted to the PdGe phase formation due to the strongly preferred Pd-Ge reaction. The only phosphide formed during the whole annealing process is GeP. The net reactions between Au, Ge, In and P can be expressed by the following equation:

$$10Au + 3Ge + 3InP \rightarrow Au_{10}In_3 + 3GeP$$

According to this equation, the volume ratio of GeP/$Au_{10}In_3$ would be 0.54 if the reaction process exactly followed the stoichiometry in this equation. In this experiment, the reaction between Au and In starts at low temperatures (<250°C), but the reaction between Ge and P begins at relatively high temperatures (>300°C). From the micrographs of the specimens annealed at 250°C to 375°C (Fig. 7-3a, Fig. 7-4a,b), the amount of GeP is much less than that of $Au_{10}In_3$ in the contacts, which indicates the reaction rate for GeP formation is lower than that for $Au_{10}In_3$ formation when the temperature is lower than 375°C. More In is consumed in the reactions than P. EDX analysis shows that P concentration in the metallizations is very low, so that the ratio of P/In in the InP must be larger than 1 in the area near the metallization/InP interface. In other words, outward diffusion of In from InP leaves a large number of vacancies near the metallization/InP interface, which provides a foundation for the Ge doping process. It should be pointed out that some P is likely lost through sublimation.

In the Pd/Ge/Pd/InP contacts, Pd reacts with both In and P according to the following equation:

$$3Pd + 2InP \rightarrow 2PdIn + PdP_2$$

The volume ratio of PdP_2/PdIn is 0.36 if the amount of In and P, released during decomposition of the Pd-In-P epitaxial layer, is the same and all the released In and P react with Pd according to the above equation. In the Pd/Ge/Pd/InP contact system, the reaction between In and Pd and the reaction between P and Pd take place at the same temperature and the same time. Although the reaction rate is not known, from the micrographs of specimens annealed at 425°C (Fig. 7-15b,c and Fig. 7-16a), the difference between the actual volume ratio of PdP_2/PdIn and the theoretical ratio of PdP_2/PdIn is less than that between the actual ratio of GeP/$Au_{10}In_3$ and the theoretical value of the GeP/$Au_{10}In_3$ ratio. This implies that the number of In site vacancies in the Au/Ge/Pd/InP contacts is higher than in the Pd/Ge/Pd/InP contacts. Therefore, the doping level of Ge in the InP substrates of the Au/Ge/Pd/InP contacts is higher than that in the Pd/Ge/Pd/InP contacts. As a result, tunnelling in the Au/Ge/Pd/InP contacts should be easier than in the Pd/Ge/Pd/InP contacts and, hence, the minimum contact resistance value for the Au/Ge/Pd/InP contacts should be lower than for the Pd/Ge/Pd/InP contacts.

Comparing the two systems, the morphology of the Pd/Ge/Pd/InP contacts is more uniform. Before the epitaxial layers decompose, i.e., during the first stage, the contact systems are uniform and layered (three layers in the Au/Ge/Pd/InP contacts and two layers in the Pd/Ge/Pd/InP contacts). After the second stage (300°C-375°C anneal for the Au/Ge/Pd/InP contacts, 400°C-425°C anneal for the Pd/Ge/Pd/InP contacts), the metallization/InP interfaces in both contact systems become rougher due to decomposition of the epitaxial phase. In the terms of practical applications of the contacts, this nanoscale roughness is tolerable so that this kind of morphology is still considered to be fairly uniform. With further annealing, spiking of $Au_{10}In_3$ into the InP substrates in the Au/Ge/Pd/InP system becomes worse, and the contact morphology is rather rough. In contrast, the morphology of the Pd/Ge/Pd/InP contacts is much better, although the compound grains become bigger in the contacts with the further annealing. This indicates that using Pd, instead of Au, in the ohmic contact metallization scheme can improve the contact morphology.

Another difference between the two systems is the optimum annealing condition for forming ohmic contacts. When the Au/Ge/Pd/InP contacts are annealed from 300°C to 375°C for 5-180s, the contacts are ohmic. The temperature range for the onset of ohmic behavior in the Pd/Ge/Pd/InP contacts is 400°C to 425°C, and the optimum annealing periods depends on the ratio of Ge/Pd in the metallization scheme. If the proper ratio of Ge/Pd is used in the contact metallization scheme, the reliability and thermal stability of the Pd/Ge/Pd/InP ohmic contacts would be better than that of the Au/Ge/Pd/InP ohmic contacts under the same working condition because of the inactivity of Pd.

7.3.4. Mechanism of ohmic contact formation

Ohmic behavior in the AuGePd metallizations and the PdGePd metallizations to n-type InP is attributed to a doping mechanism based on solid state reaction-driven decomposition of intermediate phases that occur at the metal/InP interface, producing a very thin, heavily doped InP layer.

It is known that there are three general principles for forming ohmic contacts, which have been described in Chapter 3. Two of these are possible factors governing the formation of Au/Ge/Pd/InP and Pd/Ge/Pd/InP ohmic contacts. The first one is that the compounds that form at the metal/InP interface during annealing have a work function less than that of the n-InP, so that no energy barrier exists at the metal/InP interface for electron flow. In the Au/Ge/Pd/InP contact system, $Au_{10}In_3$, GeP and PdGe form at the metallization/InP interface. $Au_{10}In_3$ and GeP do not have lower work functions than InP, since both are present after stage II (ohmic behavior) and stage III (Schottky behavior). In the Pd/Ge/Pd/InP contacts, PdIn, PdP_2, Pd_2Ge and PdGe form during thermal reaction. PdIn and PdP_2 are not the compounds responsible for the onset of ohmic behavior in the Pd/Ge/Pd/InP contact system, for the same reasons that $Au_{10}In_3$ and GeP are not. The Pd_2Ge phase is in the outer layer of the contact when the contacts became ohmic, i.e., it is not in direct contact with InP at that point, so that this phase is also ruled out. The PdGe phase only forms in the Pd/Ge/Pd/InP contacts with a 5nm Ge layer, which takes place after the third stage of annealing when the contacts become Schottky barriers again. In addition, there is no PdGe formation in the contacts with a 20nm original deposited Ge layer. Therefore, since PdGe is not responsible for the ohmic behavior in the Pd/Ge/Pd/InP contacts, it is not likely to be responsible for ohmic behavior in Au/Ge/Pd/InP contacts. From the above analysis, it can be concluded that ohmic contact formation in Au/Ge/Pd/InP contacts and Pd/Ge/Pd/InP contacts is not governed by the

formation of zero energy barriers (or lower energy barriers) at the metallization/InP interface.

The other principle for ohmic contact formation is that a shallow InP surface layer, which is much more heavily doped than the rest of the InP substrate, is produced during the annealing process. As a result of the doping, the energy barrier at the metal/InP interface is narrowed, so that electrons can easily tunnel through the barrier without much energy loss. In general, it is considered that the semiconductor doping process is realized by either liquid phase regrowth or solid phase regrowth of the compound semiconductor.

Annealing of metal films on compound semiconductor substrates, at temperatures above or slightly below the Au-Ge eutectic temperature can result in the dissolution of the compound semiconductor and subsequent precipitation or regrowth of a heavily doped or alloyed epitaxial layer. This process is called liquid phase regrowth of compound semiconductor [204,205]. The ohmic properties of eutectic Au-Ge (12.5wt% Ge) based metallizations to n-type GaAs have been attributed to the formation of a Ge-doped GaAs layer by the dissolution and regrowth mechanism. This model fails, however, when it is applied to the Au/Ge/Pd/InP contact system, because no sign of melting or dissolution and regrowth of the constituents has been detected in the ohmic contacts formed during second stage annealing. Even if the Au-Ge metal layers did melt during the annealing, the InP substrates would not dissolve in the Au-Ge eutectic alloy solution, because the first metal layer next to InP substrate in the contacts is Pd rather than Au-Ge. Actually, cross sectional TEM micrographs from this experiment show that the Ge reacts with Pd to form PdGe, and Au reacts with In forming a Au-In solid solution or compound during annealing of the contacts at 250°C. It should be pointed out that this temperature is well below the eutectic point for Au-12.5wt% Ge (361°C). This is a strong indication that the reaction between Ge and Pd as well as that between Au and In are either kinetically or thermodynamically preferred over the formation of a Au-Ge eutectic. Therefore, when the contacts are annealed at 300°C to 375°C, there should not be any InP dissolution and regrowth taking place in the Au/Ge/Pd/InP contact system.

The mechanism for solid phase regrowth of a compound semiconductor is based on the assumptions that reaction-driven decomposition of an intermediate phase takes place at temperatures well below the melting points of the interfacial phases, thereby producing laterally uniform regrowth layers. This type of process can be described as follows [164]: Films of two elements M and M' are deposited sequentially on a compound semiconductor

substrate AB. At low annealing temperatures, the film of metal M adjacent to the substrate reacts with AB to form a ternary phase M_xAB according to:

$$xM + AB \rightarrow M_xAB$$

The second film consists of an element M' that is chosen such that it reacts with M_xAB to form a compound MM'_y that is sufficiently stable so as to drive the reaction

$$(xy)M' + M_xAB \rightarrow AB + xMM'_y$$

to the right. Because of the proximity of the crystalline AB substrate, epitaxial regrowth of AB is likely. Furthermore, regrown AB may be doped or alloyed with M'. This model is usually used to explain the ohmic formation mechanism of Pd-based or Ni-based metallizations to n-GaAs or n-InP substrate systems, because the only metals (M) that are known to react with GaAs and InP at low temperatures (≤200°C) to form M_xAB ternary phases are Ni and Pd.

In the Au/Ge/Pd/InP and the Pd/Ge/Pd/InP contact systems, low temperature formation of the quaternary phase (Au-Ge-Pd-P) and ternary phase (Pd_2InP(II)), does occur in each respective system, as does the decomposition of these phases. The model of solid phase regrowth of a compound semiconductor, however, cannot be applied to these circumstances. According to the model, Pd is supposed to act as the element M, while Ge acts as the element M' in the contacts. But, TEM observations of the Pd/Ge/Pd/InP contacts indicate that the Ge reacts with Pd, rather than with Pd-In-P phase, to form Pd_2Ge during low temperature annealing (stage I). Because of the limited supply of Ge in the metallization scheme, all deposited Ge is consumed by Pd_2Ge formation before the intermediate Pd_2InP(II) phase starts to decompose, so that the contact has a structure of Pd_2Ge/Pd_2InP(II)/InP at this stage. Consequently it is impossible for the following reaction, during further annealing of this contact (stage II), to take place according to the following equation derived from the model:

$$Ge + Pd_2InP(II) \rightarrow Pd_2Ge + InP$$

Actually, the products of the Pd_2InP(II) decomposition, observed in this experiment, are PdIn and PdP_2 that form a mixed layer, replacing the Pd_2InP(II) layer, which is

sandwiched between the Pd_2Ge layer and the InP substrate. From this result, it can be inferred that $Pd_2InP(II)$ decomposition should occur through the following reaction:

$$3Pd_2InP(II) + InP \rightarrow 4PdIn + 2PdP_2$$

During $Pd_2InP(II)$ decomposition, therefore, no precipitation of InP and no regrowth of InP can take place. Instead, more InP is required and consumed to drive the $Pd_2InP(II)$ decomposition reaction. Moreover, of all reactions occurring in the Pd/Ge/Pd/InP contact during annealing, which are described in Section 7.2., not one results in InP precipitation. In addition, if any regrowth had occurred, it could be observed by TEM, because the most prominent feature in the regrowth layer is a high crystalline defect density. In the TEM micrographs obtained from the Pd/Ge/Pd/InP contacts, no such InP region can be found.

In the Au/Ge/Pd/InP contact system, the amount of Ge in the contact metallization scheme is more than the amount required to form PdGe, i.e., the volume ratio of Ge/Pd is close to 2. According to the results from TEM observations, after Ge reacts with Pd to form PdGe during low temperature annealing (stage I), there is still extra Ge in the contacts. Instead of extracting Pd from Pd-In-P phase, most of the extra Ge diffuses and dissolves in the Pd-In-P phase, while inward diffusion of Au and the outward diffusion of In take place, transforming the Pd-In-P amorphous layer into an epitaxial Au-Ge-Pd-P layer. When this epitaxial layer begins decomposing with further annealing (stage II), although Ge and Pd in the epitaxial phase indeed react to form PdGe, it is still impossible for InP to precipitate. This is because the In concentration in the epitaxial layer is close to zero due to the out-diffusion of In at an earlier annealing stage. Moreover, from the experimental results, Au and Ge, released during decomposition of the AuGePdP layer and diffusing from the outer layer, react with In and P to form $Au_{10}In_3$ and GeP respectively. The reactions can be summarized in the following equation:

$$10Au + Ge + Au\text{-}Ge\text{-}Pd\text{-}P + InP \rightarrow Au_{10}In_3 + 3GeP + PdGe,$$

which is not balanced because the composition of Au-Ge-Pd-P is not known. From this equation it is evident that InP is a reactant but not a product in Au-Ge-Pd-P decomposition. Therefore, more InP is required to finish this reaction, which is similar to what happens in the Pd/Ge/Pd/InP system. Again, there is no evidence of InP regrowth in the contact from TEM observations.

From the experimental results, it is believed that the onset of the ohmic behavior in the Au/Ge/Pd/InP contacts and the Pd/Ge/Pd/InP is due to the formation of a shallow surface layer in the InP heavily doped by Ge diffusion. The inward diffusion of Ge to InP is enhanced by epitaxial layer decomposition at the metallization/InP interface. At lower temperatures (<300°C for the Au/Ge/Pd/InP contacts, <400°C for the Pd/Ge/Pd/InP contacts), Ge diffuses into the epitaxial layer. The driving force for Ge inward diffusion in the Au/Ge/Pd/InP contacts arises from the high Ge concentration in the contacts. The Ge in-diffusion in the Pd/Ge/Pd/InP system is initiated by the reaction between Pd_2Ge, In and P which releases Ge atoms. The epitaxial layer in each system acts as a diffusion barrier that prevents Ge from diffusing into InP substrate. As soon as the epitaxial layer decomposes at the interface of metallization/InP, the Ge atoms, released from the epitaxial layer, rapidly diffuse into the underlying InP substrate and take vacant In sites forming a n^+-type doped InP layer. Because of the uniformity of the epitaxial layer, the thickness of the heavily doped layer and the lateral distribution of the dopant are uniform.

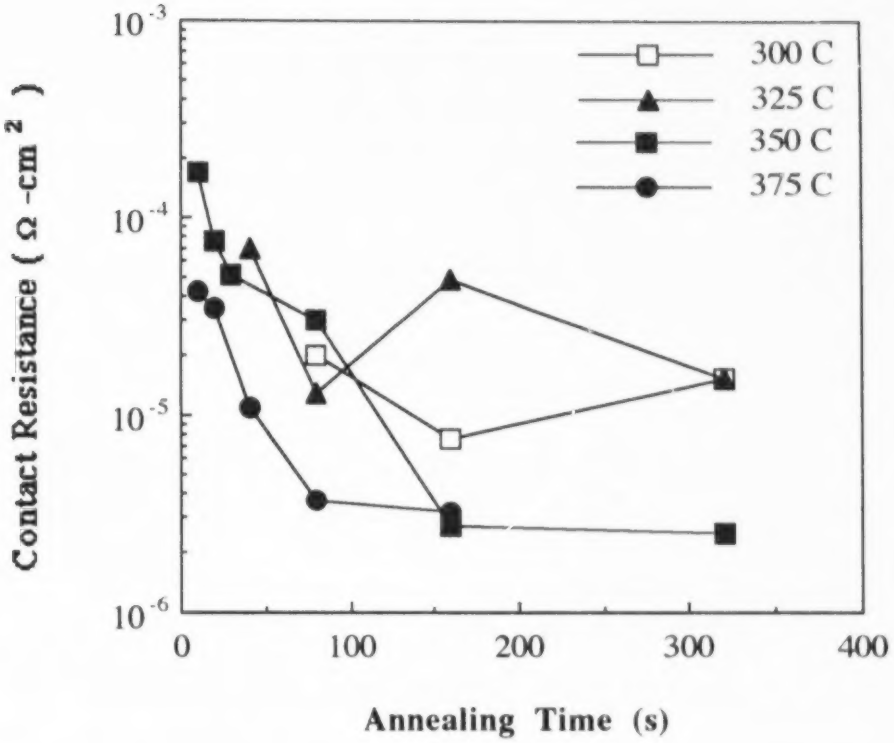

Fig. 7-1 Plot of contact resistance vs annealing time for contacts exhibiting ohmic behavior.

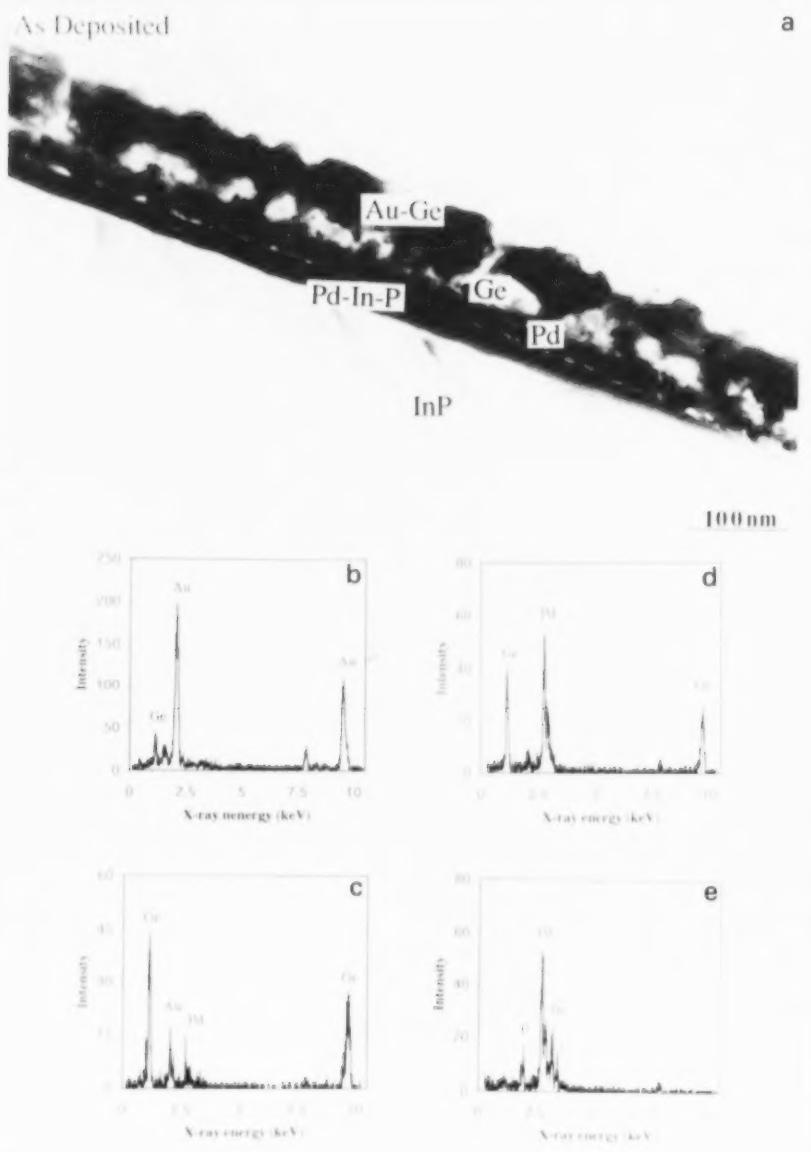

Fig. 7-2 a) Bright field micrograph of a cross section specimen and x-ray spectra from b) the top layer (Au), c) the second layer (Ge), d) the third layer (Pd) and e) the fourth layer (amorphous) of the as deposited sample.

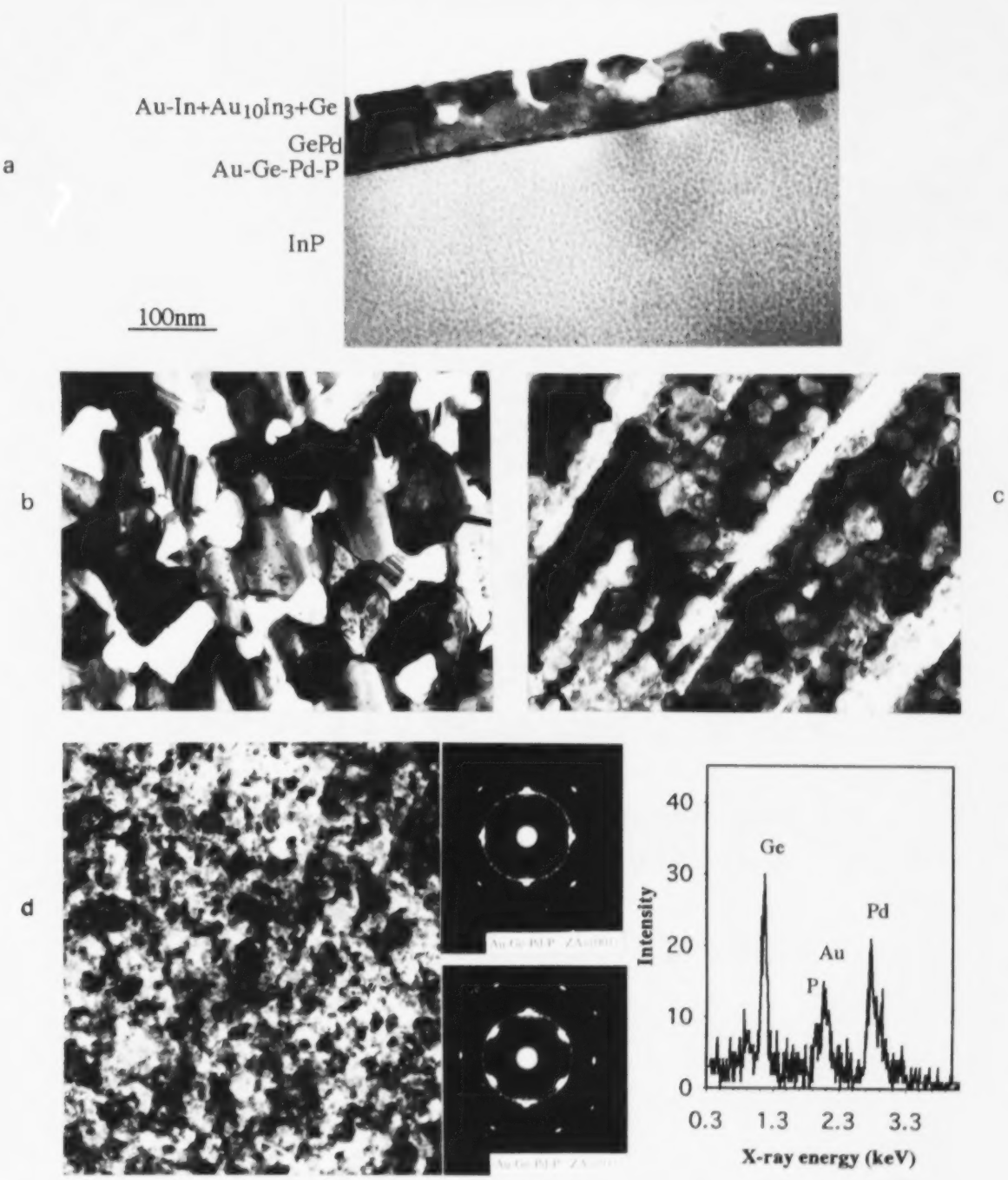

Fig. 7-3 Bright field micrographs of a) a cross section and plan views of b) the outer layer, c) the middle layer and d) the inner layer of the specimen annealed at 250°C for 180s. SAD pattern and x-ray spectrum obtained from the inner layer. The ring pattern in the SAD pattern was from polycrystalline Pd_2Ge.

Fig. 7-4 Bright field micrographs of cross section specimens annealed at a) 325°C for 5s and b) 350°C for 180s.

a

100nm

b

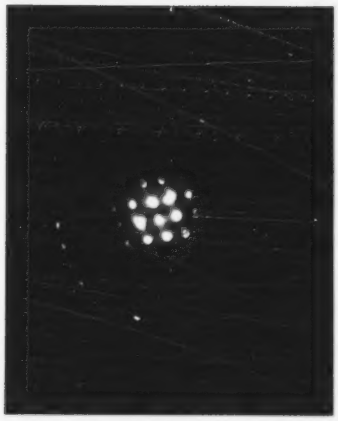

$Au_{10}In_3$ ZA=[71$\bar{8}$3]

c

PdGe ZA=[1$\bar{3}\bar{1}$]

Fig. 7-5 a) Bright field micrograph of a plan view specimen from the outer layer of the specimen annealed at 350°C for 180s. CBED patterns taken from b) dark contrast area and c) white contrast area.

a

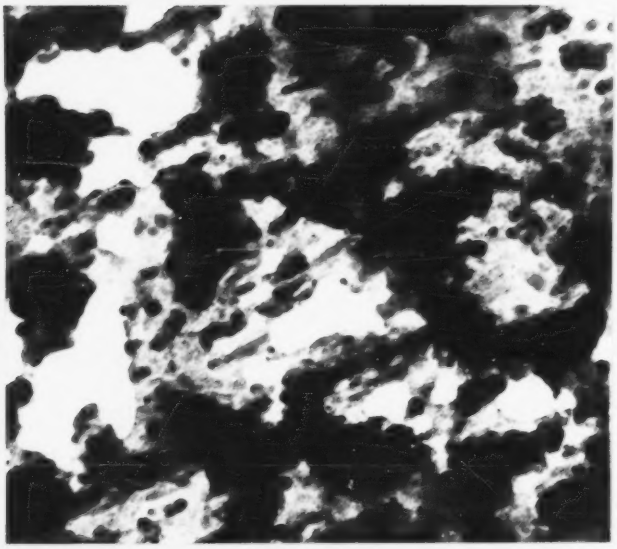

100nm

b

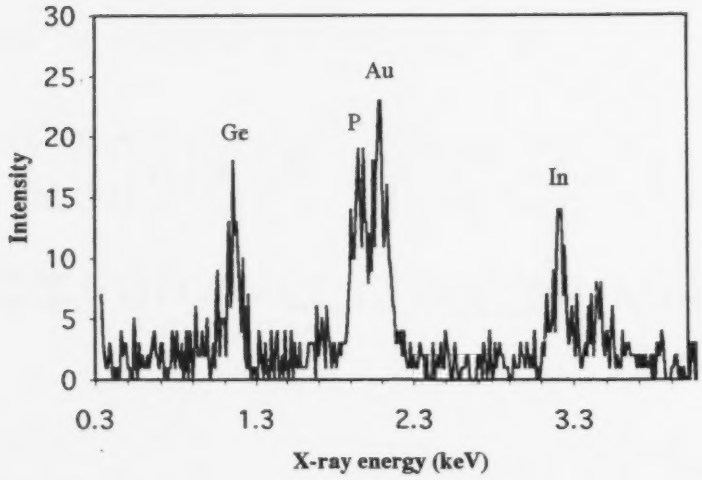

Fig. 7-6 a) Bright field micrograph and b) x-ray spectrum of the layer adjacent to InP substrate, from a plan view specimen annealed at 325°C for 5s.

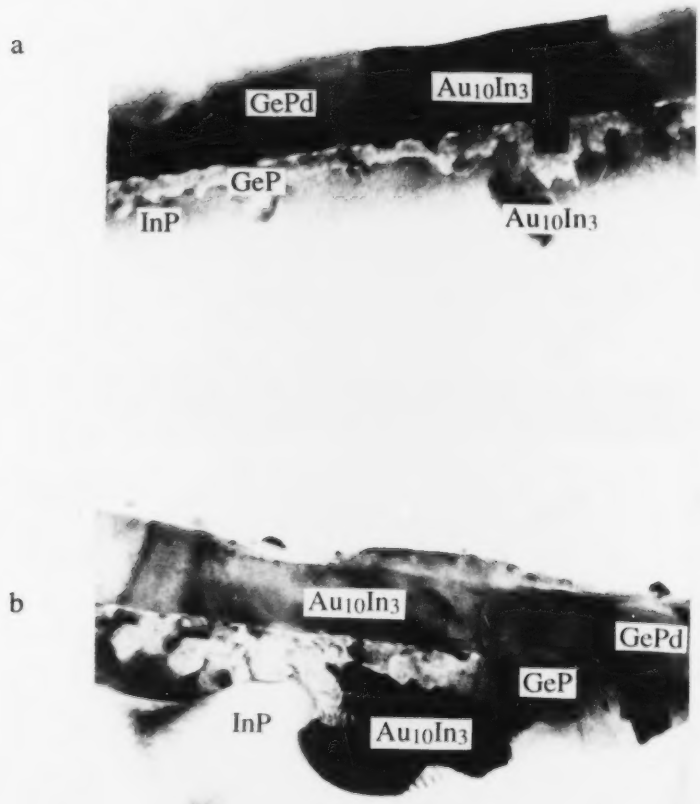

Fig. 7-7 Bright field micrographs of cross section specimens annealed at a) 400°C for 20s and b) 450°C for 180s.

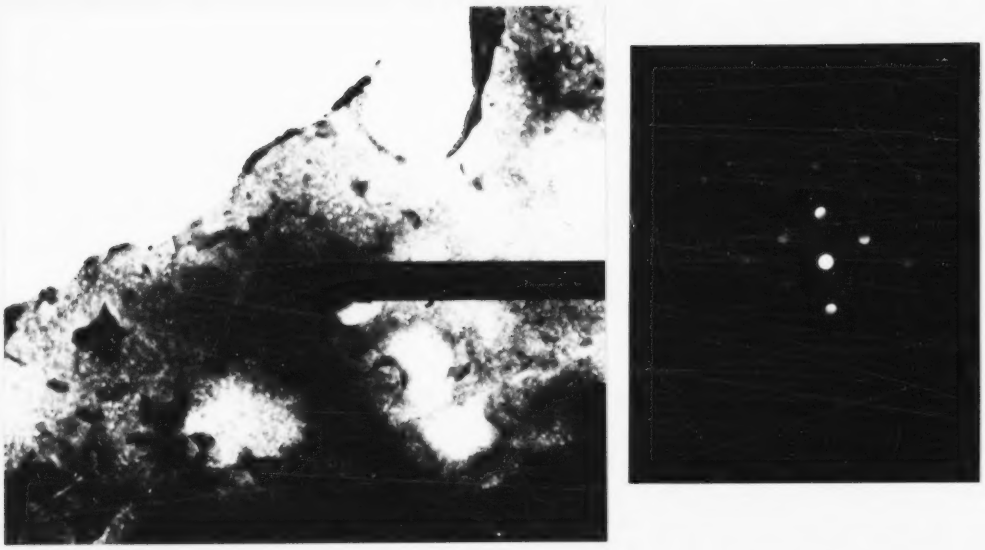

Fig. 7-8 Bright field micrograph of a plan view specimen from the inner layer of specimen annealed at 400°C for 20s. CBED pattern taken from the area indicated.

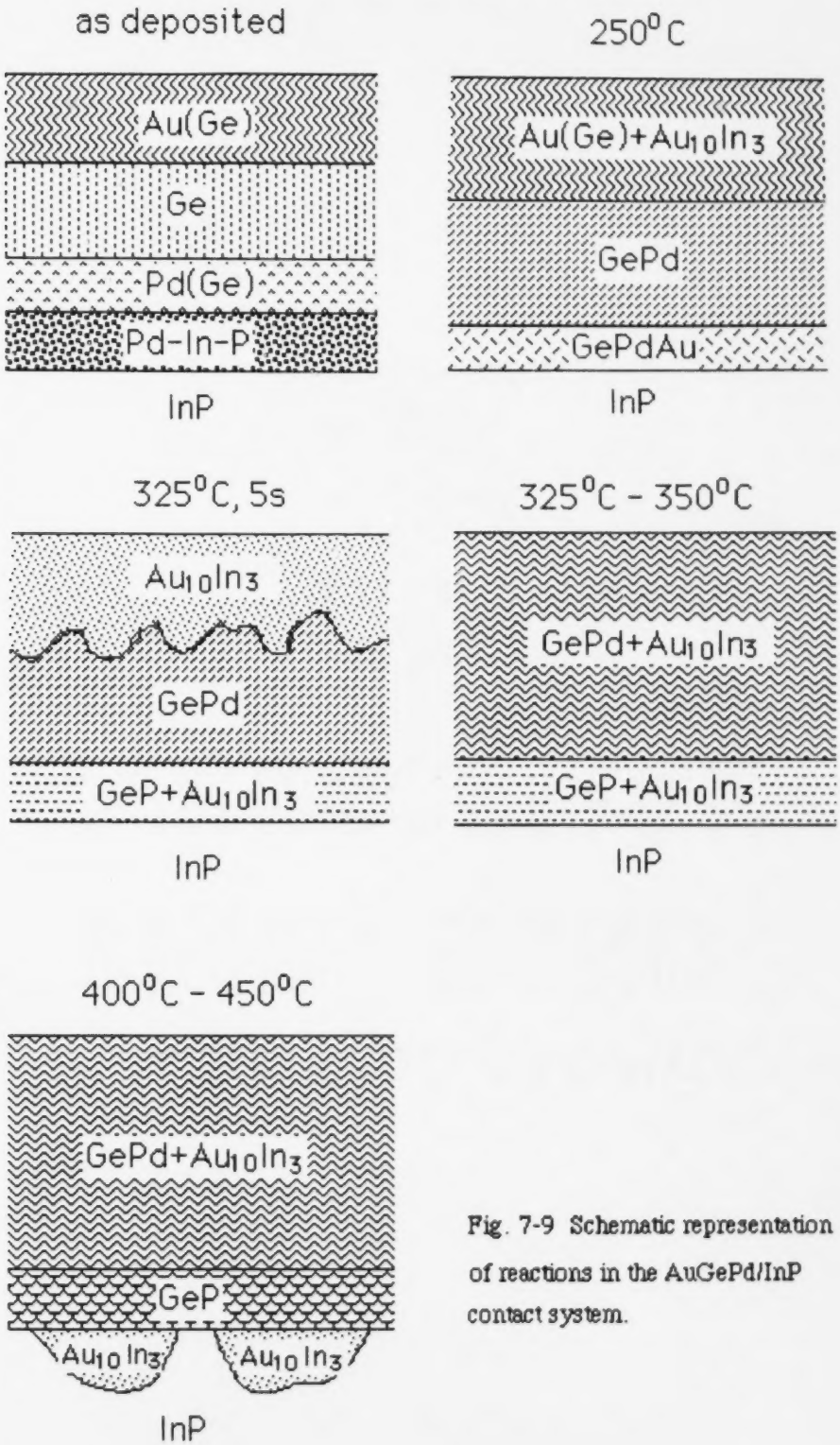

Fig. 7-9 Schematic representation of reactions in the AuGePd/InP contact system.

Fig. 7-10a Bright field micrograph of a cross section specimen from as deposited contact.

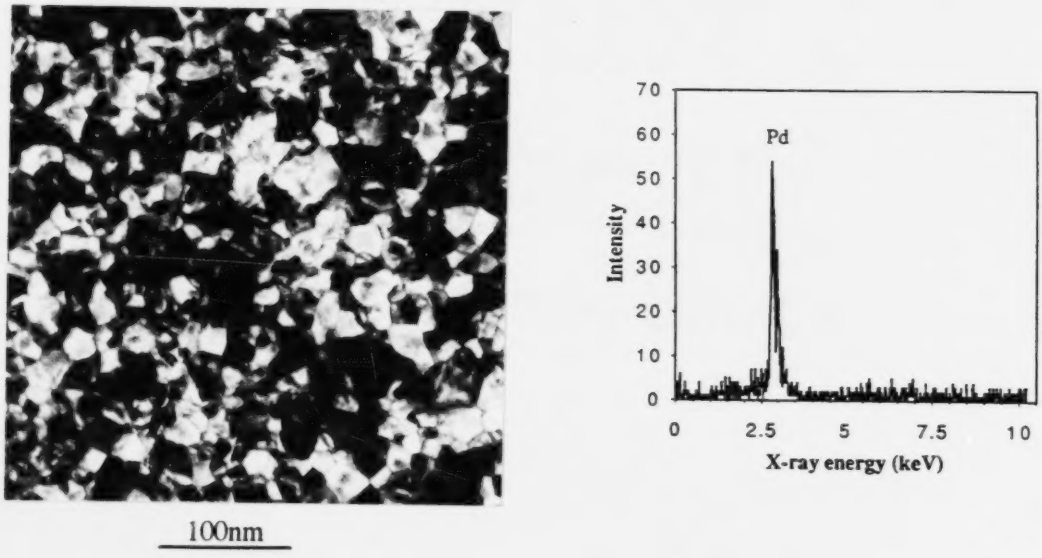

Fig. 7-10b Bright field micrograph of a plan view specimen and x-ray spectrum from the outer layer of as deposited contact.

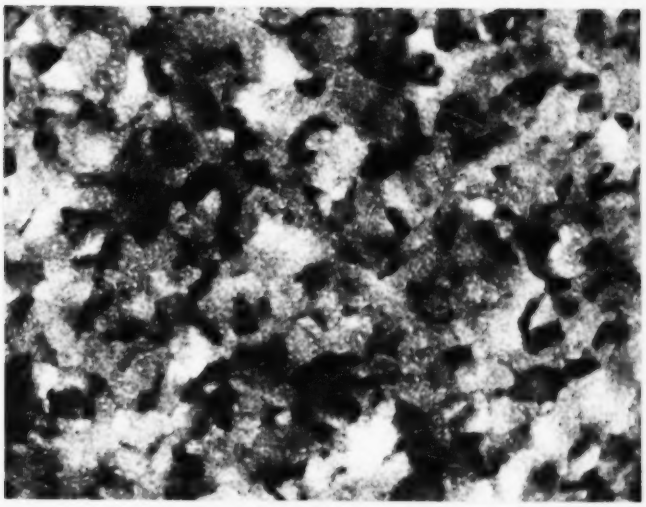

100nm

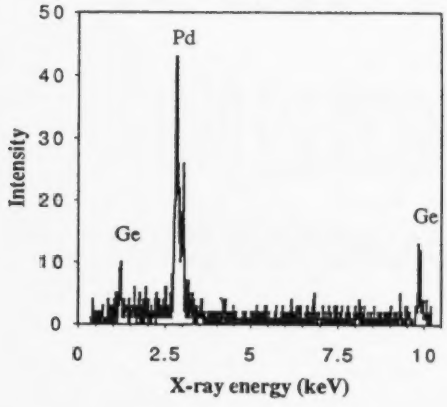

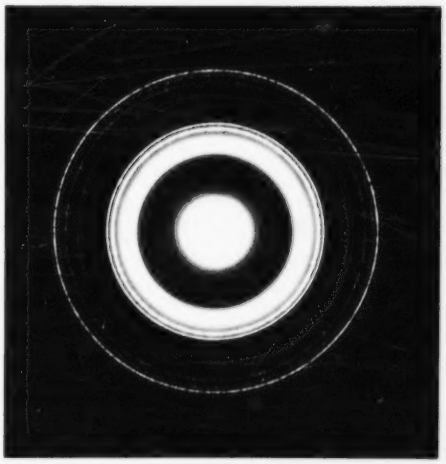

Pd_2Ge

Fig. 7-10c Bright field micrograph of a plan view specimen, x-ray spectrum and SAD pattern of Pd_2Ge obtained from the middle layer of as deposited specimen.

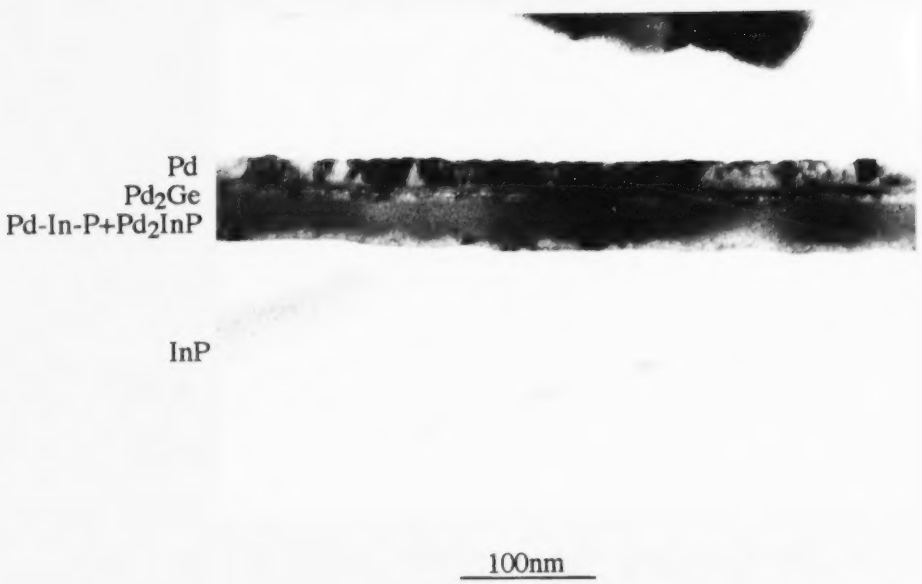

Fig. 7-11 Bright field micrograph of a cross section specimen annealed at 250°C for 10s.

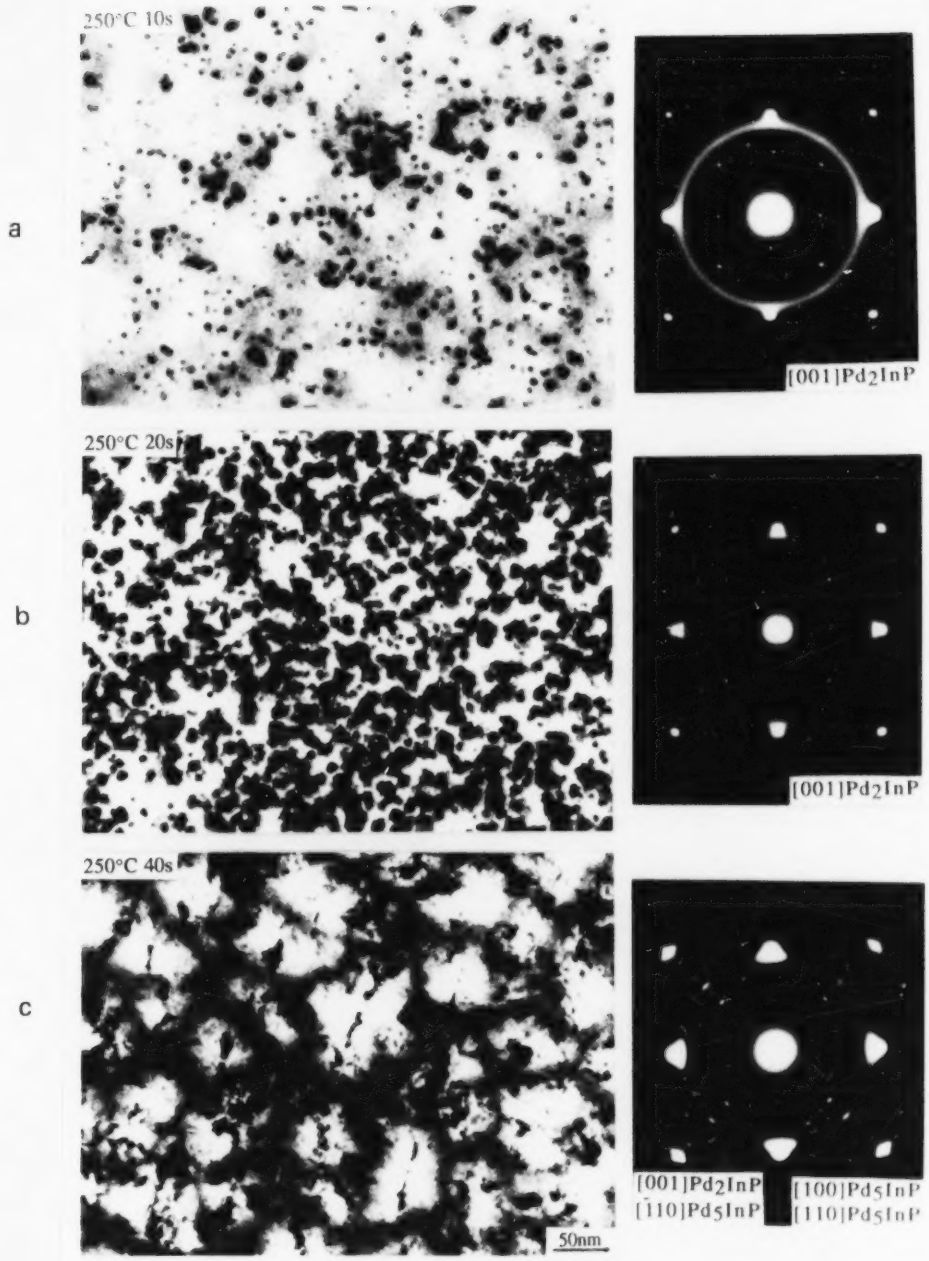

Fig. 7-12 Bright field micrographs and SAD patterns from samples annealed at 250°C for a) 10s, b) 20s and c)40s.

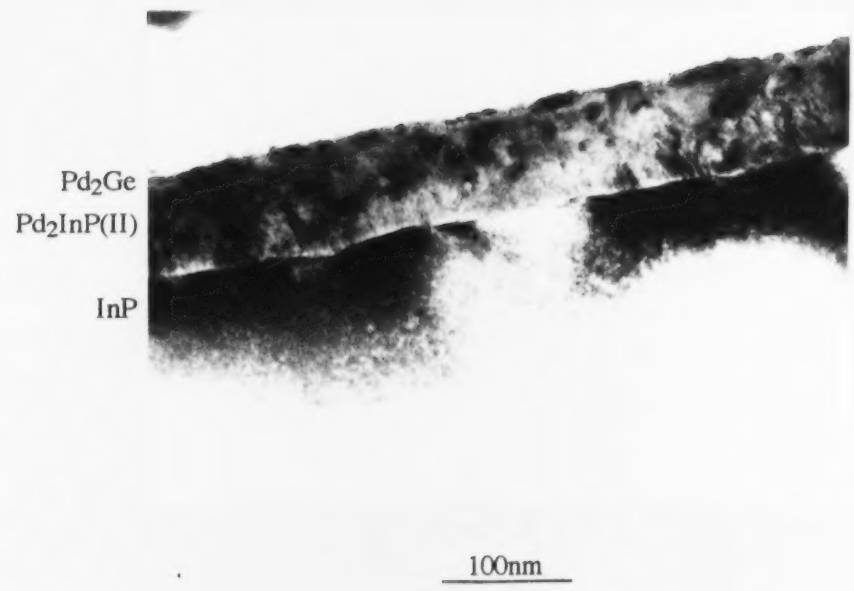

Fig. 7-13a Bright field micrograph of a cross section specimen annealed at 350°C for 20s.

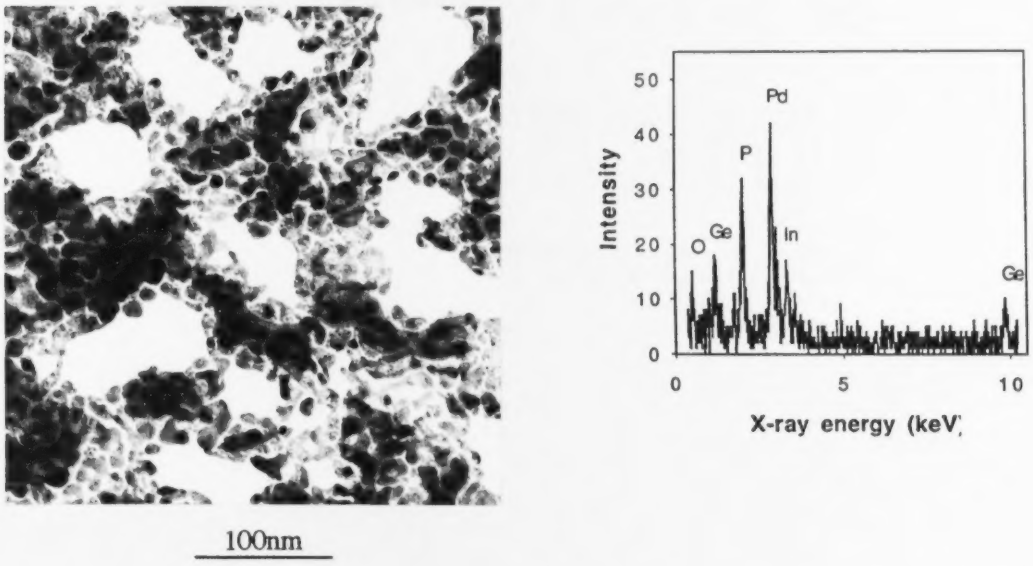

Fig. 7-13b Bright field micrograph of a plan view specimen and x-ray spectrum obtained from the top layer of specimen annealed at 350°C for 120s.

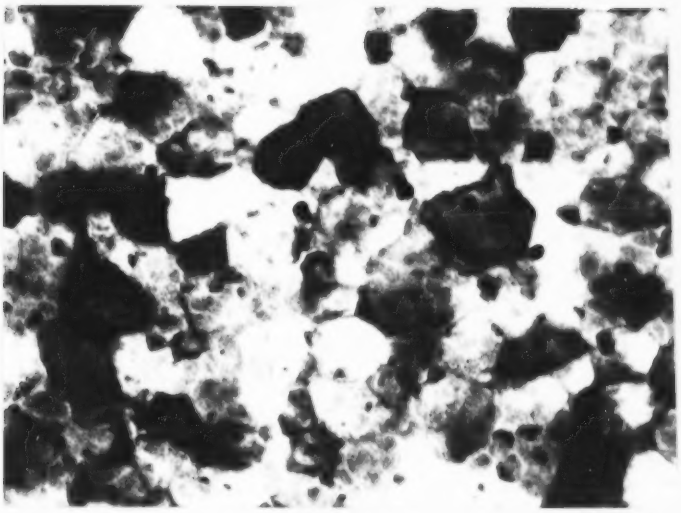

Fig. 7-13c Bright field micrograph of a plan view specimen from t' > second layer of sample annealed at 350°C for 120s.

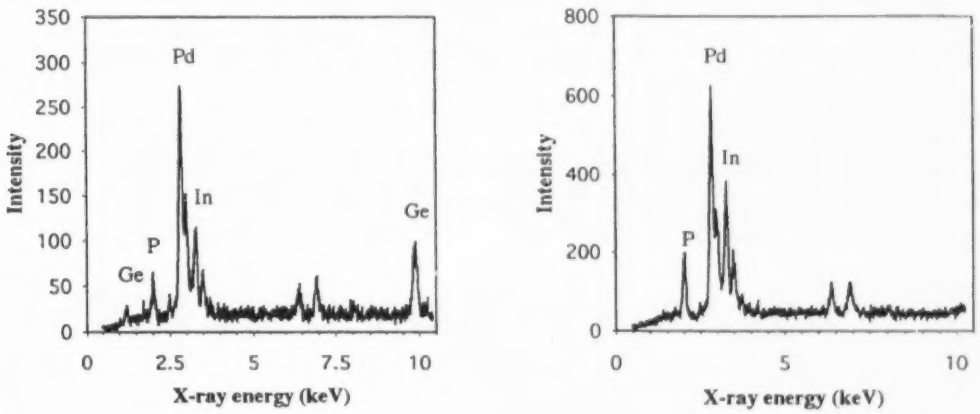

d e

Fig. 7-13 EDX spectra obtained from d) an area close to the $Pd_2Ge/Pd_2InP(II)$ interface and e) an area close to the $Pd_2InP(II)/InP$ interface in the sample annealed at 350°C for 180s.

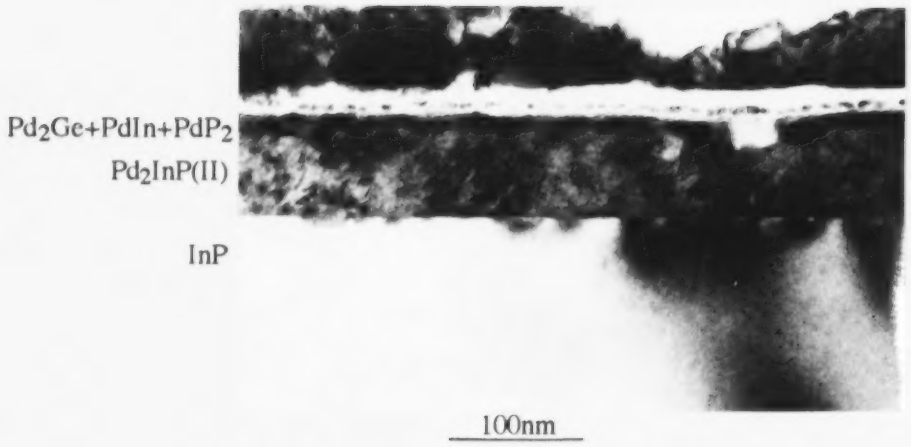

Fig. 7-14a Bright field micrograph of a cross section specimen annealed at 400°C for 180s.

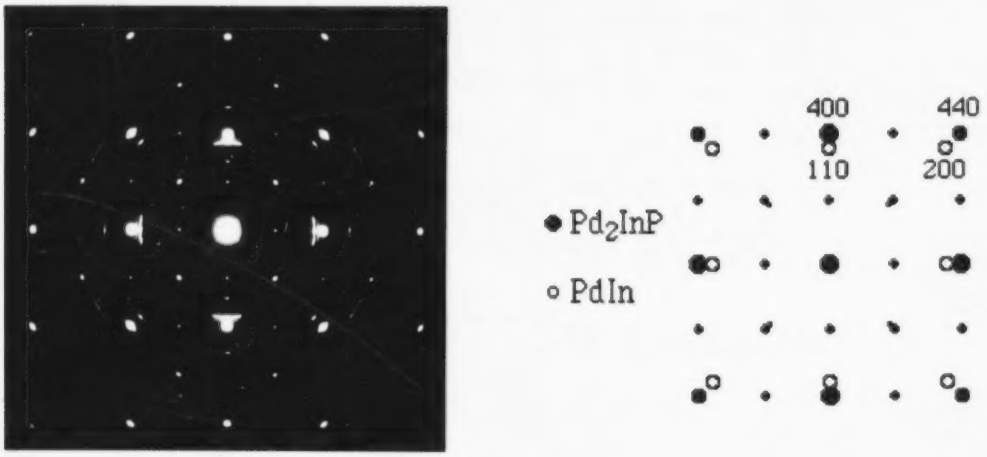

b [001]PdIn [001]$Pd_2InP(II)$ c

Fig. 7-14 b) SAD pattern from a plan view specimen of the first layer in a sample annealed at 400°C for 180s, and c) a computed SAD pattern corresponding to b). [001] orientation of PdIn is superimposed on [001] $Pd_2InP(II)$.

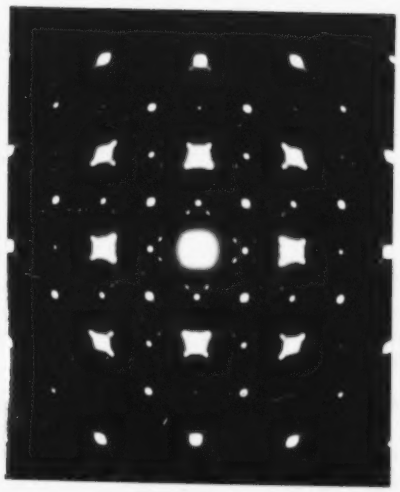

ZA=[001]

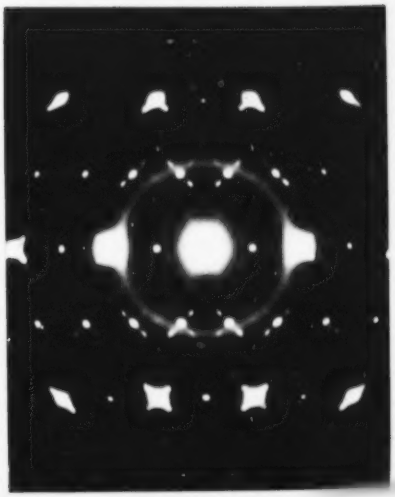

ZA=[013]

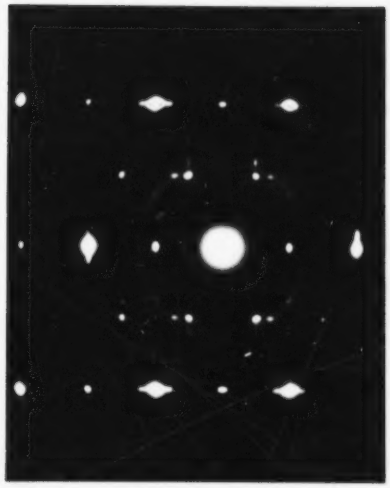

ZA=[114]

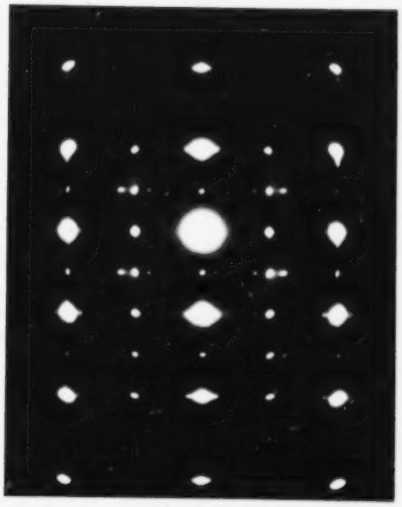

ZA=[112]

Fig. 7-14d SAD patterns of Pd_2InP(II) taken from the inner layer in the sample annealed at 400°C for 180s.

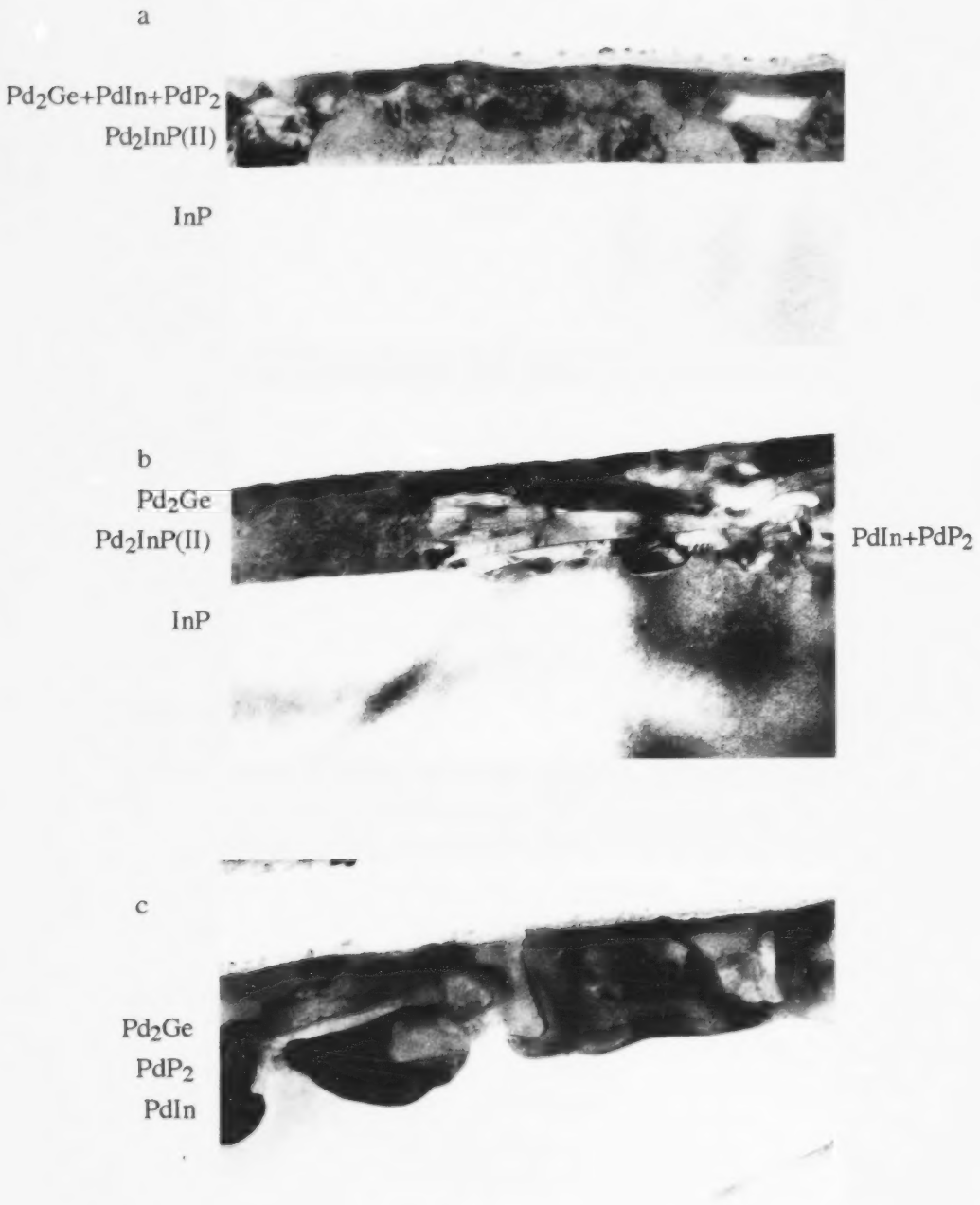

Fig. 7-15 Bright field micrographs of cross section specimens annealed at 425°C for a) 90 min. b) 120 min. and c) 180 min.

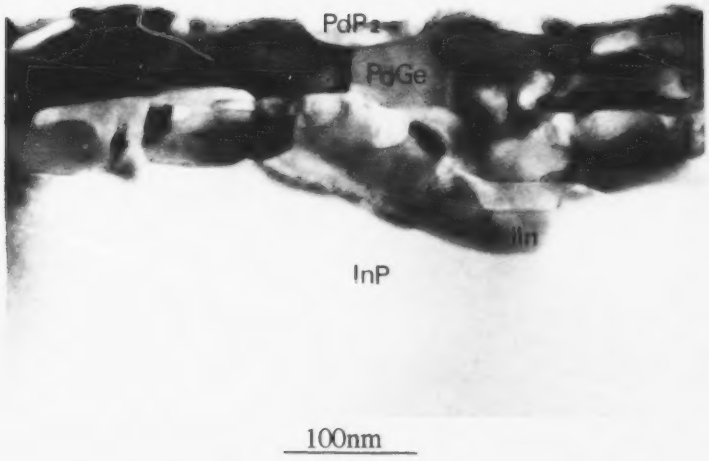

Fig. 7-16a Bright field micrograph of a cross section specimen annealed at 425°C for 5 hours.

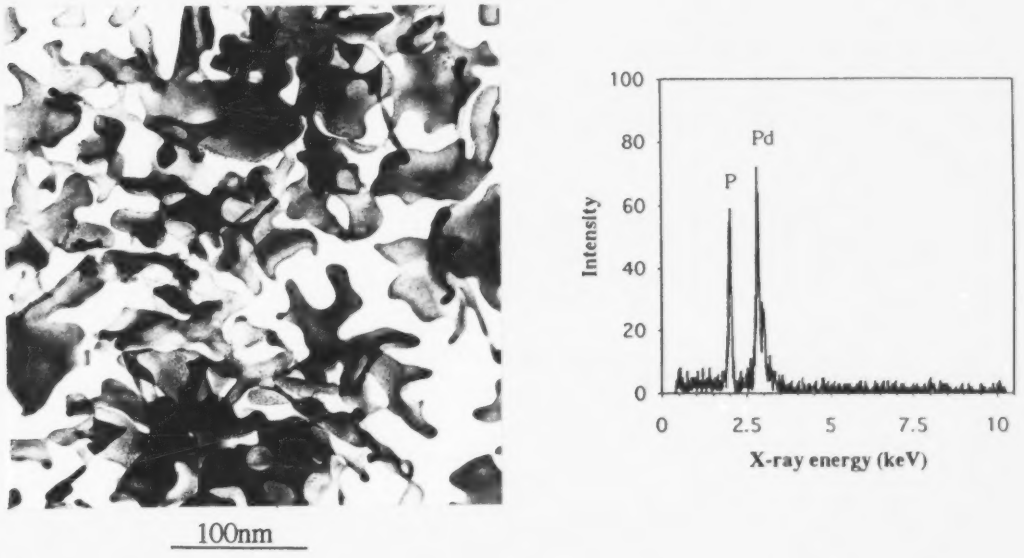

Fig. 7-16b Bright field micrograph and x-ray spectrum of a plan view specimen from the top layer of sample annealed at 425°C for 5 hours.

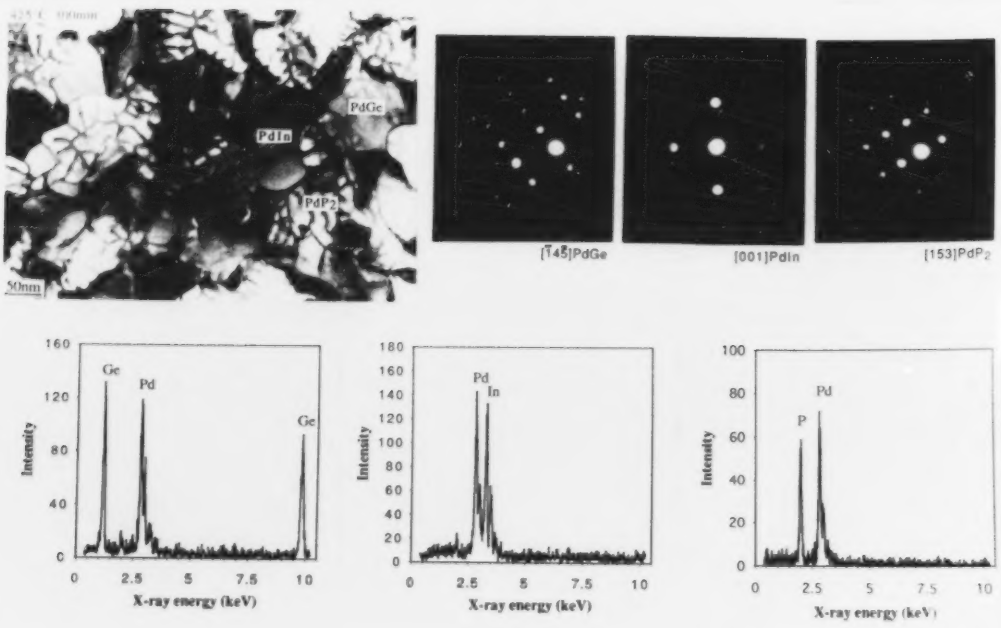

Fig. 7-16c Bright field micrograph, CBED patterns and x-ray spectra obtained from a plan view specimen annealed at 425°C for 5 hours.

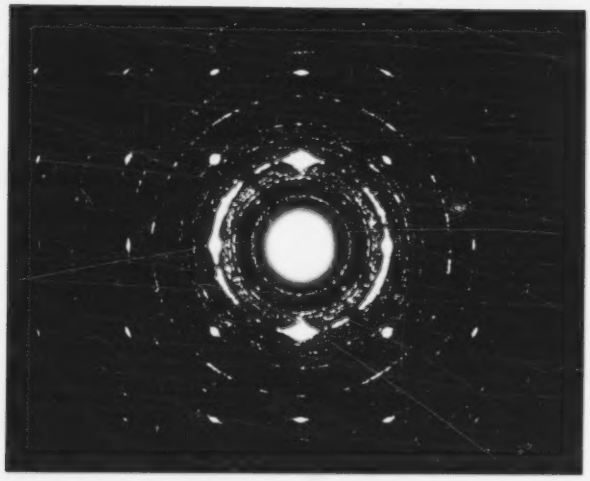

Fig. 7-16d SAD pattern taken from the plan view specimen annealed at 425°C for 5 hours. The diffracted spots are from PdIn.

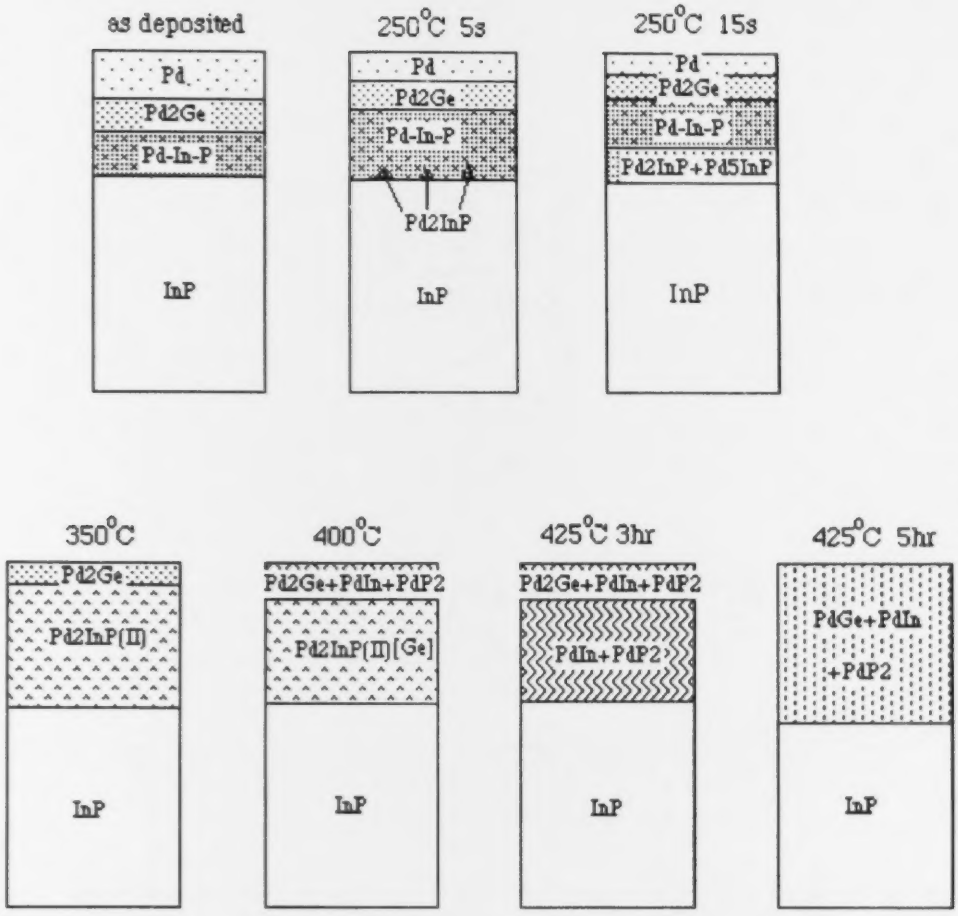

Fig. 7-17 Schematic representation of the Pd/Ge/Pd/InP contact system.

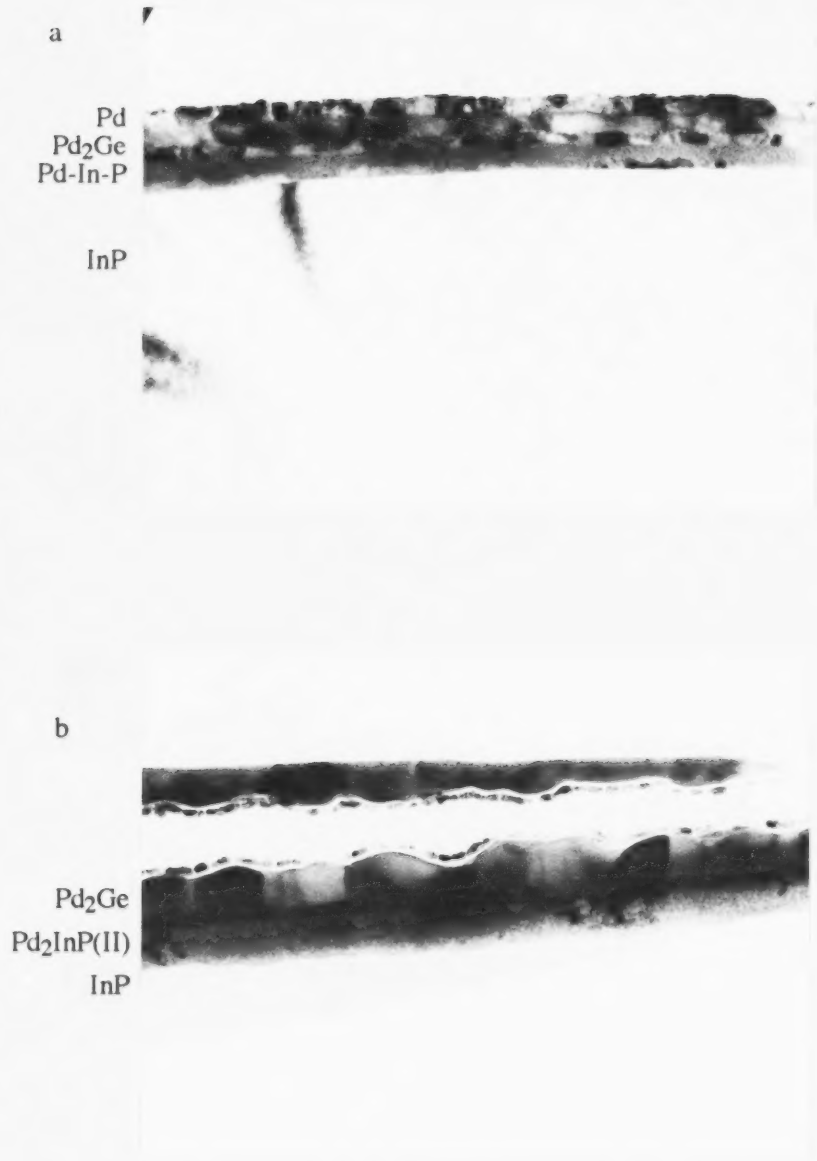

Fig. 7-18. Bright field micrographs of cross section specimens annealed at a) 250°C for 20s and b) 350°C for 10s.

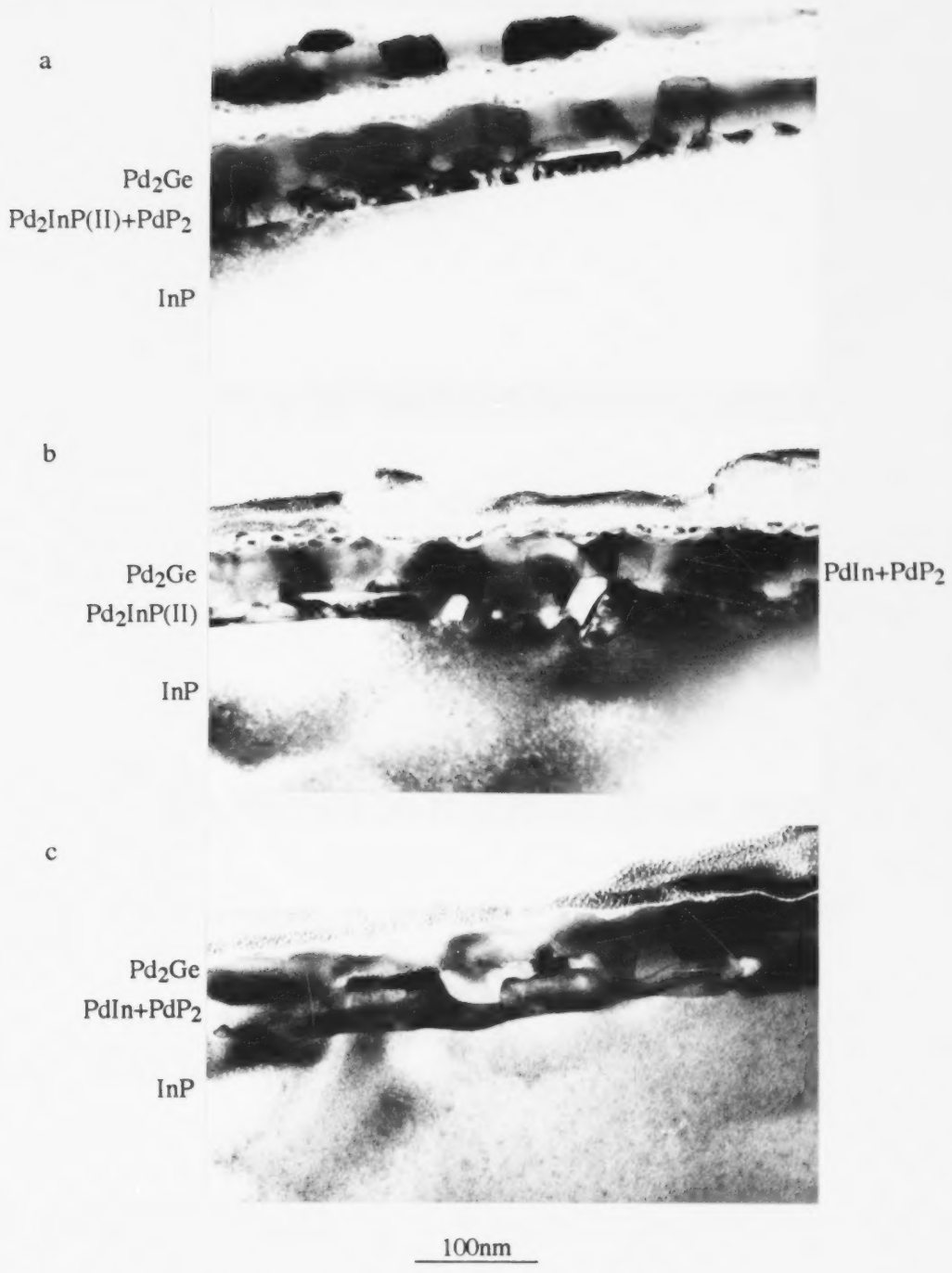

Fig. 7-19 Bright field micrographs of cross section specimens annealed at 425°C for a) 60s, b) 120s and c) 180s.

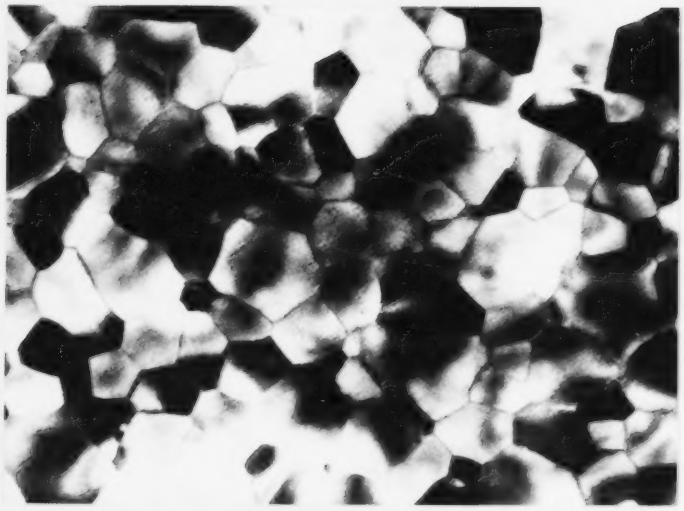

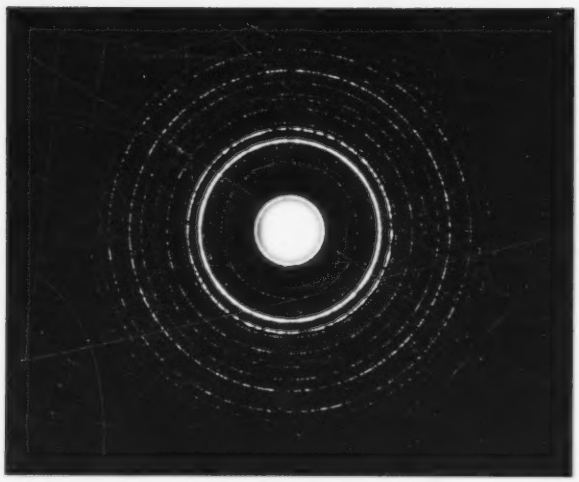

Pd_2Ge

Fig. 7-20 Bright field micrograph of Pd_2Ge phase and SAD pattern from the outer layer of the specimen annealed at 425°C for 180s.

Table 7-1 Specific contact resistances in the Pd/Ge/Pd/InP contacts

Contact (nm)	Temperature	Time	Resistance (Ωcm^2)
10nm Pd/5nm Ge/25nm Pd	350	80s	diode
10nm Pd/5nm Ge/25nm Pd	400	60s	diode
10nm Pd/5nm Ge/25nm Pd	400	180s	diode
10nm Pd/5nm Ge/25nm Pd	400	360s	diode
10nm Pd/5nm Ge/25nm Pd	400	720s	diode
10nm Pd/5nm Ge/25nm Pd	425	30s	diode
10nm Pd/5nm Ge/25nm Pd	425	60s	diode
10nm Pd/5nm Ge/25nm Pd	425	90s	diode
10nm Pd/5nm Ge/25nm Pd	425	180s	1×10^{-5}
10nm Pd/5nm Ge/25nm Pd	425	360s	$>1\times10^{-4}$
10nm Pd/5nm Ge/25nm Pd	425	1.5 hrs	diode
10nm Pd/5nm Ge/25nm Pd	425	3 hrs	diode
10nm Pd/5nm Ge/25nm Pd	450	60s	3×10^{-4}
10nm Pd/20nm Ge/25nm Pd	300	120s	diode
10nm Pd/20nm Ge/25nm Pd	350	10s	diode
10nm Pd/20nm Ge/25nm Pd	350	90s	diode
10nm Pd/20nm Ge/25nm Pd	350	320s	diode
10nm Pd/20nm Ge/25nm Pd	400	90s	diode
10nm Pd/20nm Ge/25nm Pd	400	180s	diode
10nm Pd/20nm Ge/25nm Pd	400	360s	$>5\times10^{-4}$
10nm Pd/20nm Ge/25nm Pd	400	720s	$>5\times10^{-4}$
10nm Pd/20nm Ge/25nm Pd	425	5s	diode
10nm Pd/20nm Ge/25nm Pd	425	30s	diode
10nm Pd/20nm Ge/25nm Pd	425	60s	diode
10nm Pd/20nm Ge/25nm Pd	425	90s	diode
10nm Pd/20nm Ge/25nm Pd	425	180s	3×10^{-5}
10nm Pd/20nm Ge/25nm Pd	425	360s	$>5\times10^{-4}$

Chapter 8 Conclusions and Recommendation

8.1 Conclusions

In this research, transmission electron microscopy has been used to study the microstructural changes in contacts on InP during thermal reactions. The role of Pd in ohmic contact formation and the relationship between the microstructure and the electrical properties of Au/Ge/Pd/InP and Pd/Ge/Pd/InP metallizations have been investigated. A number of conclusions can be made based on the experimental results.

1. Pd reacts with InP to form an amorphous and an epitaxial layer at low temperatures (<250°C), which provides good metallization adhesion to the InP substrates and improves the contact morphology.
2. Ohmic contacts to n-type InP have been fabricated in both the Au/Ge/Pd/InP and the Pd/Ge/Pd/InP systems.
3. The minimum specific contact resistances were $2.5\times10^{-6}\ \Omega cm^2$ in the Au/Ge/Pd/InP contacts and $1\times10^{-5}\ \Omega cm^2$ in the Pd/Ge/Pd/InP contacts respectively.
4. The annealing regime for ohmic contact formation is 300°C-375°C for the Au/Ge/Pd/InP system and 400°C-425°C for the Pd/Ge/Pd/InP system.
5. The morphology of the Pd/Ge/Pd/InP contacts is more uniform than that of the Au/Ge/Pd/InP contacts, especially after higher temperature annealing.
6. The onset of ohmic behavior in the contacts follows the decomposition of an epitaxial layer at the metallization/InP interface.
7. Ohmic contact formation in the Au/Ge/Pd/InP and the Pd/Ge/Pd/InP systems is attributed to the Ge doping mechanism based on the solid state reaction-driven decomposition of intermediate phases, which occurs at the metallization/InP interface, producing a very thin, heavily doped InP layer.
8. The degradation of the contact resistance is due to the overreaction between metals and InP, which consumes more InP and destroys the heavily doped InP layer.
9. The ratio of Ge/Pd in the contact metallization scheme can affect the reaction products between Ge and Pd, the degree of reaction between Pd and InP, the thermal stability of the Pd/Ge/Pd/InP contacts and the consumption of the InP substrate.

8.2. Recommendation

From experimental observations, it is found that the amount of Pd and Ge in the contact metallization schemes can effect the contact microstructure, the optimum annealing regime, the InP substrate consumption and the thermal stability of the ohmic contacts. In addition, from Ref. 172, the ratio of Ge/Pd can affect the value of the minimum contact resistance. Because the ratio of Ge/Pd used in this experiment is not the optimum, further investigation is recommended to find the optimum ratio of Ge/Pd the proper amount of Pd for ohmic contact fabrication.

References

1. C. Kittel, *Introduction to Solid State Physis*, John Wiley and Sons, Inc., New York, (1986)
2. J. W. Mayer and S. S. Lau, *Electronic Materials Science: For Integrated Circuits in Si and GaAs*. Macmillan Publishing Company, New York, (1990).
3. M. L. Cohen and J. R. Chelikowsky, *Electronic Stucture and Optical Properties of Semiconductor*, Berlin, Springer-Verlag, (1988).
4. D. S. Yang, *Fundamentals of Semiconductor Devices*, McGraw-hill Book Company, (1978).
5. B. G. Streetman, *Solid State Electronic Devices*, Prentice-Hall. Inc., New Jersey, (1972).
6. INSPEC, Properties of Indium Phosphide, *The Institute of Electrical Engineers*, London and New York, (1991)
7. J. M. Golio and R. J. Trew, *IEEE. Trans. Electron. Devices*, Vol. ED-30, 1411, (1983).
8. H. Morkoc, J. T. Andrews and S. B. Hyder, *IEEE. Trans. Electron. Devices*, Vol. ED-26, 238, (1979).
9. A. Katz, *Indium phosphide and Related Materials: Processing, Technology, and Devices*, Artech House, Boston, London, (1992).
10. C. W. Wilmsen, *Physics and Chemistry of III-V Compound Semiconductor Interfaces*, Plenum Press, New York and London, (1985).
11. E. H. Rhoderich and R. H. Williams, *Metal-Semiconductor Contacts*, 2nd Edition, Clarendon Press, Oxford, (1988).
12. S. M. Sze, *Physics of Semiconductor Devices*, John Wiley and Sons Inc., New York, (1969).
13. T. C. Shen, G. B. Gao and H. Morkoc, *J. Vac. Sci. Technol. B.* Vol. 10, No. 5, 2113, (1992).
14. T. C. Eschbich, R. D. Carroll, R. N. Sacks and W. *J. Tanski, IEEE. trans. Electron. Devices*, Vol. ED-36, 1213, (1989).
15. J. A. Del Alamo and J. Mizutani, *Solid State Electron.* Vol. 31, 1635, (1988).
16. P. E. Hallali, P. Blanconnier, L. Bricard and J.C. Renaud, *J. Phys. Colloq.*, Vol. 49, 453, (1988).
17. J. B. Boos and W. Kruppa, *J. Vac. Sci. Technol. B*, Vol. 7, 502, (1989).
18. H. Schumacher, J. R. Hayes, R. Bhat and M. Koza, *International Electron. Devices Meeting, IEDM, Technical Digest*, 852, (1987).

19. A. Yoshida, H. Tamura, T. Fujii and S Hasuo, *Extended Abstracts of 1987 International Superconductivity Electronic Conference ISEC*, 368, (1987).
20. H. Tenkin, R. A. Logan, R. K. Karlicek, Jr, K. E. Strege, J. P. Blaha and P. M. Gabla, *Appl. Phys. Lett.*, Vol. 53, 1156, (1988).
21. R. Kaumans, N. Grote, H. G. Bach and F. Fidorra, *Inst. Phys. Conf. Ser.* Vol. 91, 501, (1987).
22. M. Fukada, O. Fujita and S. Vetara, *J. Lightwave Technol.* G., 1808, (1987).
23. D. L. Meier and D. R. Schroeder, *IEEE trans. Electron. Dev.*, Vol. ED-31, 647, (1984).
24. A. Katz, P. M. Thomas, S. N. G. Chu, J. W. Lee and W. C. Dautremont-Smith, *J. Appl. Phys.*, Vol. 66, 2056, (1989).
25. A. Katz, W. C. Dautremont-Smith, P. M. Thomas, L. A. Koszi, J. W. Lee, V. G. Riggs, R. L. Brown, J. L. Zilko and A. Lahav, *J. Appl. Phys.*, Vol. 65, 4319, (1989).
26. J. M. Vandenberg and E. Kinsbron, *Thin Solid Films*, Vol. 65, 259, (1980).
27. T. Yoshiie, C. L. Bauer and A.G.Milnes, *Thin Solid Films*, Vol. 111, 149, (1984).
28. A. J. Barcz, *Mat. Res. Soc. Symp. Proc.*, Vol. 260, 317, (1992).
29. C. H. Mueller, P. H. Holloway and R. G. Connell, *Mat. Res. Soc. Symp. Proc.*, Vol. 260, 481, (1992).
30. Q. H. Hu, A. Kvist and H. O. Andrén, *Inst. Phys. Conf. Ser.*, No. 117, sect. 2, 91, (1991).
31. T. Sands. *Materials Science and Engineering*, B1, 289, (1989).
32. V. G. Weizer and N. S. Fatemi, *J. Appl. Phys.*, Vol. 69, 8253, (1991).
33. B. Pécz, R. Veresegyházy, G. Radnóczi, A. Barna, I. Mojzes, O. Geszti, and Gy. Vincze, *J. Appl. Phys.*, Vol. 70, 332, (1991).
34. B. Pécz, G. Radnóczi, A. Barna, R. Veresegyházy and I. Mojzes, *Inst. Phys. Conf. Ser.*, No. 117, Sect. 5, 275, (1991).
35. A. Hiraki, K. Shuto, S. Kim, W. Kammura, and M. Iwami, *Appl. Phys. Lett.*, Vol. 31, 611, (1977).
36. C. T. Tsai and R. S. williams, *J. Mater. Res.*, Vol.1 (2), 352, (1986).
37. P. W. Chye, I. Lindau, P. Pianetta, C. M. Garner, C. Y. Su, and W. E. *Spicer, Phys. Rev.*, B.18, 5545, (1978).
38. J. M. Vandenberg, H. Temkin, R. A. Hamm and M. A. DiGiuseppe, *J. Appl. Phys.*, Vol. 53, 7385, (1982).

39. J. Vandenberg, H. Temkin, R. A. Hamm and M. A. DiGuiseppe, *Thin Solid Films*, Vol. 104, 419, (1983).
40. H. Okamoto and T. B. Massalski, *Binary Alloy Phase Diagram*, Edited by T. B. Massalski, American Society for Metals, P268, (1986).
41. S. E. R. Hiscocks and W. H. Rothery, *Proc. Res. Soc. London Ser. A*, 282, 318, (1964).
42. P. Villars and L. D. Calvert, *Pearson's Handbook of Crystallographic Date for Intermetallic Phases*, American Society for Metals, (1986).
43. M. Z. Jandali, T. Rajasekharan and K. Schutbert, *Z. Metallkda*, Vol. 73, 463, (1982).
44. A. Hiraki, S. Kim, W. Kammura and M. Iwami, *Surface Science*, Vol. 86, 706, (1979).
45. L. J. Brillson, C. F. Brucker, A. D. Katnani, N. G. Stoffel and G. Margaritondo, *J. Vac. Sci. Technol.*, Vol. 19, 661, (1981).
46. C. T. Tsai and R. S. Williams, *J. Mater. Res.*, Vol.1, 820, (1986).
47. A. Piotrowska, P. Auvray, A. Guivarch, G. Pelous, and P. Henoc, *J. Appl. Phys.*, Vol.52, 5112, (1981).
48. O. Wada, *J. Appl. Phys.*, Vol. 57, 1901, (1985).
49. A. Barna and B. Pécz. *Journal of Electron Microscopy Technique*, Vol. 18, 325, (1991).
50. N. S. Fatemi and V. G. Weizer, *J. Appl. Phys.*, Vol. 67, 1934, (1990).
51. V. G. Weizer and N. S. Fatemi, *J. Appl. Phys.*, Vol. 68, 2275, (1990).
52. N. S. Fatemi and V. G. Weizer, *J. Appl. Phys.*, Vol. 65, 2111, (1989).
53. N. S. Fatemi and V. G. Weizer, *Mat. Res. Soc. Symp. Proc*, Vol. 181, 417, (1990).
54. N. S. Fatemi and V. G. Weizer, *Appl. Phys. Lett.*, Vol. 57, 500, (1990).
55. N. Szydlo and J. Olivier, *J. Appl. Phys.*, Vol. 50, 1445, (1979).
56. H. B. Kim, A. F. Lovas, G. G. Sweeney, T. M. S. Heng, *Inst. Phys. Conf. Ser.*, B33, 145, (1977).
57. J. H. Pugh and R. S. Williams, *J. Mater. Res.* Vol. 1(2), 343, (1986).
58. I. Mojzes, D. Szigethy, and R. Veresegyházy, *Electr. Lett.*, Vol. 19, 117, (1983).
59. B. Tuck, K. T. Ip, and L. F. Eastman, *Thin Solid Films*, Vol. 55, 41, (1977).
60. E. Kaminska, A. Piotrowska, A. Barcz, J. Adamczewska and A. Turos, *Solid-state Electron.*, Vol. 29, 279, (1986).
61. O. Oparaku, C. L. Dargan, N. M. Pearsall and R. Hill, *Semicond. Sci. Technol.*, Vol. 5, 65, (1990).

62. J. J. Kelly, J. M. G. Rikken, J. W. M. Jacobs and A. Valster, *J. Vac. Sci. Technol.* B., Vol. 6, 48, (1988).
63. E. Kuphal, *Solid-state Electron.*, Vol. 24, 69, (1981).
64. A. Piotrowska, E. Kaminska, A. Barcz, J. Adamczewska and A. Turos, *Thin Solid Films*, Vol. 130, 231, (1985).
65. P. Auvray, A. Guivarc'h, H. L'haridon, J. P. Mercier and P. Henoc, *Thin Solid Films*, Vol. 127, 39, (1985).
66. H. Temkin, R. J. McCoy, V. G. Keramidas and W. A. Bonner, *Appl. Phys. Lett.*, Vol. 36, 444, (1980).
67. A. J. Valois and G. Y. Robinson, *J. Vac. Sci. Technol. A*, Vol. 1(2), 466, (1983).
8. V. Malina, K. Vogel and J. Zelinka, *Semicond. Sci. Technol.*, Vol. 3, 1015, (1988).
69. V. G. Keramidas, *Thin Solid Films*, Vol. 96, 347, (1982).
70. A. J. Valois and G. Y. Robinson, *Solid-State Electron.*, Vol. 25, 973, (1982).
71. D. G. Ivey, P. Jian and R. Bruce, *Thin Solid Films*, Vol. 190, 217, (1990).
72. L. P. Erickson, A. Waseem and G. Y. Robinson, *Thin Solid Films*, Vol.64, 421, (1979)
73. D. G. Ivey, R. Bruce and G. R. Piercy, *J. Electron. Mat.*, Vol. 17, 373, (1988).
74. A. Katz and S. J. Pearton, *J. Vac. Sci. Technol.* B., Vol. 9 (1), 178, (1991).
75. P. Kringhøj, J. L. Hansen and S. Y. Shiryaev, *J. Appl. Phys.*, Vol. 72, 2249, (1992).
76. S. C. Binari and J. B. Boos, *Electron, Lett.*, Vol. 25, 1207, (1989).
77. P. A. Barnes and R. S. Williams, *Solid-State Electron.*, Vol. 24, 907, (1981).
78. I. Camlibel, A. K. Chin, F. Ermanis, M. A. DiGiuseppe, J. A. Lourenco, and W. A. Bonner, *J. Electrochem. Soc.*, Vol.129, 2585, (1982).
79. T. C. Hasenberg and E. Garmire, *J. Appl. Phys.*, Vol. 61, 808, (1987).
80. J. B. Boos and W. Kruppa, *Solid-state Electron.*, Vol. 31, 127, (1988).
81. J. Dunn and G. B. Stringfellow, *J. Electron. Mat.*, Vol. 19, No. 2, L1, (1990).
82. T. Sands, V. G. Keramidas, J. Washburn and R. Gronsky, *Appl. Phys. Lett.*, Vol. 48, 402, (1986).
83. T. Sands, V. G. Keramidas, A. J. Yu, K. M. Yu, R. Gronsky and J. Washburn, *J. Mater. Res.*, Vol. 2, 262, (1987).
84. A. Lahav, M. Eizenberg and Y. Komen, *J. Appl. Phys.*, Vol. 60, 991, (1986).
85. M. Ogawa, Thin Solid Films, Vol. 70, 181, (1980).

86. A. Lahav, M. Eizenberg and Y. Komem, *Mater. Res. Soc. Symp. Proc.*, Vol. 37, 641, (1985).
87. X. Y. Zheng, J. C. Lin, D. Swenson, K. C. Hsieh and Y. A. Chang, *Mat. Sci. Eng.* B5, 63, (1989).
88. C. H. Jan, D. Swenson and Y. A. Chang, *J. Appl. Phys.*, Vol. 68, 6458, (1990).
89. S. H. Chen, C. B. Carter, C. J. Palmstrφm and T. Ohashi, *Appl. Phys. Lett.*, Vol. 48, 803, (1986).
90. S. H. Chen, C. B. Carter and C. J. Palmstrφm, *J. Mater. Res.* Vol.3(6), 1385, (1988).
91. T. Sands, V. G. Keramidas, K. M. Yu. J. Washburn and K. Krishnan, *J. Appl. Phys.*, Vol. 62, 2070, (1987).
92. T. S. Kuan, J. L. Freeouf, P. E. Batson and E. L. Wilkie, *J. Appl. Phys.* Vol. 58, 1519, (1985).
93. T. Sands, V. G. Keramidas, R. Gronsky and J.Washburn, *Thin Solid Films*, Vol. 136, 105, (1986).
94. J. C. Lin, K. C. Hsieh, K. J. Schulz and Y. A. Chang, *J. Mater. Res.*, Vol. 3, 148, (1988).
95. P. Oelhafen, J. L. Freeouf, T. S. Kuan, T. N. Jackson and P. E. Batson, *J. Vac. Sci. Technol.*, B1.(3), 588, (1983).
96. T. Sands, V. G. Keramidas, R. Gronsky and J. Washburn, *Mater. Lett.*, Vol. 3, 409, (1985).
97. R. Beyers, K. B. Kim, and R. Sinclair, *J. Appl. Phys.*, Vol. 61, 2195, (1987).
98. J. O. Olowolafe, P. S. Ho, H. J. Hovel, J. E. Lewis and J. M. Woodall, *J. Appl. Phys.*, Vol. 50, 955, (1979).
99. X. F. Zeng and D. D. L. Chung, *J. Vac. Sci. Technol.*, Vol. 21, 611, (1982).
100. A. Oustry, M. Caumont and A. Escaut, *Thin Solid Films*, Vol. 79, 251, (1981).
101. F. Y. Shiau, S. L. Chen, M. Loomans and Y. A. Chang, *J. Mater. Res.* Vol. 6, 1532, (1991).
102. F. Y. Shiau and Y. A. Chang, *Materials Chemistry and Physics*, Vol. 32, 300, (1992).
103. F. Y. Shiau and Y. A. Chang, *Mat. Res. Soc. Symp. Proc.*, Vol. 230, 47, (1992).
104. F. Y. Shiau and Y. A. Chang, *Mat. Res. Soc. Symp. Proc.*, Vol. 230, 39, (1992).

105. C. J. Palmstrφm, C. C. Chang, A. Yu, G. J. Galvin and J. W. Mayer, *J. Appl. Phys.*, Vol. 62, 3755, (1987).
106. A. J. Yu, G. J. Galvin, C. J. Palmstrφm and J. W. Mayer, *Appl. Phys. Lett.*, Vol. 47, 934, (1985).
107. M. Genut and M. Eizeberg, *Appl. Phys. Lett.*, Vol. 50, 1358, (1987).
108. F. Y. Shiau, Y. A. Chang and L. J. Chen, *J. Electron. Mater.*, Vol. 17, 433, (1988).
109. F. Y. Shiau and Y. A. Chang, *Mat. Res, Soc. Symp. Proc.*, Vol. 148, 29, (1989).
110. F. Y. Shiau, Y. Zuo, J. C. Lin, X. Y. Zheng and Y. A. Chang, *Z. Metallkde*, Vol. 80, 544, (1989).
111. K. J. Schulz and Y. A. Chang, *Mater. Sci. Eng.*, B12, 223, (1992).
112. K. M. Yu, S. K. Cheung, T. Sands, J. M. Jaklevic and E. E. Haller, *J. Appl. Phys.*, Vol.61(3), 1099, (1987).
113. K. J. Schulz, O. A. Musbah and Y. A. Chang, *J. Phase. Equilibria*, Vol. 12, 10, (1991).
114. R. Sinclair, T. Konno, D. H. Ko and S. Ogawa, *Inst. Phys. Conf. Ser.*, No. 117, Sect. 5, 283, (1991).
115. K. J. Schulz, X. Y. Zheng, J. C. Lin and Y. A. Chang, *J. Electron. Mat.*, Vol. 19, No.6, 581, (1990).
116. C. Fontaine, T. Okumura and K. N. Tu, *J. Appy. Phys.*, Vol. 54, 1404, (1983).
117. X. Y. Zhang, K. J. Schulz, J. C. Lin and Y. A. Chang, *Journal of the Less Common Metals*, Vol. 146, 233, (1989).
118. K. J. Schulz, O. A. Musbah and Y. A. Chang, *J. Appl. Phys.*, Vol.67(11), 6798, (1990).
119. K. M. Yu, T. Sands, J. M. Jaklevic and E. E. Haller, *J. Appl. Phys.*, Vol.62(5), 1815, (1987).
120. K. J. Schulz and Y. A. Chang, *Met. Res. Soc. Symp. Proc.*, Vol. 144, 557, (1989).
121. K. J. Schulz, O A. Musbah and Y. A. Chang, *Bulletin of Alloy Phases Diagrams*. Vol. 11, 211, (1990).
122. K. M. Yu, W. Walukiewicz, J. M. Jaklevic and E. E.Haller, *Appl, Phys. Lett.*, Vol.51, 189, (1987).
123. A. Appelbaum, P. M. Thomas and P. A. Barnes, *Semiconductor-based Heterostructures: Interfacial Structure and Stability*, M. L. Green, E. E. Baglin,

G. Y. Chin, H. W. Deckman, W. Mayo and D. Narasinham Eds, The Metallurgical Society, Inc. 409, (1986).

124. M. F. Singleton and P. Nash, *Binary Alloy Phase Diagrams*, Edited by T. B. Massalski, American Society for Metals, P1386, (1986).
125. P. Nash, *Binary Alloy Phase Diagrams*, Edited by T. B. Massalski, P1738, (1986).
126. B. Bhattacharya and D. B. Masson, *Mater. Sci. Eng.*, Vol. 22, 133, (1976).
127. M. Andersson-Söderberg and Y. Andersson, *J. Solid-State Chem.*, Vol. 85, 315, (1990).
128. W. B. Pearson, *A Handbook of Lattice Spacing and Structures of Metals*, Pergamon Press London,
129. S. E. Mohney and Y. A. Chang, *J. Mater. Res.* Vol. 7, 955, (1992).
130. M. Andersson-Söderberg, *Mat. Res. Soc. Symp. Proc.* Vol. 204, 231, (1991).
131. T. Sands, C. C. Chang, A. S. Kaplan, V.G.Keramidas, K. M. Krishnan and J. Washburn, *Appl. Phys. Lett.*, Vol. 50 (19), 1346, (1987).
132. G. Stremsdoerfer, Y. Wang, J. R. Martin and E. Souteyrand, *Mat. Res, Soc. Symp. Proc.*, Vol. 260, 543, (1992).
133. A. Appelbaum, M. Robbins and F. Schrey, *IEEE Transactions of Electron Devices*, Vol. ED-34, 1026, (1987).
134. H. Okamoto, *"Alloy Phase Diagram"*, *ASM Handbook*, Vol. 3, 256, (1992).
135. H. Okamoto, *"Alloy Phase Diagram"*, *ASM Handbook*, Vol. 3, 330, (1992)
136. S. Rundqvist, *Nature*, Vol. 185, 31, (1960).
137. L. O. Gullman, *J. Less-Common Metals*, Vol. 11, 157, (1966).
138 Y. Andersson, *Acta Chemica Scandinavica*, A. 31, 354, (1977).
139. S. E. Mohney and Y. A. Chang, *Mat. Res. Soc. Symp. Proc.*, Vol. 260. 519, (1992).
140. R. C. Popowich, J. Washburn, T. Sands and A. S. Kaplan, *J. Appl. Phys*, Vol. 64 (10), 4909, (1988).
141. M. El-Boragy and K. Schubert, *Z. Metallkde*, Vol. 61, 579, (1970).
142. G. Stremsdoerfer, C. Calais, J. R. Martin and P. Clechet, *J. Electronchem. Soc.*, Vol. 137, 835, (1990).
143. M. Ogawa, *J. Appl. Phys.*, Vol. 51, 406, (1980).
144. G. Y. Robinson, *Solid-State Electron.*, Vol. 18, 331, (1975).
145. T. S. Kuan, P. E. Batson, T. N. Jackson, H. Rupprecht and E. L. Wilkie, *J. Appl. Phys.*, Vol. 54, 6952, (1983).
146. R. A. Bruce and G. R. Piercy, *Solid-State Electron.*, Vol 30, 729, (1987).

147. J. B. B. Oliveira, C. A. Olivieri and J. C. Galzerani, *Vacuum*, Vol. 41, 807, (1990).

148. S. J. Chua, S. H. Lee, R. Gopalakrishnan, K. L. Tan and T. C. Chong, *Thin Solid Films*, Vol. 200, 211, (1991).

149. H. M. Harris and J. R. Farley, *Mat. Res. Soc. Symp. Pro.*, Vol. 260. 475, (1992).

150. M. Murakami, A. Otsuki, K Tanahashi and H. J. Takata, *Mat. Res. Soc. Symp. Proc.*, Vol. 260, 457, (1992).

151. Z. Liliental and R. W. Carpenter and J. Escher, *Ultramicroscopy*, Vol. 14, 135, (1984).

152. Y. C. Shih, M. Murakami, E. L. Wilkie and A. C. Callegari, *J. Appl. Phys*, Vol. 62, 582, (1987).

153. A. A. Lakhani, *J. Appl. Phys*, Vol. 59, 2082, (1986).

154. N. Lustig, M. Marakami, M. Norcott and K. McGann, *Appl. Phys. Lett.*, Vol. 58, 2093, (1991).

155. K. B. Alexander and W. M. Stobbs, *Mater. Res. Soc. Symp. Proc*, Vol. 181, 363, (1990).

156. I. mehdi, U. K. Reddy, J. Oh, J. R. East and G. I. Haddad. *J. Appl. Phys.*,Vol. 65, 867, (1989).

157. F. Ren, T. R. Fullowan, S. N. G. Chu, S. J. Pearton, W. S. Hobson and A. B. Emerson, *J. Electron. Mater.*, Vol. 20, 305, (1991).

158. M. P. Grimshaw, A. E. S. Bevan, J. Herniman and D. A. Allan, *Mat. Res. Soc, Symp. Proc*, Vol. 181, 375, (1990).

159. M. P. Grimshaw and A. E. Staton-Bevan, *Mater. Sci. Eng.*, B5, 21, (1989).

160. U. Merkel, E. Nebauer and M. Mai, *Thin Solid Films*, Vol. 217, 108, (1992).

161. T. E. Kazior, H. Hieslmair and R. C. Brooks, *Mat. Res. Soc. Symp. Proc*, Vol. 181, 313, (1990).

162. L. Zheng, *J. Appl. Phys.*, Vol. 71, 3566, (1992).

163. C. Lin. and C. P. Lee, *J. Appl. Phys.*, Vol. 67, 260, (1990).

164. T. Sands, E. D. Marshall and L. C. Wang, *J. Mater. Res*, Vol. 3, 914, (1988).

165. L. C. Wang, S. S. Lau, E. K. Hsieh and J. R. Velebir, *Appl. Phys, Lett.*, Vol. 54, 2677, (1989).

166. C. J. Palmstrøm, S. A. Schwarz, E. Yablonovitch, J. P. Harbison, C. L. Schwartz, L. T. Florez, T. J. Gmitter, E. D. Marshall and S. S. Lau, *J. Appl. Phys.*, Vol. 67, 334, (1990).

167. E. D. Marshall, W. X. Chen, C. S. Wu, S. S. Lau and T. F. Kuech, *Appl. Phys, Lett.*, Vol. 47, 298, (1985).

168. E. D. Marshall, B. Zhang, L. C. Wang, P. F. Jiao, W. X. Chen, T. Sawada, S. S. Lau, K. L. Kavanagh and T. F. Kuech, *J. Appl. Phys.*, Vol. 62, 942, (1987).

169. A. Paccagnella, L. C. Wang, C. Canali, G. Castellaneta, M. Dapor, G. Donzelli, E. Zanoni and S. S. Lau, *Thin Solid Films*, Vol. 187, 9, (1990).

170. S. A. Schwarz, C. J. Palmstrøm, C. L. Schwartz, T. Sands, L. G. Shantharama, J. P. Harbison, L. T. Florez, E. D. Marshall, C. C. Han, S. S. Lau, L. H. Allen and J. W. Mayer, *J. Vac. Sci. Technol.*, A. 8(3), 2079, (1990).

171. L C. Wang, X. Z. Wang, S. N. Hsu, S. S. Lau, P. S. D. Lin, T. Sands, S. A. Schwarz, D. L. Plumton and T. F. Kuech, *J. Appl. Phys.*, Vol. 69, 4364, (1991).

172. J. Tsuchimoto, S. Shikata and H. Hayashi, *J. Appl. Phys.*, Vol. 69, 6556, (1991).

173. H. R. Grinolds and G. Y. Robinson, *Solid-State Electron.*, Vol. 23, 973, (1980).

174. A. K. Sinha, T. E. Smith and H. J. Levinstein, *IEEE Transactions on Electron Devices*, Vol. ED-22, 218, (1975).

175. L. C. Wang, B. Zhang, F. Fang, E. D. Marshall, S. S. Lau, T. Sands and T. F. Kuech, *J. Mater. Res.*, Vol. 3, 922, (1988).

176. L. S. Yu, L. C. Wang, E. D. Marshall, S. S. Lau and T. F. Kuech, *J. Appl. Phys.*, Vol. 65, 1621, (1989).

177. L. C. Wang, Y. Z. Li, M. Kappes, S. S. Lau, D. M. Hwang, S. A. Schwarz and T. Sands, *Appl. Phys. Lett.*, Vol. 60, 3016, (1992).

178. A. Jesús, D. Alamo and T. Mizutani, *Solid-State Electron.*, Vol. 31, 1635, (1988).

179. K. P. Pande, E. Martin, D. Gutierrez and O. Aina, *Solid-State Electron.*, Vol. 30, 253, (1987).

180. N. S. Fatemi and V. G. Weizer, *Mat. Res. Soc. Symp. Proc.*, Vol. 260, 537, (1992).

181. R. J. Graham, S. Myhajlenko and J. W. Steed, *J. Appl. Phys.*, Vol. 57, 1311, (1985).

182. D. A. Anderson, R. J. Graham and J. W. Steeds, *Semicond. Sci. Technol.*, Vol. 3, 63, (1988).

183. G. Bahir and J. L. Merz, *J. Electron. Mater.*, Vol. 16, 257, (1987).

184. H. Morkoc, T. J. Drummond and C. M. Stanchak, *IEEE Transactions on Electron Devices*, Vol. ED-28, 1, (1981).

185. D. G. Ivey, D. Wang and D. Yang, *Microscopical Society of Canada 20th Annual Meeting*, June 3-5, Toronto, Ont., (1993).

186. M. F. J. Olkeefe, R. E. Miles, M. J. Howes, *SPIE "Indium Phosphide and Related Materials for Advanced Electronic and Optical Devices"*, Vol. 1144, 361, (1989).

187. E. Yamaguchi, T. Nishioka and Y. Ohmachi, *Solid-State Electron.*, Vol. 24, 263, (1981).

188. S. A. Schwarz, M. A. A. Pudensi, T. Sands, T. J. Gmitter, R. Bhat, M. Koza, L. C. Wang and S. S. Lau, *Appl. Phys. Lett.*, Vol. 60, 1123, (1992).

189. W. X. Chen, S. C. Hsueh, P. K. L. Yu and S. S. Lau, IEEE Electron Device Letters, Vol. EDL-7, 471, (1986).

190. S. A. Schwarz, T. Sands, R. Bhat, M. Koza, M. A. A. Pudensi, L. C. Wang and S. S. Lau, Mat. Res. Soc. Symp. Proc. Vol. 260, 525, (1992).

191. D. G. Ivey, P. Jian, L. Wan, R. Bruce, S. Elcher and C. Blaauw, *J. Electron. Mater.*, 237, (1991).

192. *Powder Diffraction Files.* JCPDS-internationalCenter for Diffraction Data.

193. D. G. Ivey and G. R. Piercy, *J. Elect. Microsc. Tech.*, Vol. 8, 233, (1988).

194. L. Zhang, *MSc. Thesis*, University of Alberta, (1990).

195. B. E. P. Beeston, R. W. Horne and R. Markham, *Electron Diffraction and Optical Diffraction Techniques*, Americal Elsevier Publishing Co., (1972).

196. J. I. Goldstein, D. B. Williams and G. Cliff, Quantitative X-Ray Analysis, from "Principles of Analytical Electron Microscopy", D. C. Joy, A. D. Romig and J. I. Goldstein, eds., Plenum Press, New York, (1986).

197. A, Scorzoni and M. Finetti, *Mater. Sci. Rep.*, Vol. 3, 79, (1988).

198. G. S. Marlow and M. B. Das, *Solid-State Electron.*, Vol. 25, 91, (1962).

199. D. G. Ivey, L. Zhang and P. Jian, *J. Mater. Sci.:Mater. In Electron.*, Vol. 2, 21, (1991).

200. R. B. Schwarz and W. L. Johnson, *Physical Review Letters*, Vol. 51, 415, (1983).

201. F. Y. Shiau and Y. A. Chang, *Mat. Res. Soc. Symp. Proc.*, Vol. 187, 89, (1990).

202. C. L. Chen, M. A. Hollis, L. J. Mahoney, W. D. Goodhue, M. J. Manfra and R. A. Murphy, *J. Vac. Sci. Technol.*, B. 5(4), 902, (1987).

203. B. Goldstein, *Physical Review*. Vol. 121, 1305,(1961).

204. A. Christon, *Solid-State Electron.*, Vol. 22, 141, (1979).

205. J. Ding, J. Washburn, T. Sands and V. G. Kermidas, *Appl. Phys. Lett.*, Vol. 49, 818, (1986).